The Dissertation Committee for Laurent Olivier Froideval Certifies that this is the approved version of the following dissertation:

A Study of Solar Radiation Pressure acting on GPS Satellites

Committee:

Bob E. Schutz, Supervisor

David G. Hull

Wallace T. Fowler

Cesar A. Ocampo

Oliver Montenbruck

A Study of Solar Radiation Pressure Acting on GPS Satellites

by

Laurent Olivier Froideval, B.S, M.S.E.

Dissertation

Presented to the Faculty of the Graduate School of
The University of Texas at Austin
in Partial Fulfillment
of the Requirements
for the Degree of

Doctor of Philosophy

The University of Texas at Austin
August 2009

Acknowledgements

First, I would like to thank the University of Texas for allowing me to be part of its graduate school. I also wish to express my gratitude to Dr. Bob Schutz for his guidance and his help during my stay at the University of Texas. This is a great opportunity to express my respect to the members of my committee: Dr. David Hull, Dr. Wallace Fowler, Dr. Cesar Ocampo and Dr. Oliver Montenbruck. I am also pleased to thank Dr. Charles Webb for his precious help and advices and to Dr. Hyung-Jin Rim for his help with MSODP. Dr. Richard Eanes and Dr. John Ries assisted me incalculably in their advices on satellite laser ranging. I appreciate all the people from the Center for Space Research in Austin who helped me throughout my work. I would like to thank Dr. Marek Ziebart for his help on the UCL model. I would like to acknowledge the professors from the Aerospace Engineering Department of the University of Texas who taught me the knowledge required in this research.

I would like Mrs. Sylvianne Wignacourt to know that I am grateful for her efforts in helping me get to the graduate program at the University of Texas, which has really expanded my awareness of different cultures, and has been a superior educational experience. I thank my friends who supported me including Jennifer Bonin, Nadège Pie, Robert Harpold and Jean-Philippe Munoz. I am also very grateful to my girlfriend Amy Puett for believing in me and for her assistance in the editing process. This dissertation is dedicated to my parents and my family who were always here for me.

A Study of Solar Radiation Pressure Acting on GPS Satellites

Publication No._____________

Laurent Olivier Froideval, Ph.D.
The University of Texas at Austin, 2009

Supervisor: Bob E. Schutz

An increasing number of GPS applications require a high level of accuracy. To reduce the error contributed by the GPS ephemerides, an accurate modeling of the forces acting on GPS satellites is necessary. These forces can be categorized into gravitational and non-gravitational forces. The non-gravitational forces are a significant contribution to the total force on a GPS satellite but they are still not fully understood whereas the gravitational forces are well modeled. This study focuses on two non-gravitational forces: Solar Radiation Pressure (SRP) and the y-bias force.

Different SRP models are available in the University of Texas Multi-Satellite Orbit Determination Program (MSODP). The recently developed University College London model was implemented for the purpose of this study. Several techniques to compute parameters associated with SRP models and the y-bias force during an orbit prediction were examined. Using the International GNSS Service (IGS) precise ephemerides as a reference, five different models were compared in the study. Satellite Laser Ranging (SLR) residuals were also studied to validate the approach. Results showed that the analytical UCL model performed as well as a purely empirical model such as the Extended CODE model. This is important since analytical models attempt to represent the physical phenomena and thus might be better suited to separate SRP from other forces. The y-bias force was then shown to have a once per revolution effect. The time evolution of the y-bias was found to be dependent on the SRP model used, the satellite Block type, the orbital plane, and the attitude of the satellite which suggests that estimates of y-bias contain errors from other sources, particularly the SRP models. The dependency of the y-bias evolution on the orbital plane suggests that the orientation of the plane towards the Sun is important.

Table of Contents

List of Tables

List of Figures

Chapter 1

Introduction

1.1 NAVIGATION

The art of navigation has always been of interest to mankind. In Egypt, around 2600 BC, under Pharaoh Snefru, an ancient scribe wrote about the use of boats to carry heavy loads: “Bringing of forty ships filled with cedar logs” [Casson, 1914]. Later, in the 13th century BC, the Phoenicians developed important seafaring activities in order to first promote trade between independently developed cities and then to expand their civilization by creating convenient new colonies that were regularly spread on the Mediterranean coastline such as Carthage or Motya [Moscati, 1988]. Phoenicians used short-haul coastal navigation as well as deep-sea navigation. In the latter case, they used the Ursa Minor constellation to ensure they had the proper direction. The North Star was previously known as the “Phoenician Star”.

One of the first tools introduced in navigation was the compass. The first record of a primitive compass is believed to be found in China around the 4th century BC. It became widely used by sailors around the 11th century AD. Invention of newer tools such as the mariner astrolabe in the 13th century, later improved with the quadrant, followed by the octant and the sextant [Harding, 1952], allowed the measurement of latitude. The longitude, on the other hand, remained harder to precisely measure. In Europe, around the 16th century, a new quest to find a practical longitude measurement technique [Bruyns, 1993]. The measurement of time became the key to measuring accurately the longitude. Marine chronometers were among the first practical tools to keep track of time on ships. It was commonly used in the 18th century. In the modern times, navigation techniques include radio navigation and radar navigation already in use during World War II. Nowadays, satellite navigation stands as a crucial navigation tool. The first satellite navigation system developed was the US Navy Navigation Satellite System (NAVSAT) which became operational in 1964. Also known as TRANSIT, it used a constellation of about 10 satellites, but it could not support instantaneous, global navigation. Global Navigation Satellite Systems (GNSS) started to emerge. Their performance kept increasing over time. In 1973, the US Department of Defense (DOD) began to finance the development of the NAVigation Satellite Timing And Ranging (NAVSTAR) Global Positioning System (GPS). A few years later, the Soviet Union also started to create their own GNSS, simply known as GLObal NAvigation Satellite System (GLONASS). In addition, Europe recently launched the first 2 satellites of its future GNSS constellation known as Galileo. It is also worth mentioning that China is likely to transform its regional navigation system Beidou into the newly planned GNSS Compass.

The GPS is the most widely used GNSS. This is mostly due to its accuracy combined with the fact that it remains the only fully operational constellation. It is typically decomposed into three segments. The space segment encompasses the constellation of spacecrafts along with their transmitted signals. The control segment, also known as Operational Control System (OCS) includes the ground stations that track, control and maintain the satellites. Finally, the user segment describes the receivers, the applications and the measurements techniques.

1.2 THE GLOBAL POSITIONING SYSTEM

1.2.1 Constellation

In 1995, the US Air Force (USAF) Space Command declared the GPS constellation operational (Figure 1.1). At the time, it was consisted of satellites known for their design characteristics as Block II and Block IIA satellites built by Rockwell International. The satellites known as Block I satellites were used for engineering test purposes. General Electric Astro Space, today part of Lockheed Martin, designed the Block IIR satellites that gradually are replacing the Block II/IIA satellites. Block IIR-M satellites are a "modernized" version of Block IIR satellites. The next generation of spacecraft, the Block IIF, will be built by Boeing and are currently scheduled for 2009. In 2008, the USAF awarded Lockheed Martin the contract for the first series of the much improved Block IIIA satellites, which will include a modernization of the broadcast signals [Gao, 2009], scheduled to be launched starting in 2014.

Figure 1.1. The GPS constellation [Boeing, 2007]

Current constellation status is maintained by the OCS and can be found on different public servers such as the ones of the US Coast Guard (USCG) or at Shriever Air Force Base (AFB). As of November 2008, the constellation includes 31 satellites distributed as follows: 13 Block IIAs, 12 Block IIRs, 6 Block IIR-Ms. More details can be found in Table 1.1. GPS satellites can be designated by their Space Vehicle Number (SVN) or by their Pseudo Random Noise (PRN) number.

1.2.2 Satellite requirements

The satellites are designed to perform three functions. They need first to be able to keep a very accurate time since precise time keeping is crucial in GPS positioning. To support this task, they carry high accuracy atomic clocks: a Rubidium (Rb) and Cesium (Cs) atomic clock. The resulting error is as low as 1 second in 3,000,000 years [Rizos, 1999].

The second function of a GPS satellite is to transmit information to users. GPS satellites transmit two different frequencies L1 and L2 at 1575.42 MHz and 1227.60 MHz respectively [Hofmann-Wellenhof et al., 2001]. The choice of frequencies allows the signal to be highly directional and to easily penetrate the clouds and the rain. Using L1 and L2, the signal is then transmitted using two different codes: the Coarse Acquisition (C/A) or Clear/Access code and the P-code for Precise code. Both codes are based on algorithms that generate a signal with random characteristics. However, the C/A code repeats itself every millisecond and the P-code every 267 days. This is the reason why they are referred to Pseudo Random Noise (PRN) codes. This design has several advantages. The receivers use similar specific PRN codes to lock onto the satellite signal. Thus the signal does not need to be transmitted with high power. It also allows the signal

Plane	Slot	SVN	PRN	Block	Clock
A	1	39	9	IIA	CS
A	2	52	31	IIR-M	RB
A	3	38	8	IIA	CS
A	4	27	27	IIA	CS
A	5	25	25	IIA	RB
A	6	48	7	IIR-M	RB
B	1	56	16	IIR	RB
B	2	30	30	IIA	CS
B	3	44	28	IIR	RB
B	4	58	12	IIR-M	RB
B	5	35	5	IIA	RB
C	1	36	6	IIA	RB
C	2	33	3	IIA	CS
C	3	59	19	IIR	RB
C	4	53	17	IIR-M	RB
C	6	57	29	IIR-M	RB
D	1	61	2	IIR	RB
D	2	46	11	IIR	RB
D	3	45	21	IIR	RB
D	4	34	4	IIA	RB
D	5	24	24	IIA	CS
E	1	51	20	IIR	RB
E	2	47	22	IIR	RB
E	3	40	10	IIA	RB
E	4	54	18	IIR	RB
E	5	23	32	IIA	RB
F	1	41	14	IIR	RB
F	2	55	15	IIR-M	RB
F	3	43	13	IIR	RB
F	4	60	23	IIR	RB
F	5	26	26	IIA	RB

SVN stands for Space Vehicle Number
PRN stands for Pseudo Random Noise
CS stands for Cesium
RB stands for Rubidium

Table 1.1. Constellation status as of November 2008 [USCG, 2008]

to be tracked even with considerable ambient noise. Lastly, the signal has a very high anti-jamming capability.

The third function required from GPS satellites is to be able to receive and store data from the OCS. Indeed, the satellite need to know their precise position which is later transmitted to the receivers.

1.2.3 The Operational Control System

The OCS is composed of a Master Control Station (MCS), located at Shriever AFB in Colorado, along with five primary DOD ground stations spread around the world in Ascension Island, Cape Canaveral, Diego Garcia, Hawaii and Kwajalein. Ten stations from the National Geospatial Intelligence Agency (NGA) were later added to this network. These stations are also evenly distributed around the world and are located in: Alaska, Washington, Ecuador, Argentina, United Kingdom, South Africa, Bahrain, South Korea, Australia and New Zealand. The MCS remotely controls the other ground stations and is operated by the US Air Force Space Command. The OCS is in charge of operational orbit determination. Furthermore, it uploads updated ephemerides to the satellites. Updated clock information is also provided to the satellites. In addition, the OCS continuously monitors the health of the satellites as well as performs the necessary station keeping maneuvers to maintain the one day repeat ground track. Lastly, the OCS can turn on and off the selective availability (SA) and the Anti Spoofing (AS). SA was introduced to degrade the accuracy of GPS for civilians. SA was deactivated in May 2000 [Hofmann-Wellenhof et al., 2001] but DOD theoretically could reactivate it at anytime. AS is a special encryption code, known as Y-code, that increases military receivers' anti-jamming capabilities. AS was turned on in January 1994.

1.2.4 Orbit Description

The GPS satellites are distributed among 6 orbital planes, each with an inclination of about 55°. Their altitude is relatively high at about 20,200 km above the Earth. The satellites are orbiting in near circular orbits ($e \leq 0.02$). The satellites' orbital period is approximately half the sidereal rotation period of the Earth which, in turn, ensures that the satellites perform two revolutions per sidereal day. In addition, the ground track illustrated in Figure 1.2 repeats closely after one day. However, a small drift to the west can be observed. Regular orbital maneuvers are performed to ensure that the ground track stays within acceptable bounds. The GPS orbits were designed to ensure that a minimum of four satellites are visible at all time anywhere on the surface of the Earth. Moreover, the DOD guarantees coverage with 24 satellites 70% of the time and with 21 satellites 98% of the time.

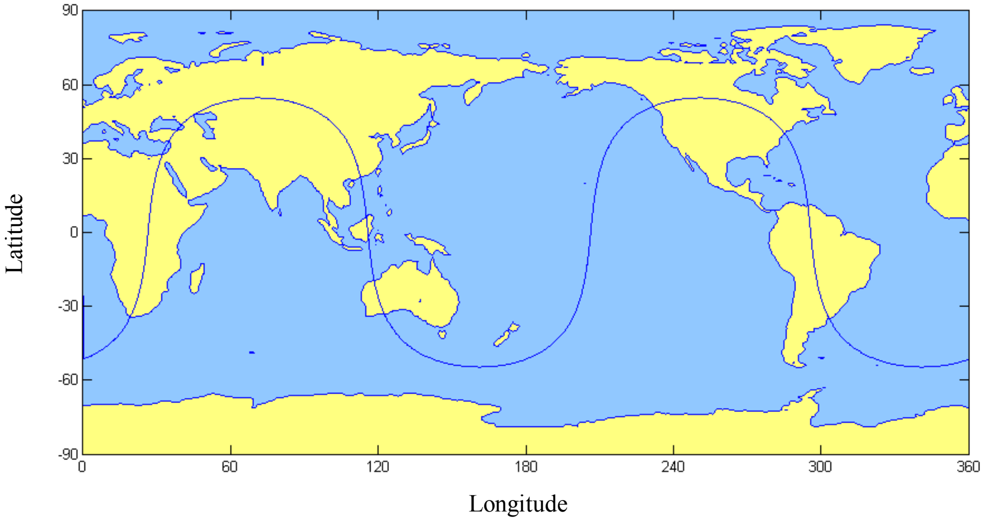

Figure 1.2. PRN 22, 1 day ground track for December 1st 2006

1.2.5 GPS Time

GPS time is a continuous time scale. It is referenced to the Coordinated Universal Time (UTC). It started on January 6th, 1980 and was then coincident with UTC [Kaplan and Hegarty, 2006]. GPS time does not include all the corrections brought to UTC. Indeed, UTC is a composite time including inputs form the International Atomic Time (TAI) and on the Universal Time 1 (UT1). UT1 is based on the Earth's rotation with respect to the Sun and includes corrections for nonuniformities in the Earth's orbital speed and in the inclination of the Earth's equator with respect to its orbital plane [Kaplan and Hegarty, 2006]. The International Earth Rotation Service (IERS) is in charge of keeping the difference between UTC and UT1 under 0.9 seconds by adding or subtracting leap seconds to UTC. GPS time is not corrected with leap seconds like UTC. Thus, GPS time and UTC do not coincide. On December 31st, 2008, the IERS introduced a leap second into UTC which made GPS time to be 15 seconds ahead of UTC.

GPS weeks began with week 0 and are numbered sequentially, starting with from January 6th, 1980. The GPS week contain 7 days ranging from day 0 to day 6 where day 0 corresponds to Sunday. For instance, day 2 of GPS week 1460 corresponds to Tuesday, January 1st, 2008.

1.3 IGS PRECISE EPHEMERIDES

1.3.1 The IGS

In addition to OCS tracking stations discussed in Section 1.2.3, the International GNSS Service (IGS), a civilian federation of hundreds of worldwide institutions, generates precise ephemerides for GPS [Dow et al., 2005]. The IGS encompasses a network of tracking stations, Data Centers, Analysis Centers and a Central Bureau.

The network of tracking stations collecting GPS data is shown in Figure 1.3. Some stations already belong to local networks such as the Continuously Operating Reference Stations (CORS) from the US National Geodetic Survey (NGS) [Gurtner, 2008]. The IGS also uses a selection of tracking stations from existing Regional networks such as the European Reference Frame network (EUREF). Regional networks include local networks along with individual tracking stations. In addition, some independent tracking stations also contribute to the IGS network. The tracking stations are managed by the Operational Centers. The GPS data collected are formatted and made available through the IGS Data Centers.

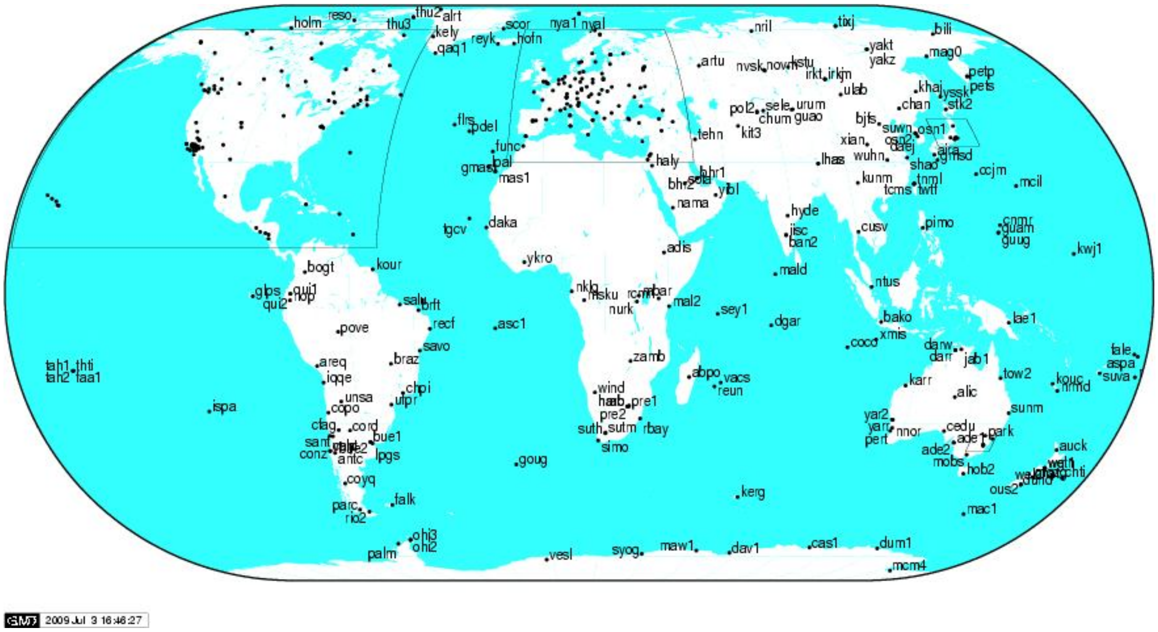

Figure 1.3. The IGS Tracking stations [IGS, 2008a]

IGS Data Centers can be separated in three categories: local, regional and global Data Centers. Local and regional centers collect data from local and regional networks respectively. A list of the current regional Data Centers is shown in Table 1.2. Each global Data Center collects the data from the different regional Data Centers along with data sent directly from the individual stations. The four current IGS global Data Centers are listed in Table 1.3.

Organization	**Acronym**
Geoscience Australia	GA
Bundesamt fur Kartographie und Geodaesie	BKG (IfAG)
NGS/NOAA Operational Data Center, NOAA	NGS/NOAA
Hartebeesthoek Radio Astronomy Observatory	HRAO
Jet Propulsion Laboratory	JPL
RDAAC-IRIS	RDAAC-IRIS

Table 1.2. IGS regional Data Centers [IGS, 2008b]

Organization	**Acronym**
Crustal Dynamics Data Information System, USA	CDDIS
Institut Geographique National, France	IGN
Scripps Institution of Oceanography, USA	SIO
Korean Astronomy and Space Science Institute, South Korea	KASI

Table 1.3. IGS global Data Centers [IGS, 2008b]

The IGS Analysis Centers use the available data to generate different products such as precise ephemerides and satellite clock corrections. At the present time, there are ten Analysis Centers. A detailed list is provided in Table 1.4. In addition, Associate Analysis Centers produce specialized or derived products. Lastly, the Analysis Center Coordinator (ACC) combines the solutions from each individual Analysis Center to generate the different official IGS products. Currently, up until 2011, NOAA's NGS in Silver Spring, Maryland is acting as Analysis Center Coordinator.

The IGS Central Bureau is located at Jet Propulsion Laboratory (JPL) in Pasadena, California. It is responsible for the overall coordination and management of the IGS. In addition, it provides information to the users through the Central Bureau Information System (CBIS). Among other things, it distributes the different IGS products via FTP servers.

Organization	**Country**	**Acronym**
Center for Orbit Determination in Europe, AIUB	Switzerland	CODE
European Space Operations Center, ESA	Germany	ESOC
GeoForschungsZentrum	Germany	GFZ
Jet Propulsion Laboratory	USA	JPL
National Oceanic and Atmospheric Administration / NGS	USA	NOAA
Natural Resources Canada	Canada	NRCan
Scripps Institution of Oceanography	USA	SIO
US Naval Observatory	USA	USNO
Massachusetts Institute of Technology	USA	MIT
Geodetic Observatory Pecny	Czech Republic	GOP-RIGTC

Table 1.4. IGS Analysis Centers [IGS, 2008b]

1.3.2 Generating the IGS ephemerides

As seen in Section 1.3.1, the Analysis Centers generate precise ephemerides by processing the GPS data collected by the network of tracking stations that are available through the global Data Centers. Currently, there are four main IGS ephemerides products for GPS: Final, Rapid, Ultra-Rapid (observed half) and Ultra-Rapid (predicted half) ephemerides. A summary of the accuracy of the different ephemerides is presented in Table 1.5 [IGS, 2008c]. In this study, the Final IGS ephemerides are used.

GPS Satellite Ephemerides	Accuracy	Latency	Sample Interval
Broadcast	~160 cm	real time	daily
Ultra-Rapid (predicted half)	~10 cm	real time	15 min
Ultra-Rapid (observed half)	<5 cm	3 hours	15 min
Rapid	<5 cm	17 hours	15 min
Final	<5 cm	~13 days	15 min

Table 1.5. IGS GPS satellite ephemerides products [IGS, 2008c]

To obtain the official IGS products, each individual Analysis Center first generates independently the different ephemerides using its own processing strategy. For example, the software used can be different from the other Analysis Centers as well as the orbital models or the estimated parameters may be different. As a comparison, a summary of the solar radiation pressure models used is shown Appendix A [IGS, 2008b]. In addition, a detailed example of processing strategy from Center for Orbit Determination in Europe (CODE) can be found in Appendix B.

Because of the differences in processing, the ephemerides from each Analysis Center are combined to obtain the official IGS ephemerides. The combination process results in more reliability and precision [Beutler et al., 1995]. This also allows one Analysis Center to fail without significantly affecting the integrity of the combined orbit. In addition, it gives the individual Analysis Center more flexibility with respect to their processing strategy.

The first step in combining the different orbits is to remove the differences in reference frame [Beutler et al., 1995]. Next, a weight is assigned for each Analysis Center based on orbit comparisons and previous combinations. A detailed explanation of the combination process can be found in Beutler et al. [1995].

As described previously in Section 1.3.1, the ACC is in charge of generating the combined products. Figure 1.4 provides a way of comparing the differences between the individual Analysis Center's solutions and the combined solution [IGS ACC, 2009]. It is worth noting that, over time, these differences are getting smaller and smaller.

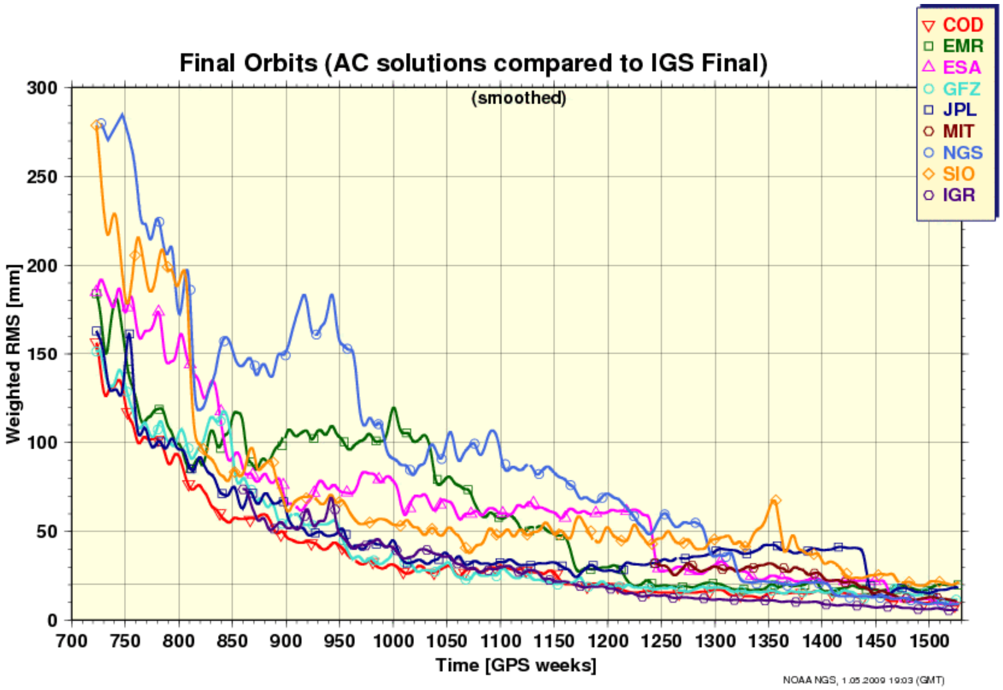

Figure 1.4. Weighted Root Mean Square (mm) of the individual Analysis Center orbit solutions with respect to the IGS Final products [IGS ACC, 2009]

After processing, the IGS ephemerides are made available through any of the FTP servers provided by the global Data Centers listed in Table 1.3. These precise ephemerides are given in the Standard Product #3 (SP3) format. A sample SP3 file is presented in Table 1.6. The header provides information about the number of satellites, the time period of the ephemerides (given as GPS week number) used and the estimated accuracy for each satellite. The epoch is provided in year, month, day, hour, minute and second in GPS time. Satellite positions are given in km and provided every 15 min in the Earth-Centered, Earth-Fixed (ECEF) International Terrestrial Reference Frame (ITRF) along with the clock offset in microseconds. In the latest version of the SP3 format, version c, for each epoch and each satellite the standard deviation is provided in mm for x, y and z.

```
#cP2008  2  3  0  0  0.00000000      96 ORBIT IGS05 HLM  IGS
## 1465      0.00000000   900.00000000 54499 0.0000000000000
+   31   G01G02G03G04G05G06G08G09G10G11G12G13G14G15G16G17G18
+        G19G20G21G22G23G24G25G26G27G28G29G30G31G32  0  0  0
+          0  0  0  0  0  0  0  0  0  0  0  0  0  0  0  0  0
+          0  0  0  0  0  0  0  0  0  0  0  0  0  0  0  0  0
+          0  0  0  0  0  0  0  0  0  0  0  0  0  0  0  0  0
++         2  3  2  2  3  2  2  2  2  3  3  2  2  3  3  3  3
++         3  3  2  2  2  2  2  2  2  2  3  3  3  4  0  0  0
++         0  0  0  0  0  0  0  0  0  0  0  0  0  0  0  0  0
++         0  0  0  0  0  0  0  0  0  0  0  0  0  0  0  0  0
++         0  0  0  0  0  0  0  0  0  0  0  0  0  0  0  0  0
%c G  cc GPS ccc cccc cccc cccc cccc ccccc ccccc ccccc ccccc
%c cc cc ccc ccc cccc cccc cccc cccc ccccc ccccc ccccc ccccc
%f  1.2500000  1.025000000  0.00000000000  0.000000000000000
%f  0.0000000  0.000000000  0.00000000000  0.000000000000000
%i    0    0    0    0      0      0      0      0         0
%i    0    0    0    0      0      0      0      0         0
/* FINAL ORBIT COMBINATION FROM WEIGHTED AVERAGE OF:
/* cod emr esa gfz jpl mit ngs sio
/* REFERENCED TO IGS TIME (IGST) AND TO WEIGHTED MEAN POLE:
/* PCV:IGS05_1461 OL/AL:FES2004  NONE     Y  ORB:CMB CLK:CMB
*  2008  2  3  0  0  0.00000000
PG01 -19287.689729 -17729.308385  -4373.894394    183.183361  8  9  8 139
PG02  14590.507862   5927.258983 -21585.238455    171.266805  9 12  9 106
PG03 -22778.551939  -7993.615002  11206.153023    181.805753  8 11  7 120
.... ............  ........... ............   .......... .. .. .. ...
.... ............  ........... ............   .......... .. .. .. ...
.... ............  ........... ............   .......... .. .. .. ...
PG32 -17533.509472  -9487.706846  17918.818903    218.534837  9 10 15 126
*  2008  2  3  0 15  0.00000000
PG01 -19412.957160 -18102.644776  -1488.604656    183.186929  7  9  8 136
PG02  14006.974231   8269.465752 -21224.257287    171.269527  9 12  8 121
PG03 -23522.349000  -8944.272345   8768.661126    181.811335  8 11  7 125
.... ............  ........... ............   .......... .. .. .. ...
.... ............  ........... ............   .......... .. .. .. ...
.... ............  ........... ............   .......... .. .. .. ...
PG32 -15539.071521 -10009.520153  19463.198029    218.543717  9  9 14 137
.... ............  ........... ............   .......... .. .. .. ...
.... ............  ........... ............   .......... .. .. .. ...
.... ............  ........... ............   .......... .. .. .. ...
```

Table 1.6. SP3 version c file

Since 1994, the different Analysis Centers have modified their processing strategy several times. Improvements were made such as the implementation of improved software and the use of more accurate orbital models. Over time, these changes produced inconsistencies in the products of each other. The IGS has decided to reprocess all the data using consistent models and references frames, for example, to generate more consistent products. Five reprocessing campaigns have been planned so far, each one focuses on a particular aspect [Steigenberger et al, 2008]. The first campaign started in February 2008 and is expected to end in 2010. It was designed to insure that all the Analysis Centers follow the same rules. The preliminary reprocessed combined products are expected for the end of 2009.

1.4 APPLICATIONS

An increasing number of applications require a high level of accuracy from GPS, such as various geodetic applications. Using a network of ground stations, GPS can help measure the changes in shape of the Earth, the polar motion or the rate of rotation of the Earth [Evans et al., 2002]. Johnson et al. [2001] emphasize the importance of orbit modeling errors in measuring the post-glacial rebound.

A high level of orbit accuracy is also required for near real-time applications such as near real-time atmospheric monitoring used in weather predictions [Ge et al., 2000 and Springer and Hugentobler, 2001]. Another example is the use of GPS as an aircraft Instrument Landing System (ILS) for category I precision approach [Pervan and Gratton, 2005]. In another example, Wang [2006] shows how the time required by a receiver to lock onto satellites could be reduced by embedding an orbit prediction algorithm in the receiver. This could be particularly useful for indoor applications. In the future, GPS could also be a tool to study the oceans and the ice sheets using GPS bistatic altimetry [Evans et al., 2002]. Onboard instruments could measure GPS signals that are reflected from the ground. The advantage in this case is the ability to use the great number of measurements from the different satellites in the GPS constellation or in future GNSS constellations to reduce the errors. Tests of bistatic GPS altimeters can be found for instance in Wilmhoff et al. [2007].

1.5 DISSERTATION OBJECTIVES

As we saw in Section 1.4, an increasing number of GPS applications require a high level of accuracy. One of the sources of errors lies in the GPS satellites ephemerides. Broadcast ephemerides are used for most real time applications and show errors of about 160 cm [IGS, 2008c]. For non-real-time applications, precise ephemerides are better suited since they are more accurate. For instance, the precise ephemerides generated at the IGS are believed to have errors under 5 cm [IGS, 2008c]. To produce both the broadcast ephemerides and the precise ephemerides, a complete and accurate modeling of the forces acting on the satellites is necessary. These forces can be categorized into gravitational and non-gravitational forces. Although nowadays the gravitational forces are well modeled, the non-gravitational forces remain still not fully understood. This main focus of this work is on two non-gravitational forces: Solar Radiation Pressure (SRP) and the y-bias force. Ultimately, this study aims to improve our knowledge of the current GPS constellation orbits and will possibly have implications for the next generation of GPS satellites and for future GNSS such as the European system Galileo.

1.6 DISSERTATION OUTLINE

In Chapter 2, theoretical considerations about SRP are described. Chapter 3 introduces the orbit determination software used in this study, namely, the University of Texas Multi-Satellite Orbit Determination Program (MSODP). A summary of the batch estimation theory is provided. In Chapter 4, a description of the gravitational forces along with the non-gravitational forces is presented. The gravitational forces are dominated by the Earth mass distribution and by the third body effect of the Sun and the Moon. The way they are modeled along with some of their known effects on the GPS orbit is described. The non-gravitational forces on the other hand, at the altitude of GPS satellite, are dominated by solar radiation pressure. Other non-gravitational forces include Earth radiation pressure, the y-bias force or the antenna recoil. A description of the different existing solar radiation pressure models, along with a brief study of the short-term effects of SRP on orbital elements, is presented. For the purpose of the study a newly developed model is implemented into MSODP. Developed at University College London, this model is based on physical assumptions. Chapter 5 justifies the use of the IGS ephemerides in this study. Indeed, it is important to assess the influence of the ephemerides generated by each individual center on the combined IGS ephemerides (see Section 1.3.2).

Chapter 6 first covers in more details the way solar radiation pressure is computed during an orbit prediction. The central issue here is to study how to handle the parameters used by the solar radiation pressure models and the y-bias force. The different SRP models are then compared by performing orbit fits using the IGS precise ephemerides as observations. The main purpose is to show that a modern analytical model performs as well as a purely empirical model such as the CODE model. Another way to look at the performance of the models is to see how well they behave during orbit predictions. Satellite Laser Ranging (SLR) data is then used as an independent set of data to confirm the previous approach that uses IGS precise ephemerides. The next section is dedicated to the y-bias force. A brief frequency analysis of the y-bias force is presented and observations about the dependencies of the y-bias force are made.

Chapter 2

Solar Radiation Pressure

2.1 THEORY

2.1.1 Origins

In 1871, in his book "Theory of heat" [Maxwell, 1871], James Clerk Maxwell expressed the idea that energy is transferred from one body to another by radiation: "The phenomenon of radiation consists in the transmission of energy from one body to another by propagation through the intervening medium, in such a way that the progress of the radiation may be traced, after it has left the first body and before it reaches the second, travelling through the medium with a certain velocity, and leaving the medium behind it in the condition in which it found it." This idea gets developed in his book on electricity and magnetism published in 1873 as seen in [Maxwell, 1873]. A few years later, Adolfo Bartoli [Bartoli, 1884] proved the existence of radiation pressure from the theory of thermodynamics. Pyotr Lebedev in 1900 and later Ernest Nichols and Gordon Hull in 1901 studied radiation pressure in their experiments.

In 1894, Max Planck worked on the black-body problem and the link between temperature and radiation. He found that the energy of a vibrating molecule is proportional to its frequency as follows:

$$E = h \cdot f \tag{2.1}$$

where

E is the energy of a molecule

h is the Planck, $h = 6.6260689633 \times 10^{-34} J \cdot s$

f is the frequency of the molecule

It was a revolutionary idea to propose that energy could be quantized. In other words energy could be decomposed in different pieces. A few years later, Albert Einstein extended Planck's idea to light and stated that its energy could also be a discrete quantity. Each piece of light, or photons, would then also have its energy proportional to its frequency. In his theory of relativity, Einstein derived a formula that relates the Energy of a photon to its momentum:

$$E = c \cdot p \tag{2.2}$$

where

E is the Energy of a photon

c is the speed of light

p is the momentum of a photon

Combining Equation (2.1) with Equation (2.2) leads to:

$$E = h \cdot f = c \cdot p \tag{2.3}$$

$$p = \frac{h \cdot f}{c} \tag{2.4}$$

Integrating over all the frequencies, and then further integrating over the number of photons per unit area leads to a force per unit area. At a distance of one Astronomical Unit (A.U.), this force can be expressed as:

$$F = \frac{S}{c} \tag{2.5}$$

where

S	is the Total Solar Irradiance (TSI)
c	is the speed of light

Note that for a given distance from the Sun d, the TSI is then scaled as follows:

$$S_d = S \cdot \left(\frac{D}{d} \right)^2 \tag{2.6}$$

where

D	is equal to 1 astronomical unit
d	is a given distance from the Sun

Therefore, the force per unit area caused by solar radiation pressure at a distance d can be formulated as:

$$F = \frac{S}{c} \cdot \left(\frac{D}{d} \right)^2 \tag{2.7}$$

2.1.2 Concepts of Radiometry

The total irradiance measures the amount of radiating power from all frequencies incident on a surface. It is expressed in watts (W) per meter square (W/m^{-2}). If we consider only one specific frequency, it is then called spectral irradiance.

The Total Solar Irradiance coming from the Sun or TSI is sometimes called the solar constant although this is not true. An approximate value is 1366 W/m^{-2}. At the beginning of the 20th century, Charles Abbot was one of the first scientists to measure the TSI. However, precise measurements of the TSI over time only came with satellite missions like the Solar Maximum Mission satellite (SMM) launched in 1980. Details about the variations of the TSI found by the Active Cavity Radiometer Irradiance Monitor (ACRIM) onboard the SMM satellite are given by Willson et al. [1981]. The TSI continued to be measured by the Upper Atmosphere Research Satellite (UARS) carrying ACRIM II and later on by the Active Cavity Radiometer Irradiance Monitor Satellite (ACRIMSAT) using ACRIM III. The SOlar Radiation and Climate Experiment (SORCE) was launched in 2003 and is one of the latest satellite missions measuring the TSI. Description of the mission is given by Gutro and Weier [2002]. Using data from SORCE, the TSI variation over 2.5 years is shown in Figure 2.1. In addition to these short-term effects, long term variations in the TSI have been observed. These variations are closely linked to the 11 year period solar cycles discovered Samuel Heinrich Schwabe in 1843. Fröhlich [2006] shows clearly the long term evolution of the TSI using data from different satellites (Figure 2.2).

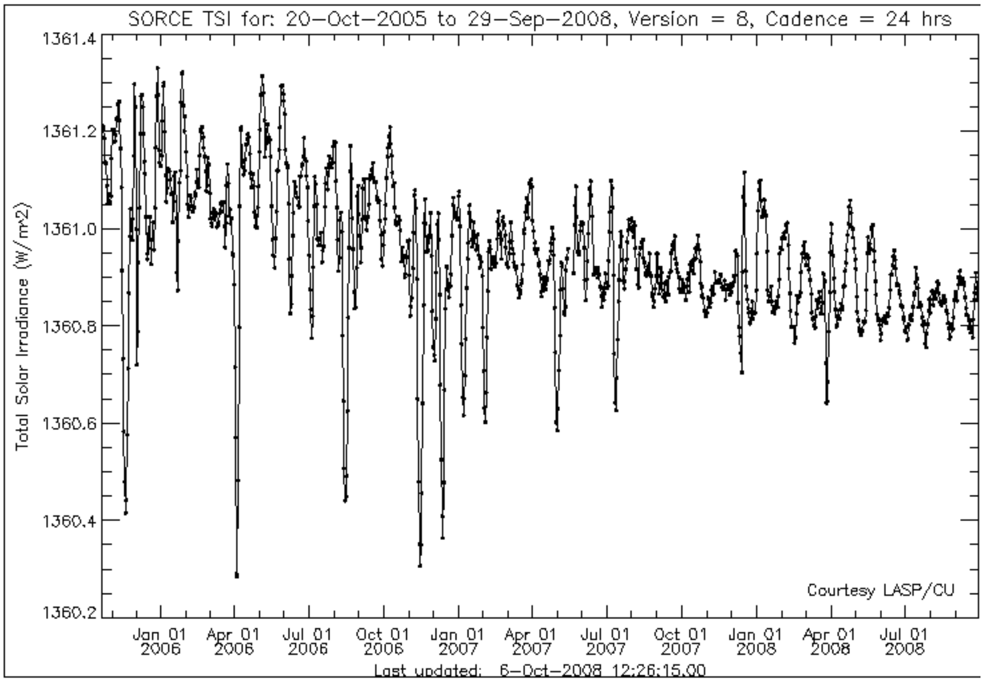

Figure 2.1. Variations of the TSI from SORCE data

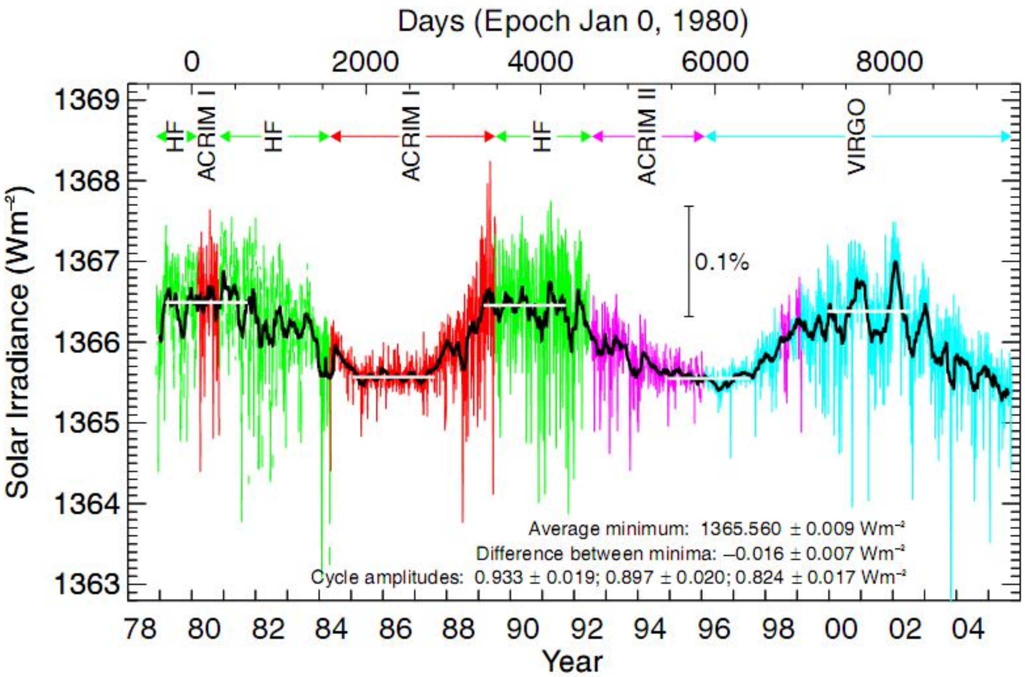

Figure 2.2. Total Solar Irradiance, long term evolution [Fröhlich, 2006].

2.1.3 Reflection

As the light hits a surface, it can be absorbed, transmitted or reflected. We often describe the amount of energy reflected by the material through a reflectivity coefficient. In case of a perfect mirror, this coefficient equals 1 because the light is totally reflected.

When trying to model the reflection of light on a surface, we often assume that the reflection has two components: a specular and a diffuse reflection. In Figure 2.3, the light is reflected totally specularly at an angle θ_r with respect to the normal of the surface; θ_r equals the angle of incidence θ_i. Note that in this case, the ray gets reflected in only one direction as opposed to the diffuse reflection where an incident ray of light is reflected in every direction. In the case of a perfect diffuse surface, the light gets reflected equally in every direction (Figure 2.4) and the reflected light follows Lambert's cosine law: the power per unit solid angle, or radiant intensity, is proportional to the cosine of the angle of incidence. This means that the reflection will appear as bright regardless where the observer stands.

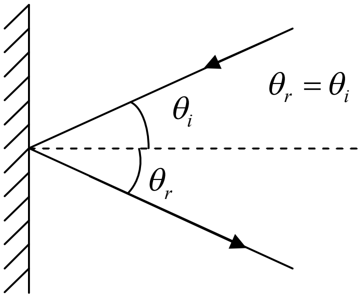

Figure 2.3. Specular reflection on a flat surface

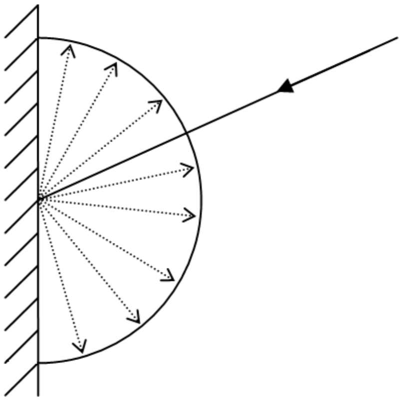

Figure 2.4. Diffuse reflection on a flat surface assuming a Lambert reflectance

2.2 ECLIPSE SEASON

An eclipse is a partial or total obscuration of the sunlight from the satellite by the Earth or by the Moon. Eclipses affect directly the amount of sunlight reaching the satellite and are thus important to determine solar radiation pressure. For example, if the sunlight is totally blocked from the satellite, there is no solar radiation pressure. In addition, the transition into shadow sometime causes major attitude problems such as the one encountered on the GPS Block II/IIAs [Bar-Sever et al., 1996b]. Eclipse seasons are the periods of time when the orientation of the orbital plane with respect to the Sun is such that eclipses occur once per revolution. For GPS satellites, such conditions happen at least twice a year and last a few weeks [Beutler, 2005]. Eclipses last a maximum of about 56 minutes.

A simple way of representing eclipses is to model the Earth's shadow with a cylinder as seen in Figure 2.5. In full shadow, solar radiation pressure is turned off whereas in full sunlight, solar radiation pressure is turned on.

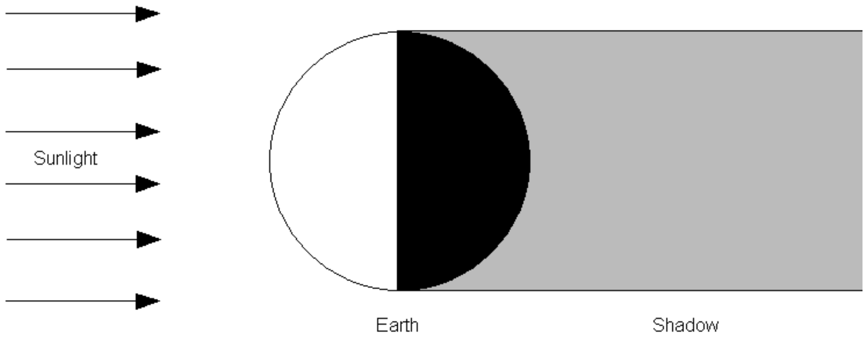

Figure 2.5. Cylindrical shadow model

The problem with this approach is that the transition from light to shadow is discontinuous. To account for those discontinuities we can use the modified back differences method [Anderle, 1973, Rim, 1992]. Another shadow model, more accurate, uses a cone to model the shadow. Figure 2.6 shows how the geometry works in that case. When the satellite enters the umbra, in black in Figure 2.6, the Earth totally obscures the Sun and there is no solar radiation pressure. In the penumbra, in gray in Figure 2.6, the TSI is then scaled by an eclipse factor ν comprised between 0 (full shadow) and 1 (full sunlight). This factor can vary linearly or be proportional to the area of the Sun visible by the satellite.

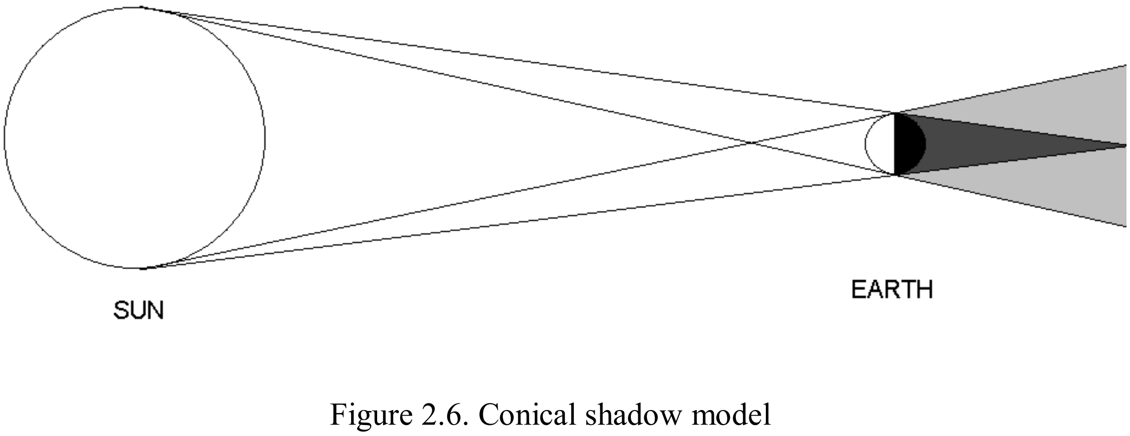

Figure 2.6. Conical shadow model

The cylindrical shadow model, along with the conical shadow model, is available in MSODP. As an example, using the conical shadow model, Figure 2.7 shows the eclipse factor for PRN 03 over one year. Two eclipse seasons are clearly visible before day 100 and after day 250. Figure 2.8 shows the eclipse factor over one day only.

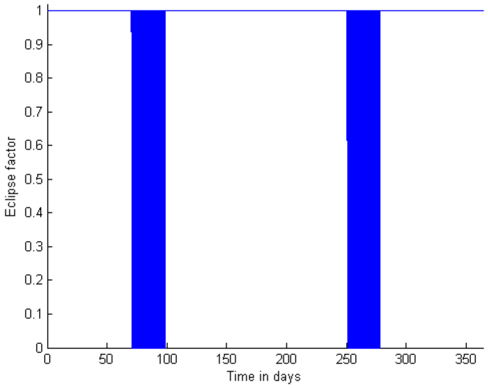

Figure 2.7. Eclipse factor for PRN 03 over one year from 2006 12 31 to 2007 12 29

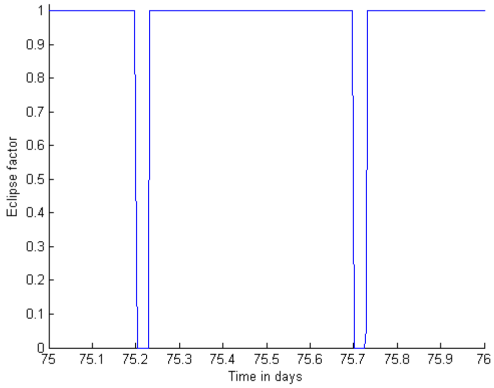

Figure 2.8. Eclipse factor for PRN 03 over one day

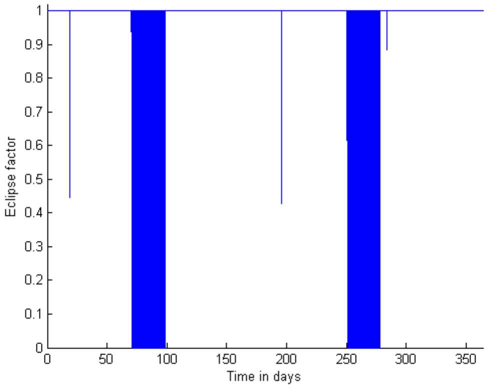

Figure 2.9. Eclipse factor for PRN 03 over one year including the shadowing of the Moon

To be more accurate, the Moon shadowing can also be included. Figure 2.9 is similar to Figure 2.7 but include the Moon. The eclipses due to the Moon are computed with a conical shadow model similar to the one used for the Sun. To be even more comprehensive, other effects could also be modeled. For instance, the light gets refracted when traveling through the Earth's atmosphere. As a consequence, the Sun's disk that is visible from a satellite is flattened. This is shown in details in [Vokrouhlický et al., 1993] and [Vokrouhlický et al., 1994]. In addition, some models include the effect of the oblateness of the Earth. One example is the model based on [Adhya et al., 2004].

Chapter 3

Estimation

3.1 THE MULTI-SATELLITE ORBIT DETERMINATION PROGRAM

To study GPS orbits, we used the Multi-Satellite Orbit Determination Program (MSODP) developed at the Center for Space Research (CSR). A list of examples of orbit determination softwares used worldwide can be found in Table 3.1. MSODP is based on the University of Texas Orbit Processor (UTOPIA) [Schutz and Tapley, 1980]. UTOPIA was designed for the Precise Orbit Determination (POD) of a single satellite. Later on, MSODP was coded to handle the POD of several satellites at the same time. The main goal was here to be able to perform the POD of different GPS satellites along with the POD of another low-Earth satellite such as TOPEX/Poseidon [Rim, 1992].

Orbit Determination Program	Organization
Bernese GPS v4.1	CODE
GIPSY/OASIS-II	JPL
EPOS.P.V2	GFZ

Table 3.1. Orbit Determination Programs

MSODP has different functionalities, or modes, such as orbit propagation, sequential or batch orbit estimation. In orbit propagation mode, MSODP integrates the equation of motions. The batch orbit estimation mode is explained in Section 3.2. For instance, in Section 6.1.1, we used the batch estimator, also called MEASX mode, to fit the IGS data using a specific dynamical model. Another example is the use of MSODP in propagation mode used to make predictions in Section 6.1.2. In addition to these functionalities, as MSODP evolved, different versions were created. We used here MSODP version 2003.1L. However, modifications were made for the purpose of this study such as the integration of the University College London (UCL) Solar Radiation Pressure (SRP) model discussed in Section 4.5.5.

In MSODP, the arc length refers to the total interval of time used for the estimation. The position and velocity are estimated once at the initial epoch. The parameters such as the SRP scale factor or the y-bias parameter can be estimated several times among the same arc. The duration of those estimations is called subarc length. For instance, we can estimate the state using a 10-day arc length and a 0.25 day subarc length. MSODP will then use observations available over 10 days to estimate the initial position and velocity and will provide 4 estimates of the parameters every day.

Finally, to perform numerical integrations MSODP uses a Krogh-Shampine-Gordon fixed-step fixed-order formulation for second-order differential equations [Rim, 1992]. For this study we used a step size of 300 seconds and an order of 14.

3.2 ESTIMATION

3.2.1 Theory

MSODP can be used as a batch estimator. It will try to find a best estimate for the state at a given time in the least square sense based on observations. Here, the state vector contains the satellite position, velocity and parameters to be estimated. For instance, the parameters could be an SRP parameter and a y-bias parameter. The observations used in this study are for the most part the precise ephemerides from IGS described in Section 1.3. The batch estimation is described below and the batch algorithm is shown in Figure

3.1. More details can be found in [Tapley et al., 2004]. The dynamic equations for the state are represented by a non-linear system:

$$\dot{X}(t) = F\left[X(t), t\right] \text{ with } X(t_0) = X_0 \tag{3.1}$$

X_0 is the unknown value we are solving for. The forces acting on the satellite that rule these equations are explained in more depth in Chapter 4. The observations $Y(t)$ are linked to the state by the following equations:

$$Y(t) = G[X(t), t] + \varepsilon(t) \tag{3.2}$$

where

$Y(t)$	is the observation vector at time t
$G[X(t), t]$	is the observation model at time t
$\varepsilon(t)$	is the error at time t

Both the equation of the state, Equation (3.1), and the equation for the observation, Equation (3.2), are then linearized about a nominal trajectory. The nominal trajectory is obtained by integrating the following system of non-linear equations:

$$\dot{X}^* = F\left[X^*(t), t\right] \quad \text{and} \quad X^*(t_0) = X_0^* \tag{3.3}$$

where X_0^* is an initial guess for X_0

We further introduce $x(t)$, the difference between the state and the nominal state:

$$x(t) = X(t) - X^*(t) \tag{3.4}$$

Taking the derivatives of Equation (3.4), we can write:

$$\dot{x}(t) = \dot{X}(t) - \dot{X}^*(t) = F\left[X(t), t\right] - F\left[X^*(t)\right] \tag{3.5}$$

Using a Taylor series expansion, we can expand $F\left[X(t),t\right]$ about the nominal trajectory as follows:

$$F\left[X(t),t\right]=F\left[X^{*}(t),t\right]+\left(\frac{\partial F}{\partial X}\right)^{*}x(t)+o\left[x(t)\right] \tag{3.6}$$

Using Equations (3.5) and (3.6) and neglecting the second order term and higher we then obtain the variational equations:

$$\dot{x}(t)=A(t)\cdot x(t) \tag{3.7}$$

where

$$A(t)=\left(\frac{\partial F}{\partial X}\right)^{*}$$

Similarly, we can introduce the difference between the actual observations and the observations taken on the nominal path. These differences, or residuals, can be expressed as:

$$y(t)=Y(t)-Y^{*}(t) \tag{3.8}$$

Using Equation (3.8) and Equation (3.2) and replacing $Y^{*}(t)$ by $G[X*(t),t]$, we get:

$$y(t)=G[X(t),t]+\varepsilon(t)-G[X^{*}(t),t] \tag{3.9}$$

We can expand $G[X(t),t]$ about the nominal path using a Taylor series as:

$$G[X(t),t]=G[X^{*}(t),t]+\left(\frac{\partial G}{\partial X}\right)^{*}x(t)+o\left[x(t)\right] \tag{3.10}$$

Thus, neglecting higher order terms, Equation (3.9) becomes:

$$y(t) = \underbrace{\left(\frac{\partial G}{\partial X}\right)^{*}}_{\widetilde{H}(t)} x(t) + \varepsilon(t) \tag{3.11}$$

We use the state transition matrix ϕ to map Equation (3.11) back to the initial state:

$$y(t) = H(t) \cdot x(t_0) + \varepsilon(t) \tag{3.12}$$

where

$$H(t) = \phi(t, t_0) \cdot \widetilde{H}(t) \tag{3.13}$$

The state transition matrix relates the state taken at an epoch t to the state at epoch t_0:

$$X(t) = \phi(t, t_0) \cdot X(t_0) \tag{3.14}$$

Thus:

$$x(t) = \phi(t, t_0) \cdot x(t_0) \tag{3.15}$$

Taking the derivatives of Equation (3.15):

$$\dot{x}(t) = \dot{\phi}(t, t_0) \cdot x(t_0) + \phi(t, t_0) \cdot \underbrace{\dot{x}(t_0)}_{=0} \tag{3.16}$$

Using Equation (3.7) leads to:

$$A(t) \cdot x(t) = \dot{\phi}(t, t_0) \cdot x(t_0) \tag{3.17}$$

Replacing $x(t)$ using Equation (3.15) gives:

$$A(t) \cdot \phi(t, t_0) \cdot x(t_0) = \dot{\phi}(t, t_0) \cdot x(t_0) \tag{3.18}$$

$$\Rightarrow \left[A(t) \cdot \phi(t, t_0) - \dot{\phi}(t, t_0)\right] \cdot x(t_0) = [0] \tag{3.19}$$

$$\Rightarrow \begin{cases} A(t) \cdot \phi(t,t_0) - \dot{\phi}(t,t_0) = [0] \\ or \\ x(t_0) = [0] \end{cases} \tag{3.20}$$

Assuming the initial state being different than the initial nominal state, or $x(t_0) \neq 0$ leads to:

$$\dot{\phi}(t,t_0) = A \cdot \phi(t,t_0) \qquad \text{with } \phi(t_0,t_0) = I \tag{3.21}$$

Integrating Equation (3.21) gives us the state transition matrix for any time t. In addition, we can combine the observation equation, Equation (3.12), for the observations at the different times:

$$\underbrace{\begin{bmatrix} y(t_1) \\ y(t_2) \\ \vdots \\ y(t_n) \end{bmatrix}}_{\underline{y}} = \underbrace{\begin{bmatrix} H(t_1) \\ H(t_2) \\ \vdots \\ H(t_n) \end{bmatrix}}_{\underline{H}} \cdot x(t_0) + \begin{bmatrix} \varepsilon(t_1) \\ \varepsilon(t_2) \\ \vdots \\ \varepsilon(t_n) \end{bmatrix} \tag{3.22}$$

$$\Rightarrow \underline{y} = \underline{H} \cdot x(t_0) + \underline{E} \tag{3.23}$$

We solve Equation (3.23) for the best estimate by using weighted least square:

$$\hat{x}_0 = \left(H^T W H\right)^{-1} H^T W \underline{y} \tag{3.24}$$

where

$\hat{x}_0$	is the best estimate
$\left(H^T W H\right)^{-1}$	is the covariance matrix
W	is the weight matrix used to emphasize certain observations

3.2.2 Batch Algorithm

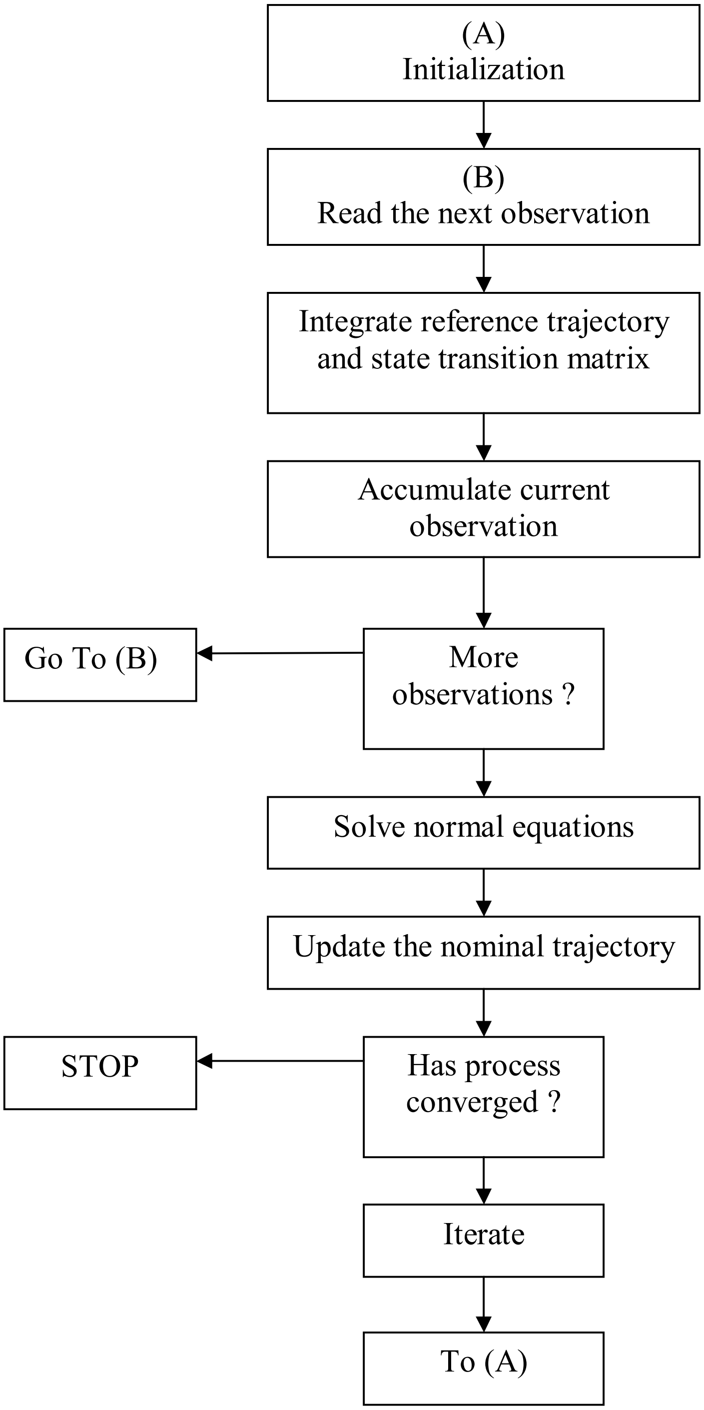

Figure 3.1. Batch Algorithm [Tapley et al., 2004]

Chapter 4

Forces

4.1 GENERAL MOTION

The equations of motion of a GPS satellite are based on the two body problem. Assuming the Earth and the satellite are perfect spheres with uniform density of mass M_{Earth} and M_{Sat} respectively, we can express these equations in an inertial frame as follows:

$$\ddot{\vec{r}} = -\frac{G \cdot \left(M_{Earth} + M_{Sat}\right)}{r^3}\vec{r} \tag{4.1}$$

where

$\vec{r}$ is the position of the satellite with respect to the center of mass of the Earth

G is the gravitational constant

Although the mass of a GPS satellite varies among the different Blocks, its value is negligible compared to the mass of the Earth. Equation (4.1) can then be simplified to the following:

$$\ddot{\vec{r}} = -\frac{\mu}{r^3}\vec{r} \tag{4.2}$$

where $\mu = G \cdot M_{Earth}$

4.2 PERTURBED MOTION

The conic section solution of Equation (4.2) does not accurately describe the actual motion. Indeed, several perturbing forces need to be taken into account to get a more comprehensive and accurate representation. Equation (4.2) can be rewritten as:

$$\ddot{\vec{r}} = -\frac{\mu}{r^3}\vec{r} + \vec{f}_{perturbations} \tag{4.3}$$

where $\vec{f}_{perturbations}$ is the sum of all perturbing forces. Note that $\vec{f}_{perturbations}$ is a force per unit mass and thus has the same units as an acceleration. These perturbing forces are typically classified into two categories: gravitational forces and non-gravitational forces. We can then write $\vec{f}_{perturbations}$ as:

$$\vec{f}_{perturbations} = \vec{f}_{gravitational} + \vec{f}_{non-gravitational} \tag{4.4}$$

where

$\vec{f}_{gravitational}$ equals to the sum of the gravitational perturbations

$\vec{f}_{non-gravitational}$ equals to the sum of the non-gravitational perturbations

4.3 GRAVITATIONAL PERTURBATIONS

Gravitational perturbations can be decomposed into several different contributions as follows:

$$\vec{f}_{gravitational} = \vec{f}_{oblateness} + \vec{f}_{\substack{ocean\\tides}} + \vec{f}_{\substack{Earth\\tides}} + \vec{f}_{rotational} + \vec{f}_{N-body} + \vec{f}_{relativity} \tag{4.5}$$

where

$\vec{f}_{oblateness}$ represents the effect of the non-sphericity of the Earth

$\vec{f}_{\substack{ocean\\tides}}$ represents the effect of the ocean tides

$\vec{f}_{\substack{Earth\\tides}}$	represents the effect of the Earth tides
$\vec{f}_{rotational}$	represents the effect due to the Earth's rotational deformation
$\vec{f}_{N-body}$	represents the effect due to the N-body perturbation
$\vec{f}_{relativity}$	represents the effect due to general relativity

4.3.1 Non-sphericity of the Earth

The Earth is not a perfect sphere of uniform density. The force produced by the mass distribution of the Earth is equal to the gradient of the geopotential:

$$\vec{f}_{geopotential} = \vec{\nabla} U \tag{4.6}$$

Kaula [1966] described this potential in terms of spherical harmonics and orbit elements as follows:

$$\begin{aligned} U = {} & \frac{\mu}{r}\left[1-\sum_{n=2}^{\infty}\left(\frac{a_e}{r}\right)^n \cdot J_n P_n(\sin\varphi)\right] \\ & +\frac{\mu}{r}\left[\sum_{n=2}^{\infty}\sum_{m=1}^{n}\left(\frac{a_e}{r}\right)^n \left\{C_{nm}\cos(m\lambda)+S_{nm}\sin(m\lambda)\right\}\cdot P_{nm}(\sin\varphi)\right] \end{aligned} \tag{4.7}$$

where

a_e	is the mean equatorial radius of the Earth
$\mu = G \cdot M_{Earth}$	where G is the gravitational constant and M_{Earth} the mass of the Earth
φ	is the geocentric latitude of the satellite
λ	is the geocentric longitude of the satellite
r	is the geocentric distance of the satellite from the center of the Earth
J_n	are the zonal harmonics

C_{nm} and S_{nm}	are the sectoral and tesseral harmonics
P_{nm}	are the Legendre Polynomials

The term $U_0 = \frac{\mu}{r}$ represents the Earth as a spherical body. However, the remaining terms are perturbations due to the non-sphericity of the Earth. The most important of these contributions is the effect due to the degree-2 term J_2. It accounts for 95% of the gravitational force other than the U_0 term [Tapley et al., 2004]. Using only the U_0 term and the J_2 term, the gravitational potential can be approximated by:

$$U \approx \frac{\mu}{r} - \frac{\mu}{r}\left(\frac{a_e}{r}\right)^2 J_2 P_2(\sin\varphi) \tag{4.8}$$

where

a_e	is the mean equatorial radius of the Earth
$\mu = G \cdot M_{Earth}$	where G is the gravitational constant and M_{Earth} the mass of the Earth
φ	is the geocentric latitude of the satellite
r	is the geocentric distance of the satellite from the center of the Earth
J_2	is the degree-2 zonal harmonic coefficient
P_2	is the degree two Legendre polynomial, $P_2 = \frac{3}{2}\sin^2\varphi - \frac{1}{2}$

Neglecting terms of order e and higher, it can be shown from Kaula [1966] that the potential can be decomposed into a term depending on *r*, a secular and a periodic part as seen in Equation (4.9).

$$U = U_0 + U_S + U_P + o(e) \tag{4.9}$$

where

$$U_0 = \frac{\mu}{r}$$

$$U_S = -\frac{\mu}{a}\left(\frac{a_e}{a}\right)^2 J_2\left(\frac{3}{4}\sin^2 i\right) - \frac{1}{2}$$

$$U_P = \frac{\mu}{a}\left(\frac{a_e}{a}\right)^2 J_2\left(\frac{3}{4}\sin^2 i\cos(2\omega + 2M)\right)$$

Moreover, Kaula describes the effects of U_S and U_P on the orbital elements. The following equations represent the effects of U_S on the mean orbital elements, as shown by Kaula [1966]:

$$\begin{cases} \dot{a} = 0 \\ \dot{e} = 0 \\ \dot{i} = 0 \end{cases} \qquad \begin{cases} \dot{\Omega} = -\frac{3}{2} J_2 n\left(\frac{a_e}{a}\right)^2 \cos i \\ \dot{\omega} = \frac{3}{4} J_2 n\left(\frac{a_e}{a}\right)^2 (5\cos^2 i - 1) \\ \dot{M} = \bar{n} + \frac{3}{4} J_2 n\left(\frac{a_e}{a}\right)^2 (3\cos^2 i - 1) \end{cases} \tag{4.10}$$

where

$n = \sqrt{\frac{\mu}{a^3}}$ is the mean motion and $\bar{n} = \sqrt{\frac{\mu}{\bar{a}^3}}$ with $\bar{a}$ being the mean value

Equations (4.10) show that the time rate of change of the semimajor axis, the eccentricity or the inclination equals to 0, in an average sense. On the other hand, the rate of change of the remaining orbital elements can be considered to be constants. The periodic effects can be expressed using Kaula (1966). For instance, by neglecting terms of degree e and higher, the semimajor axis can be expressed by:

$$a(t) \approx \bar{a} + 3\bar{n}\bar{a}J_2\left(\frac{a_e}{\bar{a}}\right)^2 \sin^2 \bar{i}\,\frac{\cos(2\omega(t)+2M(t))}{2\dot{\omega}+2\dot{M}} \qquad (4.11)$$

Where (¯) represents the mean value of the element. Equation (4.11) shows a twice per revolution frequency, that is to say four cycles per day. As an illustration, Figure 4.1 shows the periodical evolution of the semimajor axis for PRN 25 over half a day.

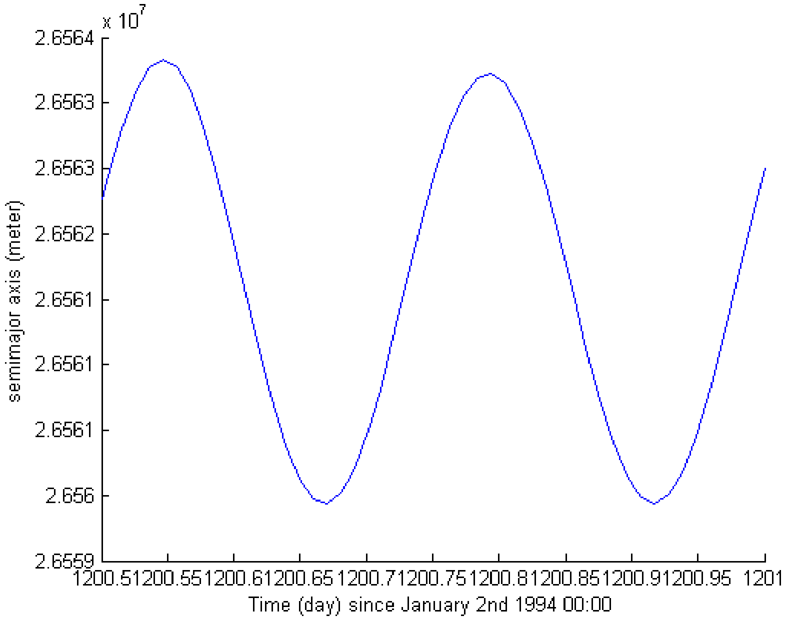

Figure 4.1. PRN 25, semimajor axis, evolution over half a day

For the purpose of this study, we used the Joint Gravity Model 3 (JGM-3) [Tapley et al., 1996]. Comparisons [Froideval, 2004] using JGM-3 or a more recent gravitational field model like GGM01 obtained with the Gravity Recovery and Climate Experiment (GRACE) showed that the differences had only very small effects. This is caused by the high altitude of the GPS satellites. In addition, for computational purposes, only terms of up to degree and order 12 were used. The higher degree and order coefficients can be neglected due to the high altitude of GPS satellites.

4.3.2 Ocean Tides

The contribution to the gravitational field model that results from the redistribution of the ocean mass produced by the Sun and the Moon, e.g., ocean tides, can be expressed with the following formula [Eanes et al., 1983, Rim 1992]:

$$\begin{aligned} \Delta U_{\substack{ocean\\tides}} &= 4\pi \cdot G \cdot \rho_w \cdot a_e \times \ldots \\ \ldots \times \sum_k \sum_{l=0}^{\infty} \sum_{m=0}^{l} \sum_{+}^{-} & \left\{ \frac{l + k_l'}{2l+1} \left(\frac{a_e}{r} \right)^{l+1} \left[C_{klm}{}^{\pm} \cdot \cos(\Theta_k \pm m\lambda) + S_{klm}{}^{\pm} \cdot \sin(\Theta_k \pm m\lambda) \right] \cdot P_{lm}(\sin\varphi) \right\} \end{aligned} \tag{4.12}$$

where

G	is the gravitational constant
a_e	is the mean equatorial semimajor axis of the Earth
ρ_w	is the mean density of seawater
k	is the ocean tide constituent index
k_l'	is the load Love number of degree l
$C_{klm}{}^{\pm}, S_{klm}{}^{\pm}$	are the prograde and retrograde tide coefficients
Θ_k	is the Doodson argument for constituent k

4.3.3 Solid Earth tides

The mass distribution of the solid Earth is also affected by other bodies, primarily the Sun and the Moon. The correction to the geopotential is given by the following formula [Wahr et al., 1981, Rim, 1992]:

$$\begin{aligned} \Delta U_{\substack{Earth\\tide}} &= \frac{GM_E}{a_e^2} \sum_{l=2}^{3} \sum_{m=0}^{l} \sum_{k(l,m)} H_k e^{i(\Theta_k + \chi_k)} k_k{}^0 \times \ldots \\ \ldots &\times \left[\left(\frac{a_e}{r} \right)^{l+1} Y_m^l(\phi, \lambda) + k_k^+ \left(\frac{a_e}{r} \right)^{l+3} Y_m^{l+2}(\phi, \lambda) \right] \end{aligned} \tag{4.13}$$

where

$Y^l_m(\phi,\lambda)$	$= (-1)^m \sqrt{\dfrac{(2l+1)\cdot(l-m)!}{4\pi\cdot(l+m)!}} \cdot P_{lm}(\sin\phi)e^{im\lambda}$
$P_{lm}(\sin\phi)$	is the associated Legendre function of degree l and order m
H_k	is the frequency dependent tidal amplitude in meters
Θ_k and χ_k	are the Doodson argument and phase correction for constituent k ($\chi_k = 0$, if l-m is even, $\chi_k = -\dfrac{\pi}{2}$, if l-m is odd)
k^0_k, k^+_k	are the Love numbers for constituent k
r, ϕ, λ	are the radial distance, the geocentric latitude, and the longitude of the satellite, respectively

Note that the sum over k means that for each (l,m) combination, there is a unique list of tidal frequencies k.

4.3.4 The N-body perturbation

GPS satellites also experience gravitational effects from other bodies such as the Moon and the Sun (as well as planets such as Jupiter and Venus). Known as the N-body perturbations, but also referred to as third-body effects, the resulting forces are described as follows:

$$\vec{f}_{N-body} = \sum_{j=1}^{n_p} \mu_j \cdot \left(\frac{\vec{\Delta}_j}{\Delta_j^3} - \frac{\vec{r}_j}{r_j^3}\right) \tag{4.14}$$

where

n_p is the number of additional bodies

μ_j is the gravitational parameter of the body j

$\vec{\Delta}_j$ is the position vector of the body j with respect to the satellite

$\vec{r}_j$ is the position vector of the body j with respect to the Earth

The third body perturbation is similar to the J_2 effect. The variations in orbit elements produced by the Sun and the Moon can be decomposed into secular variations and periodic variations. The longitude of the ascending node, the argument of perigee and the mean anomaly show secular variations [Tapley et al., 2004]. In addition to the secular variations, periodic effects can be seen in all the orbital elements with semiannual variations due to the Sun and semimonthly variations due to the Moon. As an example, Figure 4.2 and Figure 4.3 show the perturbations due to the Sun and the Moon on the semimajor axis for actual satellite PRN 03. Figure 4.3 is an expansion of Figure 4.2. These Figures are based on the IGS precise ephemerides.

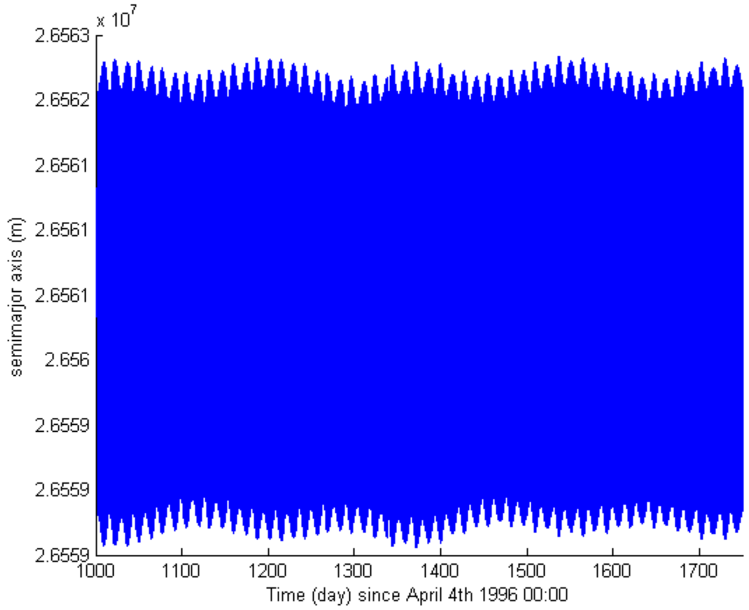

Figure 4.2. PRN 03, semimajor axis, effect of the Sun

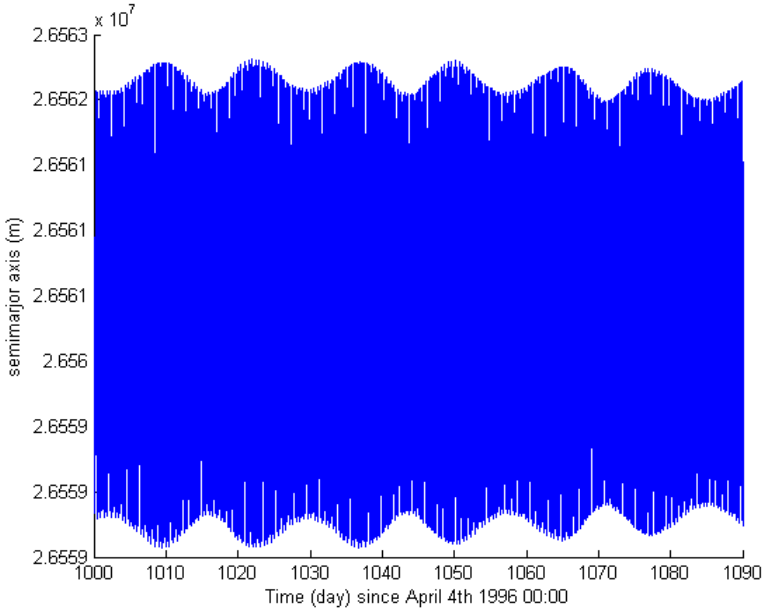

Figure 4.3. PRN 03, semimajor axis, effect of the Moon

4.3.5 Rotational Deformation

Assuming the Earth is a non-rigid body, its rotation creates a centrifugal force that causes a deformation of the mass distribution, which in turn varies with time as the result of variations in the directional magnitude of the Earth's angular velocity vector. This change in the geopotential can be stated as [Rim, 1992]:

$$\begin{aligned}
\Delta U = {} & \frac{r^2}{6}\left(\omega_1^2 + \omega_2^2 - 2\cdot\omega_3^2\right)\cdot P_{20}\cdot\sin\phi \\
& -\frac{r^2}{3}\cdot\left(\omega_1\omega_2\cdot\cos\lambda + \omega_2\omega_3\cdot\sin\lambda\right)\cdot P_{21}\cdot\sin\phi \\
& +\frac{r^2}{12}\left[\left(\omega_2^2 - \omega_1^2\right)\cdot\cos(2\lambda) - 2\omega_1\omega_2\sin(2\lambda)\right]\cdot P_{22}\cdot\sin\phi
\end{aligned} \tag{4.15}$$

where

$$\begin{cases} \omega_1 = \Omega\cdot m_1 \\ \omega_2 = \Omega\cdot m_2 \\ \omega_3 = \Omega\cdot(1+m_3) \end{cases} \qquad \begin{aligned} & m_1 = x_p \text{ (polar motion parameter)} \\ & m_2 = y_p \\ & m_3 = \frac{d(UT1-TAI)}{d(TAI)} \end{aligned}$$

and

Ω is the mean angular velocity of the Earth

TAI is the International Atomic Time

UT1 is the Universal Time

4.3.6 General RelativiTy

The effects of general relativity on GPS orbit determination should be included for high accuracy applications. The induced acceleration is formulated as [Ries et al., 1988]:

$$\vec{a}_R = \frac{\mu}{c^2 r^3}\left\{\left[2\cdot(\beta+\gamma)\frac{\mu}{r} - \gamma\cdot\left(\dot{\vec{r}}\cdot\dot{\vec{r}}\right)\right]\cdot\vec{r} + 2\cdot(1+\gamma)\cdot\left(\vec{r}\cdot\dot{\vec{r}}\right)\cdot\dot{\vec{r}}\right\} \tag{4.16}$$

where

c	is the speed of light
$\vec{r},\dot{\vec{r}}$	are the position and velocity vectors of the satellite in geocentric non-rotating coordinates
β,γ	are parameters in the isotropic Parameterized Post-Newtonian metric, which are exactly equal to one in General Relativity.

4.4 NON-GRAVITATIONAL PERTURBATIONS

The non-gravitational perturbations can be separated as:

$$\vec{f}_{non-gravitational} = \vec{f}_{SRP} + \vec{f}_{ERP} + \vec{f}_{y-bias} + \vec{f}_{C_t} + \vec{f}_{re-radiation} + \vec{f}_{antenna} + \vec{f}_{others} \tag{4.17}$$

where

$\vec{f}_{SRP}$	is the force due to solar radiation pressure
$\vec{f}_{ERP}$	is the force due to earth radiation pressure
$\vec{f}_{y-bias}$	is the y-bias force
$\vec{f}_{Ct}$	is an along track force
$\vec{f}_{re-radiation}$	is a force due to re-radiation by the spacecraft
$\vec{f}_{antenna}$	is the force due to the antenna recoil

$\vec{f}_{others}$ includes all the unmodeled forces

Note that at the high altitude of GNSS satellites, atmospheric drag can be neglected. Table 4.1 provides order of magnitudes for the different non-gravitational forces (based, in part, on Ziebart et al., 2005)

Force	**Acceleration (m/s^2)**
Solar Radiation Pressure	1×10^{-7}
Thermal re-radiation	1×10^{-8}
y-bias	1×10^{-9}
Earth Radiation Pressure	1×10^{-9}
Along track	1×10^{-9}
Antenna recoil	1×10^{-10}

Table 4.1. Order of magnitude of the non-gravitational forces

4.4.1 Solar Radiation Pressure

Due to the high altitude of the GPS satellites, the SRP perturbation becomes the limiting factor in modeling the non-gravitational forces. Figure 4.4 shows the effect of SRP depending on the distance from the center of the Earth [Montenbruck and Gill, 2000]. As seen in Chapter 2, the SRP acceleration is caused by the incident ray of light from the Sun on the satellite. A description of different ways of modeling SRP is described in Section 4.5. A brief description of short-term effects of SRP on the orbital elements is presented in Section 4.7.

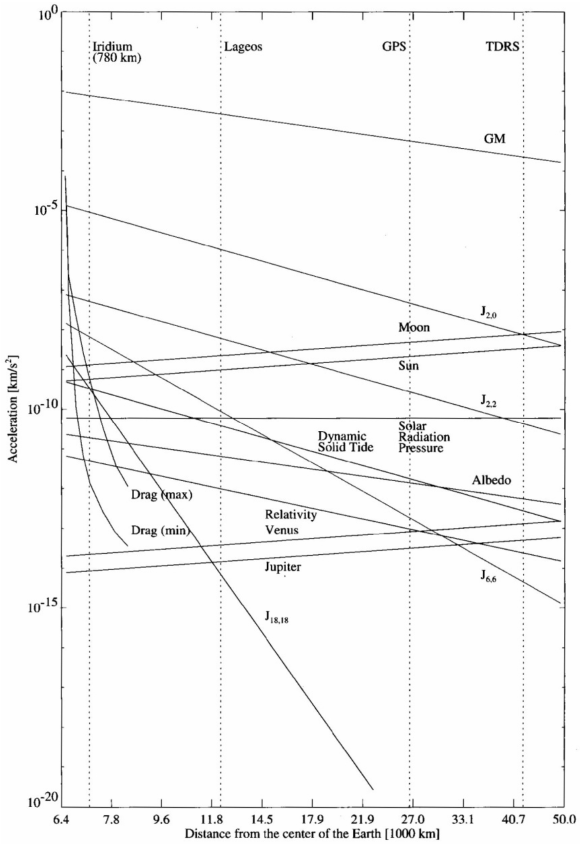

Figure 4.4. Order of magnitude of various perturbations of a satellite orbit [Montenbruck and Gill, 2000].

4.4.2 Y-bias

Early observations of the GPS constellation showed an unknown force acting along the solar panels rotation axis. It was soon called the y-bias force because of the y axis being aligned with the solar panels in the body fixed frame (Section 4.5.2). Since the solar panels are articulated to present the maximum area to the Sun, the rotation axis is essentially perpendicular to the Sun direction. One possible origin could be a solar panel misalignment as seen in Figure 4.5. Fliegel et al. [1992] also suggest that misalignment angles of about 0.5° to 1° in the solar sensors would account for the y-bias force. A third possible source could be the energy radiated through the louvres along the solar panel direction. Although the previous explanations seem reasonable, the exact origin of this force remains unclear and other possible causes cannot be ignored. In this study, to compute the y-bias force, we estimate a empirical parameter along the solar panel axis to account for the force as follows:

$$\vec{f}_{y-bias} = C_{y-bias} \cdot \vec{u}_y \tag{4.18}$$

where

C_{y-bias}	is a positive or negative constant
$\vec{u}_y$	is a unit vector in the y direction

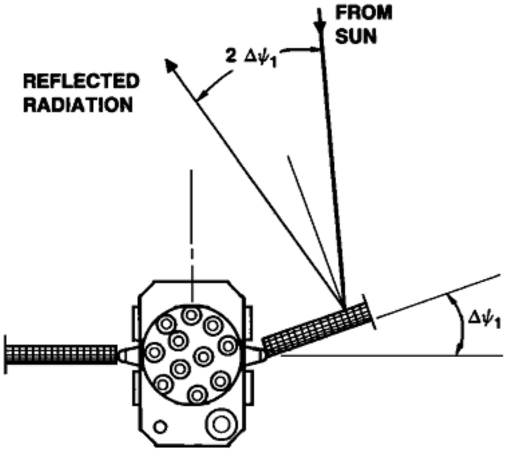

Figure 4.5. Solar panel misalignment [Fliegel et al., 1992]

4.4.3 Earth radiation pressure

Apart from the direct solar radiation pressure, GPS satellites are also influenced by the energy reflected and emitted by the Earth called Earth Radiation Pressure (ERP). The model used in MSODP is based on the ERP model described in [Knocke, 1989] and the resulting force can be expressed as [Rim, 1992]:

$$\vec{f}_{ERP} = (1+\eta_E)\cdot A \cdot \frac{A_c}{m \cdot c} \cdot \sum_{j=1}^{N} \left[\vec{r} \cdot \left(a \cdot E_s \cdot \tau \cdot \cos\theta_s + e \cdot M_B \right) \right]_j \tag{4.19}$$

where

η_E is the satellite reflectivity for ERP

A is the projected, attenuated area of a surface element of the Earth

A_c is the cross sectional area of the satellite

m is the mass of the satellite

c is the speed of light

N is the number of segments

τ	equals to 0 if the center of element j is in darkness and equals to 1 if the center of element j is in daylight
a,e	are the albedo and emissivity of element j
E_S	is the solar momentum flux density at 1 astronomical unit
θ_S	is the solar zenith angle
M_B	is the exitance of the Earth, which is the total amount of radiative flux leaving a point on a surface of the Earth into all directions above the surface.
$\vec{r}$	is the unit vector from the center of the element j to the satellite

ERP if of the same order of magnitude as the y-bias force, but the nature of ERP is complex since it depends on reflected radiation (albedo) and emitted radiation (emissivity). To isolate the y-bias effects, ERP was ignored in this study.

4.4.4 Along track force (or C_t force)

As previously mentioned, at this altitude, atmospheric drag can be neglected. However, presence of a small perturbation along an axis tangential to the velocity can be assumed and an empirical parameter called C_t in this study will be used, which is defined as follows:

$$\vec{f}_{C_t} = C_t \cdot \vec{u}_t \tag{4.20}$$

where

C_t	is an empirical estimated parameter
$\vec{u}_t$	is a unit vector tangential to the velocity vector

This along track force or C_t force also exhibits a twice per day effect, as seen in [Froideval, 2004]. One possible source for the C_t force could be thermal effects like thermal re-radiation.

4.4.5 Thermal re-radiation

When the sunlight illuminates the spacecraft, it can be reflected (as described in Section 2.1.3), transmitted or absorbed. The temperature of the spacecraft increases with the amount of energy absorbed. Absorbed radiation can be re-emitted which, in turn, will generate a force. Modeling the temperature of the spacecraft is a key to obtain the force caused by thermal re-radiation. The thermal re-radiation force is believed to be up to 10% of the SRP force as seen in [Adhya et al., 2005]. An early attempt to model the thermal forces on GPS satellites can be found in Vigue [1994]. More detailed methods that require precise knowledge of the spacecraft thermal properties are described in Adhya et al. [2005]. In this study, thermal re-radiation is typically embedded in the SRP model such as in the ROCK42 model described in Section 4.5.2 or in the empirical Extended CODE Orbit Model (ECOM) model described in Section 4.5.3.

4.4.6 Antenna recoil

The signal transmitted by a GPS satellite's antenna also creates a small perturbation of the order of 2.4×10^{-10} m/s^2 [Ziebart et al., 2005]. The induced force lies along the antenna direction, directed opposite of the transmitted signal. In this study, the antenna thrust is embedded in the UCL SRP model described in Section 4.5.5.

4.4.7 Unmodeled perturbation

After taking into account all the non-gravitational perturbation described above, small unmodeled perturbation remain. They can be due to unknown effects or mismodeling of the previous forces. Empirical parameterization can here be used to compensate for the remaining errors.

4.5 SRP MODELING

4.5.1 The Cannonball model

An early approach to modeling SRP consists in approximating a satellite by a simple sphere. As seen in [Tapley and Ries, 1987], the force induced by SRP under this assumption becomes:

$$\vec{a}_{SRP} = -P \cdot \nu \cdot (1+\eta) \cdot \frac{A}{m} \cdot \vec{u} \tag{4.21}$$

where

P	is the momentum flux of the solar radiation
η	is the reflectivity coefficient of the satellite
A	is the cross-sectional area of the spacecraft normal to the Sun
m	is the mass of the spacecraft
ν	is the eclipse factor
$\vec{u}$	is the unit vector from the satellite to the Sun

The model above is implemented in MSODP. The estimated scale factor is the reflectivity coefficient, with an approximate value of 0.2. In MSODP, the momentum flux of the solar radiation is further expressed as:

$$P = \left(\frac{S}{c}\right) \cdot \left(\frac{R}{r}\right)^2 \tag{4.22}$$

where

P	is the momentum flux of the solar radiation
S	is the solar flux constant with an approximated value of 1367.2 W/m^2
c	is the speed of light
R	is one Astronomical Unit or 1.49598 x 10^{11} m
r	is the distance form the Sun

In the above equation, it is worth noting that the solar flux constant is scaled by the distance to the Sun. Due to its simplicity, the Cannonball model is commonly used. However, more evolved SRP models have tried to approximate nonspherical satellites with better accuracy.

4.5.2 The Rockwell model

The Rockwell model was initially developed by Rockwell International, prime DOD contractor of GPS satellites Block I and Block II. Based on the work by Porter [1976], IBM and The Aerospace Corporation designed the computer programs known as ROCK4 and ROCK42, for Block I and Block II satellites, respectively [Fliegel et al., 1992]. For each Block, a standard version and a more comprehensive 'Thermal' version were created. In this study, the ROCK42 model was also used for Block IIR satellites.

The body-fixed frame used here is described in Figure 4.6. The Z axis is parallel to the antennas boresight and the positive direction points toward the center of mass of the Earth. The positive X direction points toward the half-plane that contains the Sun. The Y axis completes the right-handed system and lies along the solar panel axis.

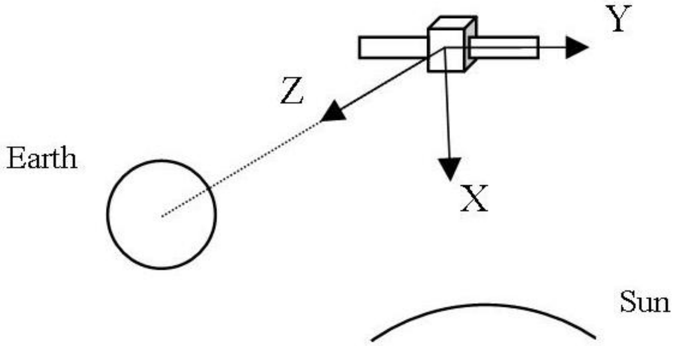

Figure 4.6. The body fixed frame

Here, the spacecraft is modeled by flat surfaces and cylinders and precise knowledge of the materials used is important. In this model, the solar rays are approximated by a perfectly diffuse beam and a perfectly specular beam. According to Fliegel et al. [1992], SRP is essentially decomposed into 3 components:

- a normal and a shear component due to the specular reflection. Here, the surface behaves like a perfect mirror. For a flat surface, the equations for the corresponding accelerations are as follows:

$$\begin{aligned} a_{f,N} &= -\left(\frac{A \cdot E}{c}\right) \cdot (1+\mu\nu) \cdot \cos^2\theta \\ a_{f,S} &= -\left(\frac{A \cdot E}{c}\right) \cdot (1-\mu\nu) \cdot \sin\theta \cdot \cos\theta \end{aligned} \tag{4.23}$$

where

A is the cross-sectional area exposed to sunlight (m^2)

E	is the Total Solar Irradiance
c	is the speed of light (m/s)
ν	is the reflectivity coefficient
μ	is the specularity coefficient
θ	is the angle of incidence of the ray on the surface

- a diffuse component, normal to the surface that can be shown to be two-thirds of the specular component. The equation for a flat surface for the diffuse component is the following:

$$a_{f,D} = -\frac{2}{3}\left(\frac{A \cdot E}{c}\right) \cdot \nu \cdot (1-\mu)\cos\theta \tag{4.24}$$

For a cylindrical surface, the equations are slightly different [Fliegel et al. 1992]:

$$\begin{cases} a_{c,N} = -\left(\dfrac{A \cdot E}{c}\right) \cdot (1+\dfrac{\mu\nu}{3}) \cdot \cos^2\theta \\ a_{c,S} = -\left(\dfrac{A \cdot E}{c}\right) \cdot (1-\mu\nu) \cdot \sin\theta \cdot \cos\theta \\ a_{c,D} = -\dfrac{\pi}{6}\left(\dfrac{A \cdot E}{c}\right) \cdot \nu \cdot (1-\mu)\cos\theta \end{cases} \tag{4.25}$$

The previous equations are used in the standard models, S10 for Block I and S20 for Block II. The thermal models, T10 and T20, include the energy re-radiated by the satellite as heat in both the body and the solar panels [Vigue and Schutz, 1991]. For a flat surface, the diffuse component then becomes:

$$a_{f,D} = -\frac{2}{3}\left(\frac{A \cdot E}{c}\right) \cdot \nu \cdot (1-\mu\nu)\cos\theta \tag{4.26}$$

and for a cylindrical surface:

$$a_{c,D} = -\frac{\pi}{6}\left(\frac{A \cdot E}{c}\right) \cdot \nu \cdot (1-\mu\nu)\cos\theta \tag{4.27}$$

To be computationally efficient, the model is then fit using a short Fourier series as seen in Equations (4.28):

$$\begin{cases} a_x = -8.96 \cdot \sin(B) + 0.16 \cdot \sin(3B) + 0.10 \cdot \sin(5B) - 0.07 \cdot \sin(7B) \\ a_z = -8.43 \cdot \cos(B) \end{cases} \tag{4.28}$$

This model is implemented in MSODP and a scale factor that multiplies a_x and a_z is estimated. If the model were to be a perfect representation, then the value of the scale factor would be one.

The Rockwell model is mainly limited by the complexity of the spacecraft as the antenna structure is not fully modeled along with other smaller parts, such as the thrusters. Note also, that it only takes into account the first intersection between rays of light and the surface of the spacecraft. Finally, the model does not account for aging effects that would change substantially the specularity coefficients as given in Fliegel et al. [1992].

4.5.3 The Extended CODE Model

Formulated by the CODE, the ECOM model is a purely empirical model developed for Block II/IIA satellites. It uses an optimal parameterization of SRP shown to be of an order of magnitude better than the ROCK42 model. The details of the methodology along with precise values and results can be found in Springer et al. [1998]. The ECOM model expresses the SRP acceleration in two different frames. The first frame is the body fixed (X, Y, Z) frame also used in the ROCK42 model. The second frame is the (B, Y, D) frame where the satellite-Sun vector is along the D axis, the Y axis lies along the solar panel rotation axis direction and the B axis completes the right-handed coordinate system. Six parameters are then estimated by fitting 5-day arcs of CODE precise ephemerides. Data over 5.5 years are used to generate time series of the six estimated parameters. These series are then analyzed and fit with trigonometric functions. The resulting SRP acceleration contribution is expressed as follows:

$$
\begin{aligned}
a_D &= D_0 + D_{C2}\cos(2\beta) + D_{C4}\cos(4\beta) \\
a_Y &= Y_0 + Y_C\cos(2\beta) \\
a_B &= B_0 + B_C\cos(2\beta) \\
a_Z &= \sin(u-u_0)\cdot\left[Z_0 + Z_{C2}\cos(2\beta) + Z_{S2}\sin(2\beta) + Z_{C4}\cos(4\beta) + Z_{S4}\sin(4\beta)\right] \\
a_X &= \sin(u-u_0)\cdot\left[X_{10} + X_{1C}\cos(2\beta) + X_{1S}\sin(2\beta)\right] \\
&\quad + \sin(3u-u_0)\cdot\left[X_{30} + X_{3C}\cos(2\beta) + X_{3S}\sin(2\beta)\right]
\end{aligned}
\tag{4.29}
$$

where

a_D , a_B = accelerations in the D and B direction

a_X , a_Y , a_Z = accelerations in the X,Y and Z direction

D_0, Y_0, B_0 = satellite-specific parameters, values for each satellite can be found in Springer et al. [1998]

Z_0 = Block-type-dependent parameter, value can be found in Springer et al. [1998]

DC2, DC4, YC, BC, ZC2, ZS2, ZC4, ZS4, X10, X1C, X1S, X30, X3C, X3S = constant parameters, values can be found in Springer et al. [1998]

u = argument of latitude of the satellite

u_0 = argument of latitude of the Sun

β = argument between the orbital plane and the spacecraft-Sun direction

MSODP implements the ECOM model by estimating a scale factor that multiplies the components of the acceleration in the (B, Y, D) frame. This factor is an indication of the accuracy of the model. If the scale factor is equal to 1 it means the ECOM is a perfect representation of SRP. Note that the values of the parameters presented in Springer et al. [1998] were obtained for Block II and Block IIA satellites. As a first approximation, we applied the ECOM model to Block IIR satellites using values previously derived for Block IIA satellites. However, for better accuracy, updated values obtained for Block IIR satellites should be used.

4.5.4 The JPL models

4.5.4.1 Early JPL model

Bar-Sever [1997] described an approach to SRP that is neither purely analytical nor purely empirical, which is known as a 'hybrid' model. This hybrid model utilizes the analytical basis from the T20 model combined with empirical data.

The JPL model is described in detail by Bar-Sever [1997] and it was designed for Block II/IIA satellites using two different modes. The first mode occurs when the satellite is in full sunlight, nominal attitude is assumed and the model is then purely empirical. The Earth-Satellite-Sun (ESS), ε, angle is used as a unique variable to describe the position of the satellite. ε is measured between the Z axis and the Earth-satellite vector. The coefficients of a truncated Fourier series are then estimated by performing a least square fit to precise ephemerides, assumed here to represent the 'true' orbit. Data from

July, 1995 to May, 1996 were here used to generate orbits for each satellite. The components of the accelerations are given in the (B, Y, D) frame:

$$\begin{cases} a_D = \eta \cdot f(m,r) \cdot (8.98 - 0.15\cos\varepsilon + 0.71\sin\varepsilon + 0.1\sin 2\varepsilon) \\ a_Y = \left(0.1 + 0.5\sin\beta + \dfrac{0.3}{\sin\beta}\right) \cdot \cos\varepsilon \\ a_B = \eta \cdot f(m,r) \cdot (-0.03\sin\varepsilon + 0.73\cos\varepsilon - 0.74\sin 2\varepsilon) \end{cases} \tag{4.30}$$

The second mode accounts for eclipsing satellites. In this mode, the model is purely analytical and is a modification of the T20 model described in Section 4.5.2. One of the main assumptions of the T20 model is that the antenna always points toward the center of the Earth, but this nominal attitude does not always apply. The attitude problems of Block II satellites are described in Bar-Sever [1996a, 1996b]. Figure 4.7 shows the main non-nominal attitude cases:

- at the point of the orbit closest to the Sun, “noon”
- at the point of the orbit farthest to the Sun, “midnight”
- up to 45 min after shadow crossing

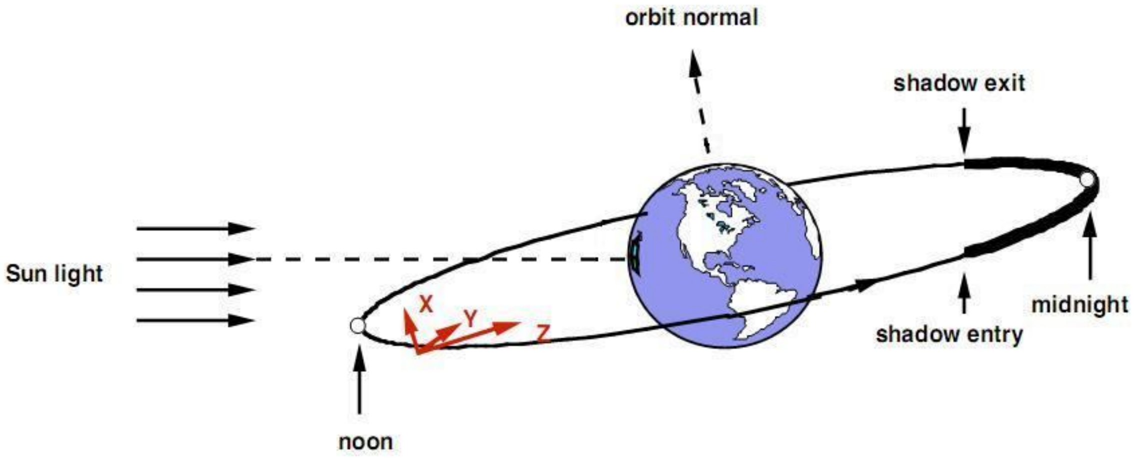

Figure 4.7. Different points of non-nominal attitude for GPS Block II [Bar-Sever, 1997]

To account for non-nominal attitude, the force computed by the T20 model is 'split' into a force applied on the main body and a force applied on the solar panel. Details about this decomposition are given in Bar-Sever [1997]. The main body is then assumed to be symmetric and the SRP component on the solar panels is further decomposed along the spacecraft-Sun direction and along the normal to the solar panels. During full eclipse, SRP is simply set to 0.

This model is also in use in MSODP. As for the ECOM model, we can estimate a scale factor that multiplies the components of the acceleration in the (B, Y, D) frame. An estimated value of 1 would mean that the model perfectly model SRP. As an approximation, we applied this model to Block IIR satellites as well. For improved accuracy, the improved model described below should be applied to Block IIR satellites.

4.5.4.2 JPL model improvements

In a most recent contribution, Bar-Sever provides a new version of the model described above applied to GPS Block IIR along with an improved version of the model for Block II/IIA. Details can be found in Bar-Sever and Kuang [2006]. In this new model, the parameterization has been improved. In addition, instead of using only a few months of data, this newer model now uses four years and a half. It is also worth noting that the precise ephemerides also improved significantly overtime and went from a 3D error of 15 cm in Root Mean Square (RMS) to below 5 cm. As far as the Block IIR satellites are concerned, a similar parameterization was used based on the T30 model describe in Section 4.5.2. However, because Block IIR satellites have a simpler attitude behavior [Kouba, 2009], the empirical method is still used during eclipse seasons. In addition, when the satellite is in the umbra, SRP is assumed to be 0. During the penumbra, SRP is scaled by the visible fraction of the Sun. Note that improvements could be made here by taking into account the atmospheric refraction. Indeed, the gradient of temperature changes the apparent shape of the Sun's disk while setting or rising. The Sun then appears flattened [Vokrouhlický et al., 1993]. This effect would, of course, increase the accuracy of SRP modeling during shadow crossing.

Note that the newer version of this model has not yet been implemented in MSODP. All the experiments conducted in this study use the early JPL model and thus do not represent the improvements in performance of the actual JPL model.

4.5.5 The UCL model

4.5.5.1 Description

The body-fixed frame is defined by Ziebart [2004a] is the same as the one described in the ROCK42 model. Its origin is at the center of mass of spacecraft. The Z-axis is parallel to the antenna boresight. The y-axis lies along the solar panel and the X-axis completes the right handed coordinate system.

In the UCL model implemented here, two main assumptions were made on the attitude of the satellite. First, the solar panels are constrained to be perpendicular to a line joining the spacecraft and the Sun. In addition, the antenna boresight is directed toward the geocenter. As a consequence, the Sun remains in the same hemisphere above the Y-Z plane and its position can be defined by a unique angle, the Earth-Satellite-Sun (ESS) angle. The ESS angle is measured between the Z axis and the Earth-satellite vector. These assumptions are not exactly true. Several approaches exist concerning the attitude of Block IIR satellites as seen in Fliegel and Gallini [1996] and Marquis and Krier [2000]. These approximations are justified in Ziebart et al. [2003] by examining the accuracy of the orbit prediction.

The spacecraft is then modeled in a very detailed fashion, using different elements: cylinders, circles, rings, paraboloids and cones. The photon flux is represented by a pixel array that will be projected onto the spacecraft model in order to calculate the acceleration (Figure 4.8). For each specific ray, its first intersection with the spacecraft is then computed. Based on Equation (2.5), the normal and shear components of the resulting acceleration on a flat surface are shown in Ziebart [2004a] to be:

$$\begin{cases} a_{f,N} = -\dfrac{A \cdot E}{c} \cdot \cos\theta \cdot \left\{ (1 + \nu \cdot \mu) \cdot \cos\theta + \dfrac{2}{3} \cdot \nu \cdot (1 - \mu) \right\} \\ a_{f,S} = \dfrac{A \cdot E}{c} \cdot \cos\theta \cdot (1 - \nu \cdot \mu) \cdot \sin\theta \end{cases} \tag{4.31}$$

where

A	is the cross-sectional area exposed to sunlight (m^2)
E	is the Total Solar Irradiance
c	is the speed of light (m/s)
θ	is the angle of incidence of the ray on the surface
ν	is the reflectivity coefficient
μ	is the specularity coefficient

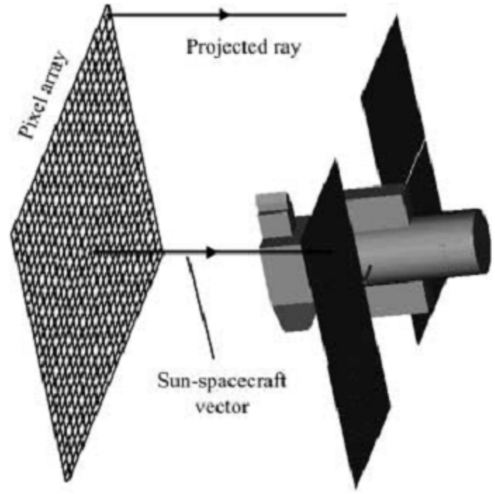

Figure 4.8. The pixel array method [Ziebart and Dare, 2001]

Note that Equations (4.31) are similar to the ones derived in the ROCK42 model. Equations (4.31) account for specularly reflected rays as well as diffusely reflected rays. It is worth noting that the UCL model takes into account the force created by secondary intersections, although only the specular part is computed. Secondary intersections happen when the incident ray get reflected onto another part of the spacecraft. The specular component is then added to the acceleration and the diffuse component is neglected. This process is performed for every ray that intersects with one component of the model. The position of the pixel array in the body fixed frame is a function of the ESS angle. As this angle varies over time, the pixel array rotates around the spacecraft and the resulting force can be computed. To avoid intensive computation, the data are finally being fit using a Fourier series with the ESS angle as the independent variable. Note that the UCL approach also provides a way to account for non-nominal attitudes using small angle perturbations.

4.5.5.2 Implementation

For the purpose of the study, the UCL model was implemented in MSODP. Although the UCL modeling techniques could be used for other satellites, the version of the UCL model used here was developed for Block IIR satellites. The code, along with the set of Fourier coefficients, was provided by UCL in 2004, Ziebart [2004b]. Improvements of the code were implemented in 2006. More precisely, the model would not only account for SRP but would also include other non-gravitational forces such as the antenna thrust (see Section 4.4.6). Note that the model is still under active development.

The code was modified to be integrated in MSODP. In addition, changes in MSODP were made to include the model. The first step was to implement the model in 'propagation' mode where the SRP contribution to the acceleration is directly calculated using the UCL model. To make sure the acceleration returned by MSODP for a given satellite was correct, MSODP outputs were compared with test cases provided by Ziebart [2004b].

To improve orbit accuracy, further modifications of MSODP were necessary. We introduced a scale factor η that multiplies the three components of the contribution to the acceleration as follows:

$$\vec{a}_{SRP}^{New} = \eta \cdot (\vec{a}_X + \vec{a}_Y + \vec{a}_Z) \tag{4.32}$$

where η allows to compensate for errors in the model. If the model would be perfect, then η would equal to 1. Estimation of η requires the calculation of the partial derivatives of the SRP acceleration with respect to the position and with respect to state. Details can be found in Appendix B.

To validate the implementation of the scale factor estimation, a few tests were performed. The idea here was to introduce a known error and see if MSODP would be able to detect it. More precisely, an arbitrary fixed value of η was used during a 1-day prediction. The resulting orbit was then fit using the estimated scale factor. The scale factor was estimated 48 times per day. The time series for η obtained after estimation was plotted. In the first test, the degraded orbit was generated with a fixed value of η equal to 1.2. Figure 4.9 shows the results of the scale factor estimation after the fit. As we can see, η stays really close to 1.2. This shows that MSODP is able to compensate rather well for the intentional error that was introduced.

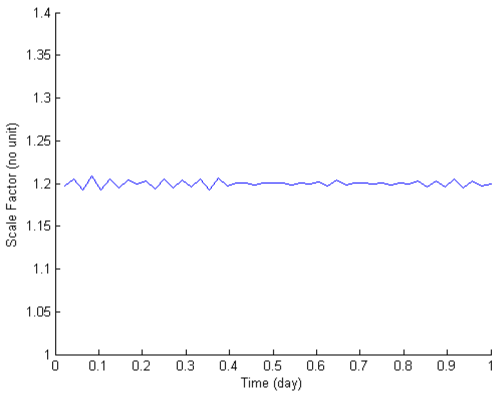

Figure 4.9. Estimation error recovery

A second orbit was generated over 1 day with a value of η equals to 1.2 during the first half of the day and another value of η of 1.8 during the second half of the day. The resulting time series for η after a fit to this orbit is shown in Figure 4.10. The value of the estimated η starts very close to 1.2 to make a sharp jump to 1.8 after half a day. As expected, MSODP seems to sens the changing errors used to generate the orbit. These two experiments assisted with validating the implementation of the scale factor for the UCL model.

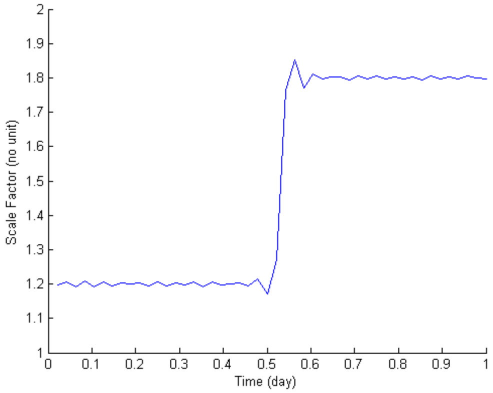

Figure 4.10. Estimation error recovery with variable error

4.6 ANALYTICAL VS. EMPIRICAL

Two main approaches can be distinguished when modeling SRP. On one hand, analytical methods approximate the satellite as accurately as possible along with the force induced by the incident sunlight. Thus, these models have an inherent physical meaning. This category includes the early Cannonball model, the ROCK42 model and the UCL model. Analytical models can provide a good approximation of SRP without the use of any on-orbit data. This is particularly helpful for new satellites like the future GPS Block III or the new GNSS Galileo. In addition, since analytical models attempt to represent the physical phenomena, they might be expected to give good predictions. However, a few major disadvantages remain. Analytical models require precise data about the satellite structure: precise shape, geometry and thermal properties like reflectivity coefficients. As a consequence, only recent models can account with precision for complex spacecraft. In addition, analytical methods cannot account for all the other error sources. Assumptions made to create the model will induce errors as well as change of the satellite geometry and thermal property over time. For instance, the y-bias force is believed to come from a misalignment of the solar panels.

On the other hand, empirical models such as the ECOM model and the recent JPL model require no modeling of the spacecraft. They are based on numerous on-orbit observations allowing precise modeling of the SRP behavior. The main advantage of empirical parameterization consists in taking into account all the effects due to SRP. Indeed, because they are using real data, empirical models will be able to compensate accurately for changes in geometry or in thermal properties. In turn, fine tuning or modifications of the models are possible. Nevertheless, to be efficient, empirical approach require several years of on-orbit data. Obviously, this is not the case for new satellites. Besides, empirical models do not have a physical meaning. In other words, each parameterization is satellite specific.

Some models do not lie strictly in one of the two categories described above. As seen previously, the early JPL model was a hybrid model switching from an empirical model to an analytical model. Note that analytical models are not always perfect and the errors associated with them can be accommodated by estimation of an empirical scale factor.

4.7 SHORT-TERM EFFECTS OF SRP ON ORBITAL ELEMENTS

In this section, we look at the effects of SRP on orbital elements of GPS satellites. Experiments over a few days were conducted to show how SRP affects the different orbital elements.

4.7.1 Methodology

As an example, we chose PRN 31 (SVN 52), a Block IIR-M satellite launched at the end of 2006 and thus one of the most recent satellites in the constellation. The experiments were performed starting February 1, 2008, for 1 or 3 days. Note that during this period, the satellite is not eclipsing and does not undergo any maneuver. To show the effect of SRP on orbital elements, two consecutive orbits were generated. Both were obtained with a fit to the IGS precise ephemerides. However, in the first case, the simple Cannonball SRP model was used whereas in the second model, SRP modeling was turned off. The orbital elements were then calculated from the generated orbit in both cases. The orbital elements obtained when SRP was turned off were then subtracted to the one with SRP turned on. A summary of the set-up is shown in Figure 4.11.

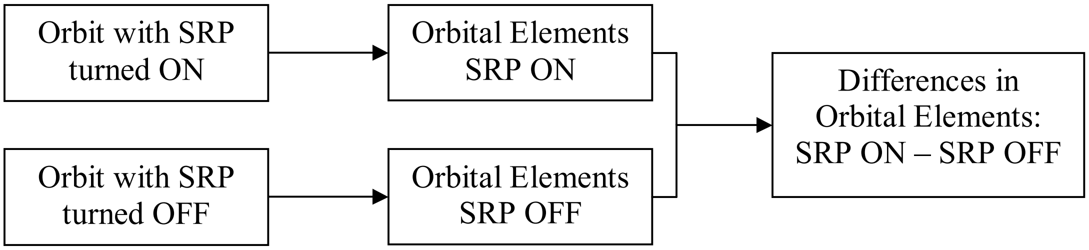

Figure 4.11. Summary of the experiment

4.7.2 Results

Figure 4.12 shows the effect of SRP on the semimajor axis over 1 day. We can see that the amplitude is about 16 meters. This is a small effect compared to the J2 effect as we saw in Section 4.3.1. Over 3 days, Figure 4.13, we observe an apparent decay of about 3.2 m/day caused by SRP.

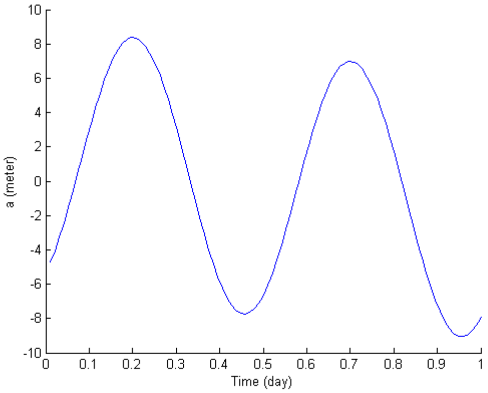

Figure 4.12. 1 day, semimajor axis

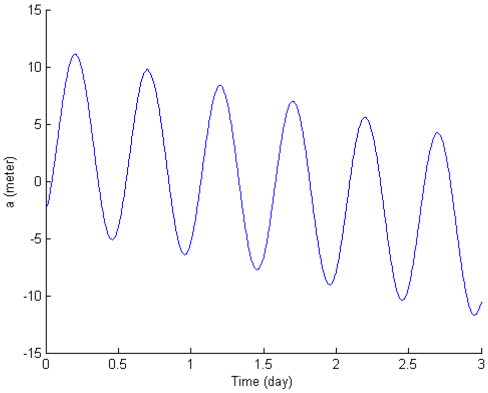

Figure 4.13. 3 days, semimajor axis

The eccentricity, Figure 4.14, presents a steady growth over 1 day with an amplitude of about 1.5×10^{-6}. Using the average value of the semimajor axis, this would represent about 40 km difference in the position of the perigee or apogee with respect to the geocenter.

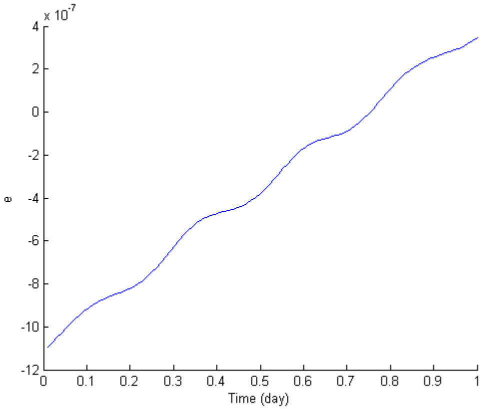

Figure 4.14. 1 day, eccentricity

The argument of perigee, Figure 4.15 shows a steady grows with an amplitude of about 20×10^{-3} degrees which is significant as far as the position of the perigee is concerned.

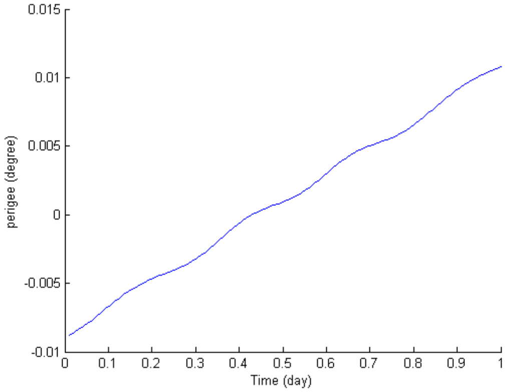

Figure 4.15. Argument of perigee

Both the inclination and the right ascension of the ascending node show very small variations. The amplitude of the difference in inclination in Figure 4.16 is about 12×10^{-6} degrees. The right ascension of the ascending node presents an amplitude of about 1.6×10^{-5} in Figure 4.17.

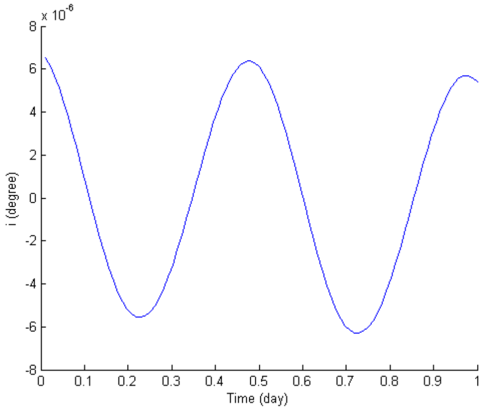

Figure 4.16. Inclination

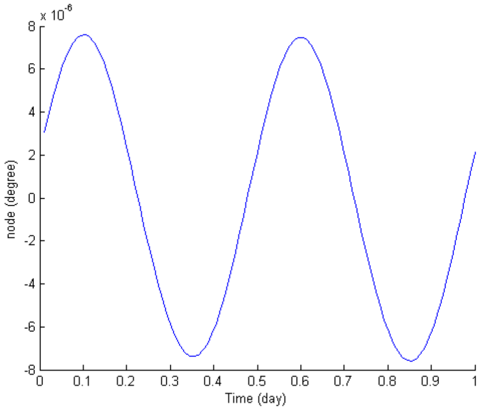

Figure 4.17. Right ascension of the ascending node

4.7.3 Conclusion

These short experiments presented some effects of SRP on the orbital elements. In summary, we observed that SRP produces significant variations on the eccentricity and on the argument of perigee whereas its effect on the semimajor axis is only small. Lastly, the variations in inclination and right ascension of the ascending node are very small. These results are consistent with the study in [Beutler, 2005] although the methods used present major differences.

Chapter 5

Methodology

5.1 USING IGS EPHEMERIDES IN MSODP

To study the GPS orbits, the IGS final ephemerides are used as our observations in MSODP's batch estimator. Their accuracy is believed to be fewer than 5 cm [IGS, 2008c]. As described in Section 1.3.2, these ephemerides are a combination of solutions generated by the individual Analysis Centers. A central issue is to know to what extent each individual solution influences the estimated orbit computed with MSODP.

5.2 SETUP

One way to examine the impact of individual centers' solution on the estimated orbit is to compare characteristics of the resulting orbit using ephemerides from different Analysis Centers. Similar experiments were conducted using the IGS combined final ephemerides, the European Space Agency (ESA) final ephemerides and the JPL final ephemerides. The ESA and JPL Analysis Centers were chosen due to their differences in processing strategy, in particular with regards to the SRP model used (See Appendix A). A Block IIR satellite, PRN13, was chosen here so the UCL model could be used. The different ephemerides were fit over one day arcs over the year 2006. Initial position and velocity were estimated once a day. The y-bias parameter was estimated twice per day and the Cannonball SRP parameter was estimated four times per day.

5.3 RESULTS

To observe the influence of the ephemerides used, we examined the estimated y-bias time series as well as the evolution of the RMS of position differences of the daily fits. Figure 5.1 shows the results using the IGS ephemerides as our observations. Results using the JPL ephemerides are shown in Figure 5.2. Lastly, Figure 5.3 shows the cases using the ESA ephemerides.

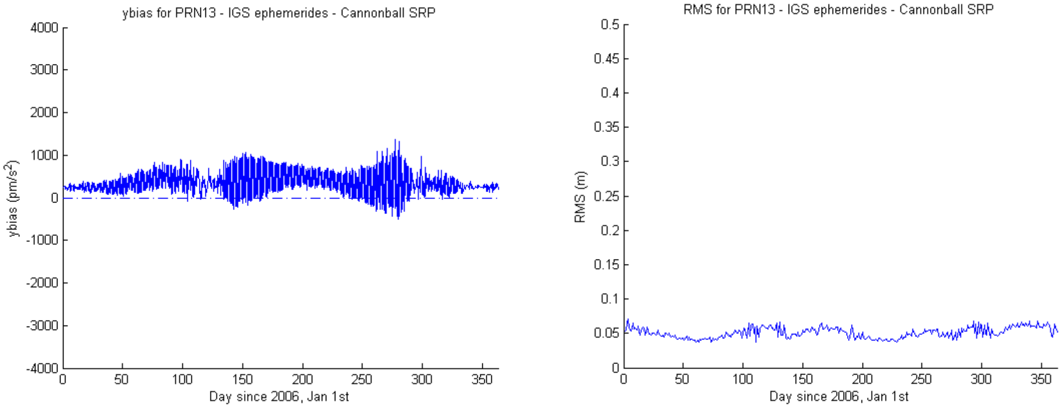

Figure 5.1. y-bias and RMS evolution - IGS ephemerides - Cannonball - 2006 - PRN13

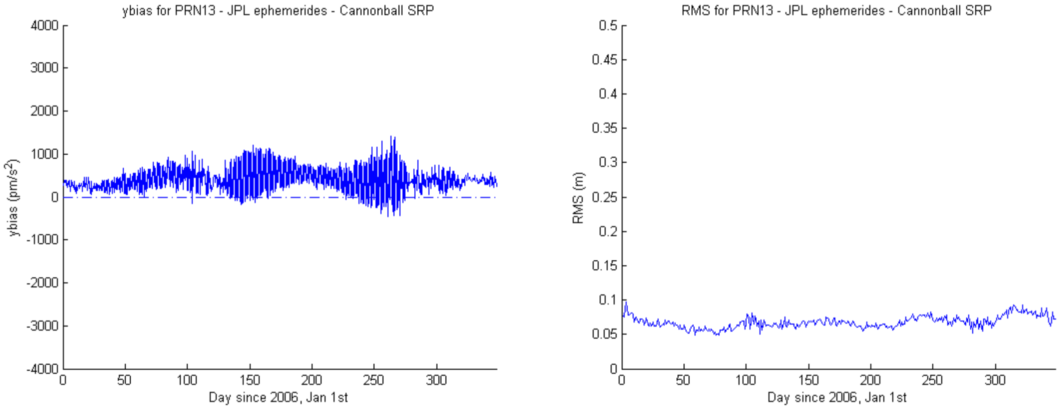

Figure 5.2. y-bias and RMS evolution - JPL ephemerides - Cannonball - 2006 - PRN13

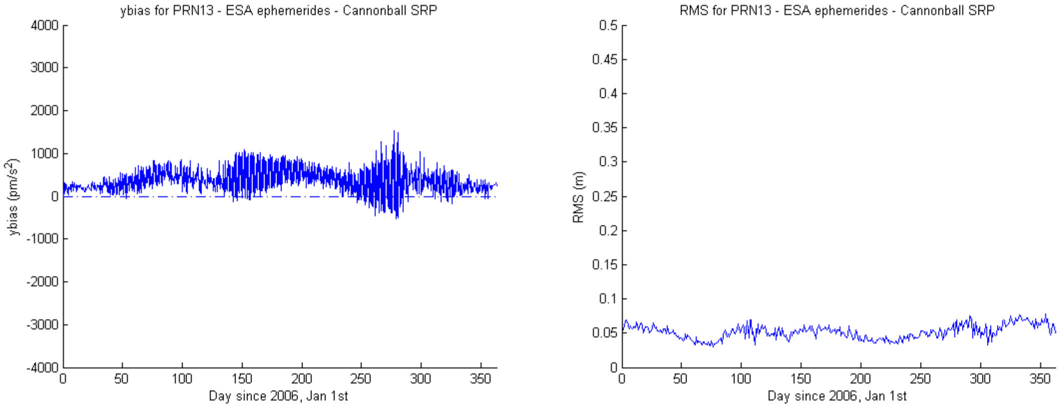

Figure 5.3. y-bias and RMS evolution - ESA ephemerides - Cannonball - 2006 - PRN13

The y-bias evolution, as well as the RMS time series, appears to be similar in the three cases. Y-bias differences were computed. Figure 5.4 shows the difference in the y-bias parameter between the IGS case and the JPL case. Figure 5.5 shows the difference between the IGS case and the ESA case. These differences are small compare to the amplitude of the y-bias.

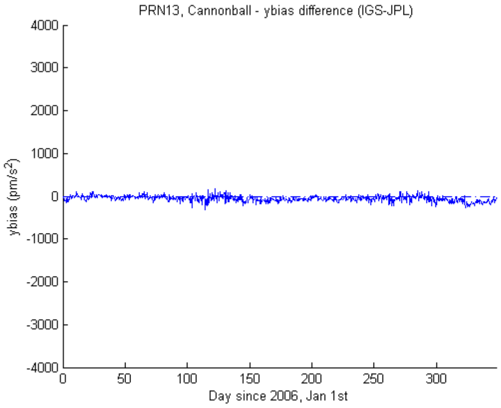

Figure 5.4. y-bias differences between IGS and JPL ephemerides

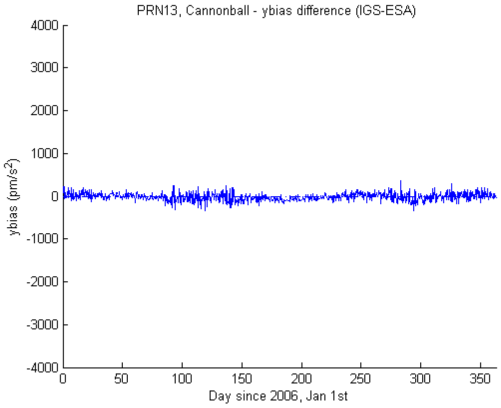

Figure 5.5. y-bias differences between IGS and ESA ephemerides

To make sure the SRP model used does not influence these observations, similar experiments were performed using the ECOM model, the UCL model, the ROCK42 model and the JPL model. Results are presented in Figure 5.6 through Figure 5.11. The y-bias evolution does show different characteristics depending on the SRP model used. However, using the same SRP model, the y-bias evolution looks similar whether we use the IGS combined ephemerides, the JPL or the ESA ephemerides.

As in the previous case, differences were computed and are shown in Figure 5.12 and Figure 5.13. These differences are small compared to the amplitude of the y-bias parameter. It is interesting to note that the small differences between the IGS and the ESA cases are the same no matter what model used. This is also true for the differences between the IGS and the JPL cases. This simply shows that each kind of ephemerides introduces its own variations.

Additional cases were computed using similar daily orbit fits in year 2008 instead of 2006. The y-bias and RMS evolution for these cases can be found in Figure 5.14 through Figure 5.19. Using the same SRP model, the y-bias parameter and the RMS are very similar no matter what set of ephemerides is used.

The above experiments show that the ephemerides used, IGS, JPL or ESA ephemerides, does not influence significantly the observations made about the estimated orbit. In other words, the impact of the individual Analysis Center is small enough to allow us to use the IGS final combined ephemerides for this study.

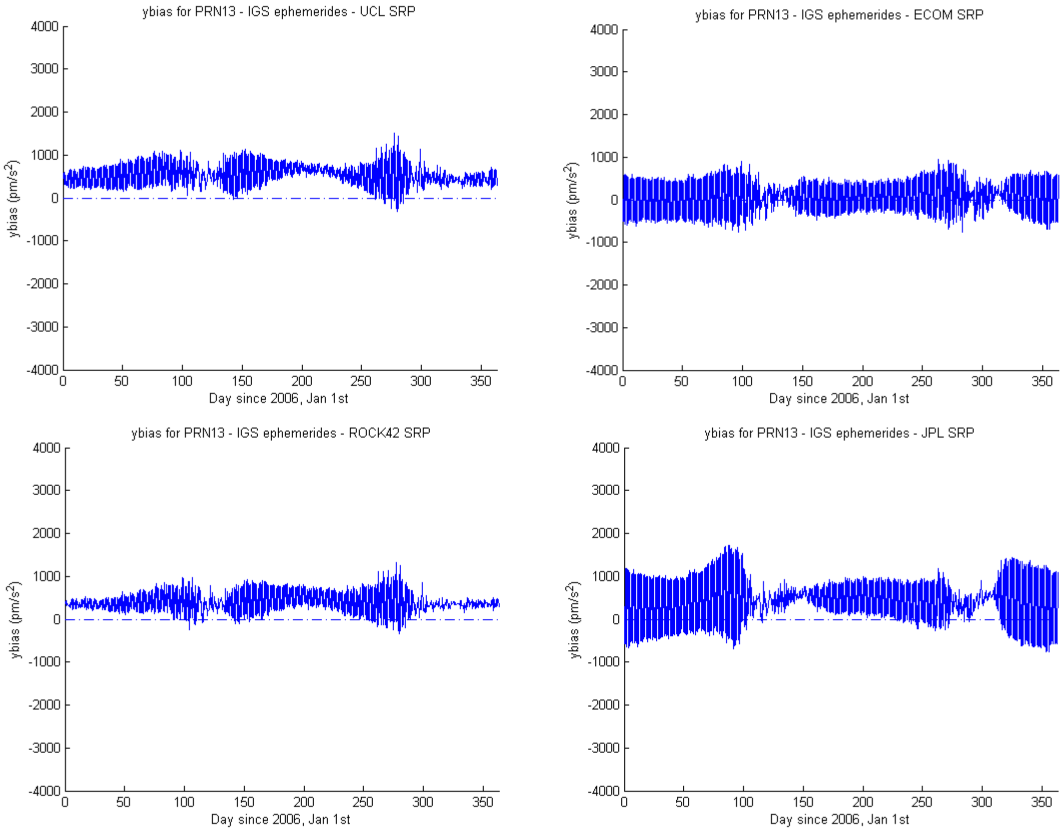

ybias for PRN13 - IGS ephemerides - UCL SRP

ybias for PRN13 - IGS ephemerides - ECOM SRP

ybias for PRN13 - IGS ephemerides - ROCK42 SRP

ybias for PRN13 - IGS ephemerides - JPL SRP

Figure 5.6. y-bias evolution - IGS ephemerides - 2006 - PRN13

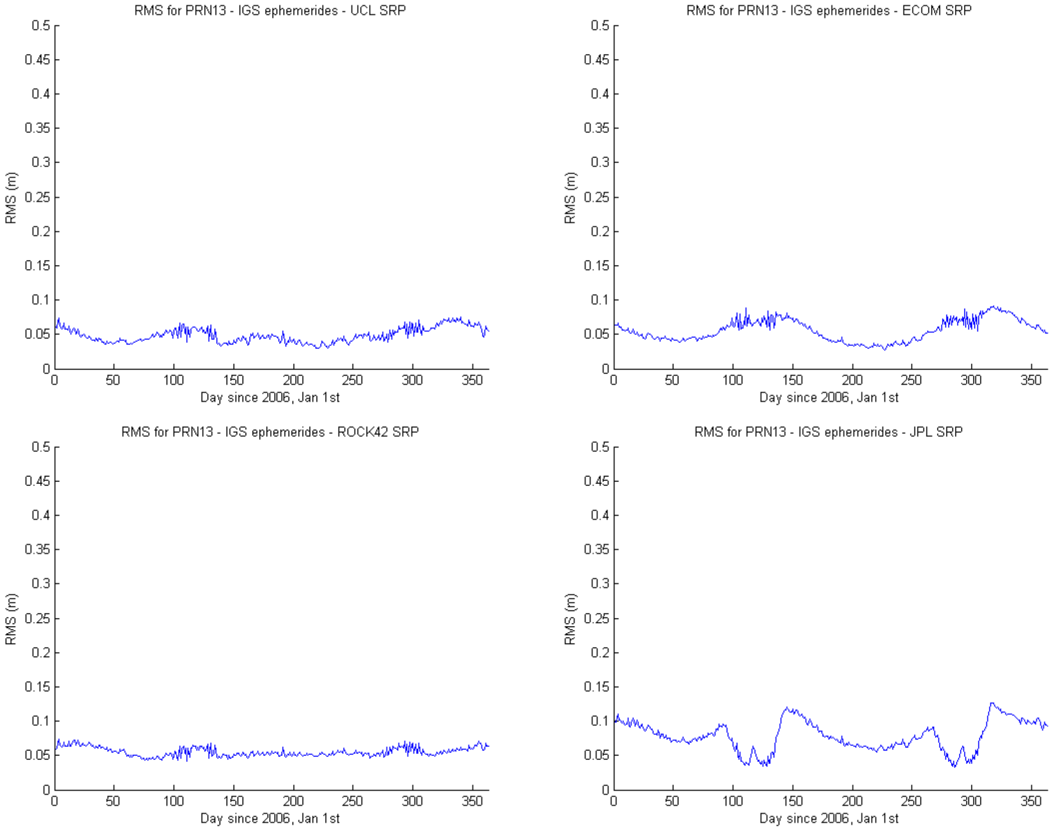

Figure 5.7. RMS evolution - IGS ephemerides - 2006 - PRN13

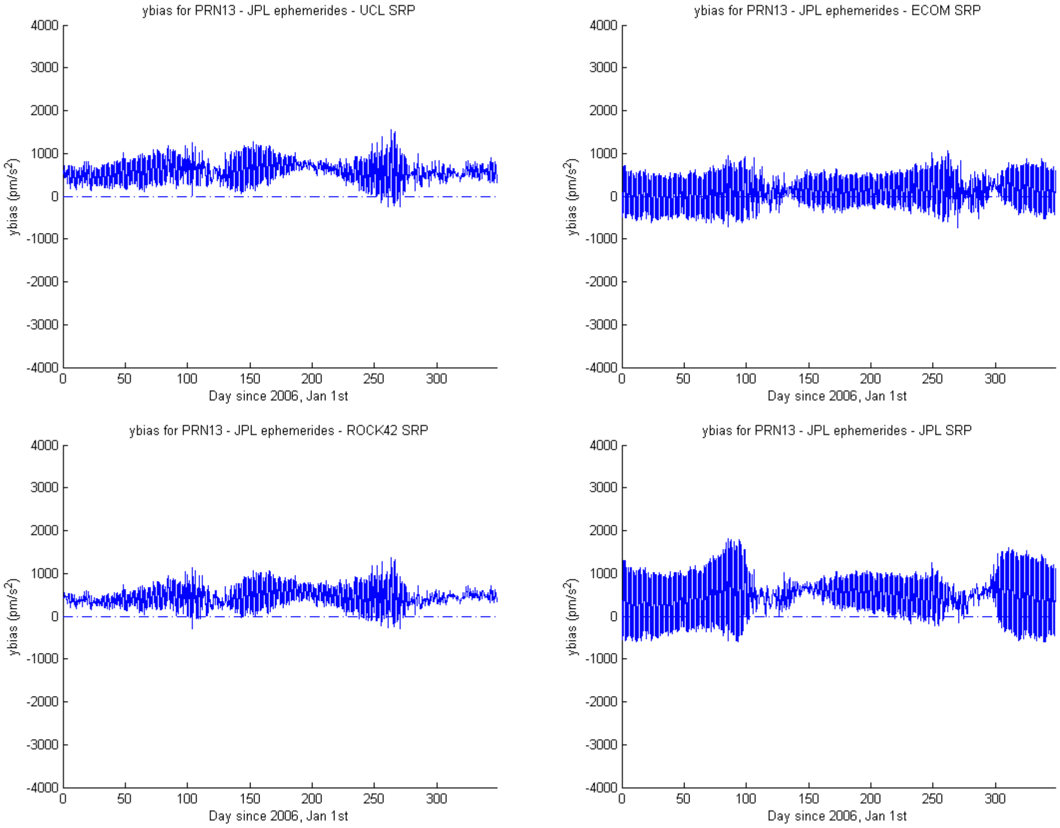

Figure 5.8. y-bias evolution - JPL ephemerides - 2006 - PRN13

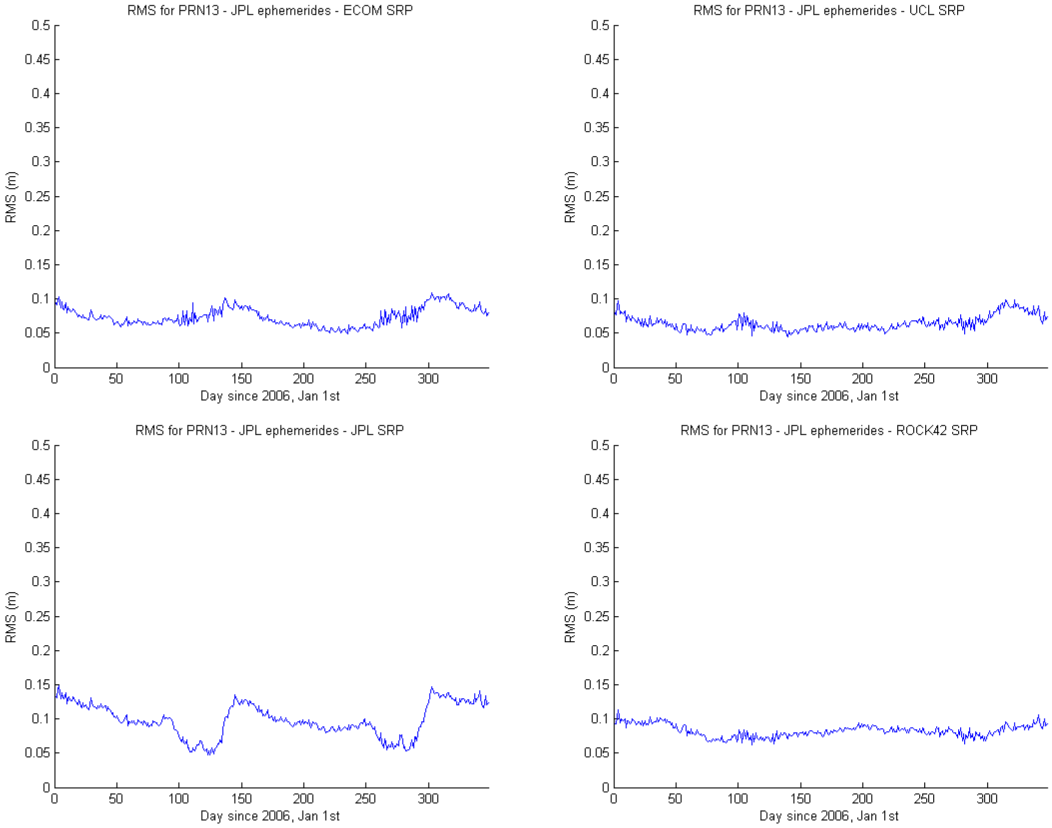

Figure 5.9. RMS evolution - JPL ephemerides - 2006 - PRN13

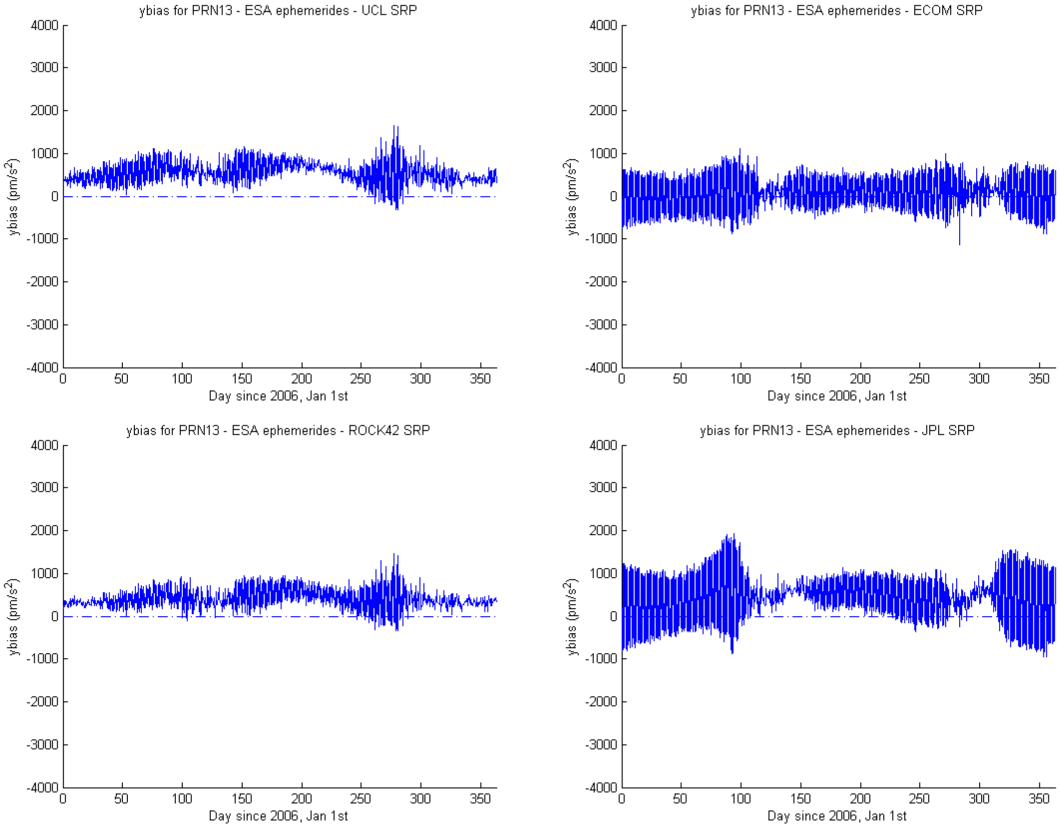
ybias for PRN13 - ESA ephemerides - UCL SRP

ybias for PRN13 - ESA ephemerides - ECOM SRP

ybias for PRN13 - ESA ephemerides - ROCK42 SRP

ybias for PRN13 - ESA ephemerides - JPL SRP

Figure 5.10. y-bias evolution - ESA ephemerides - 2006 - PRN13

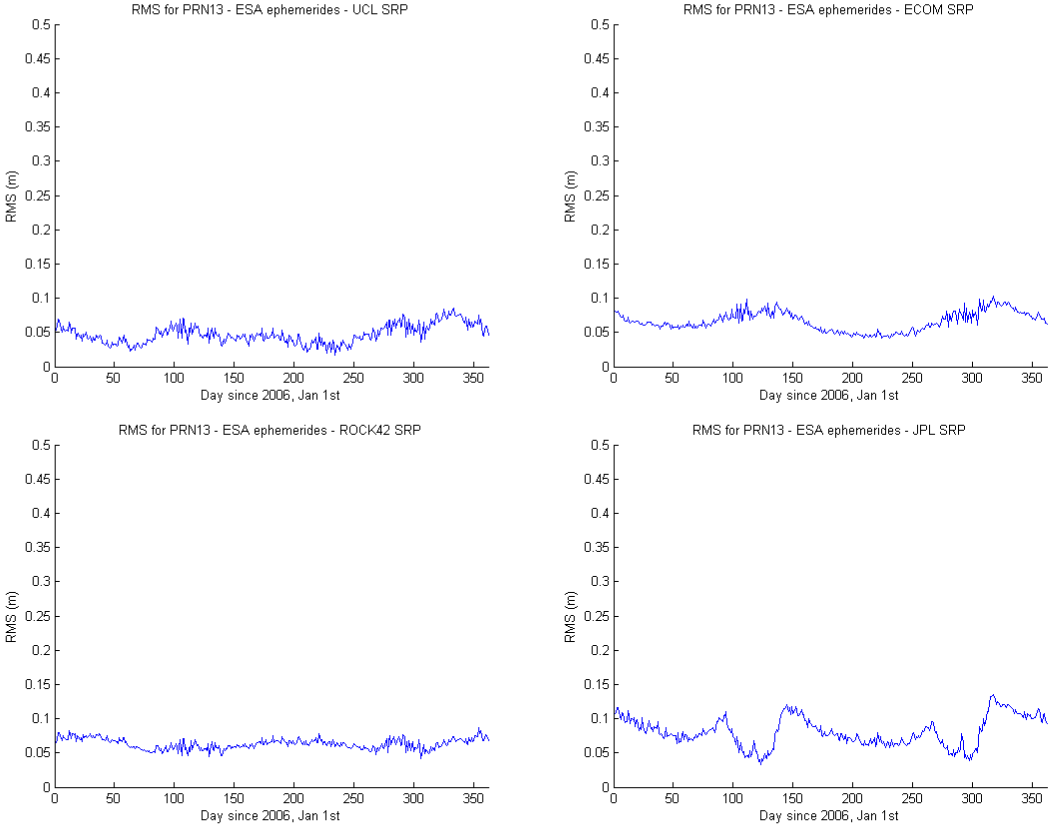

Figure 5.11. RMS evolution - ESA ephemerides - 2006 - PRN13

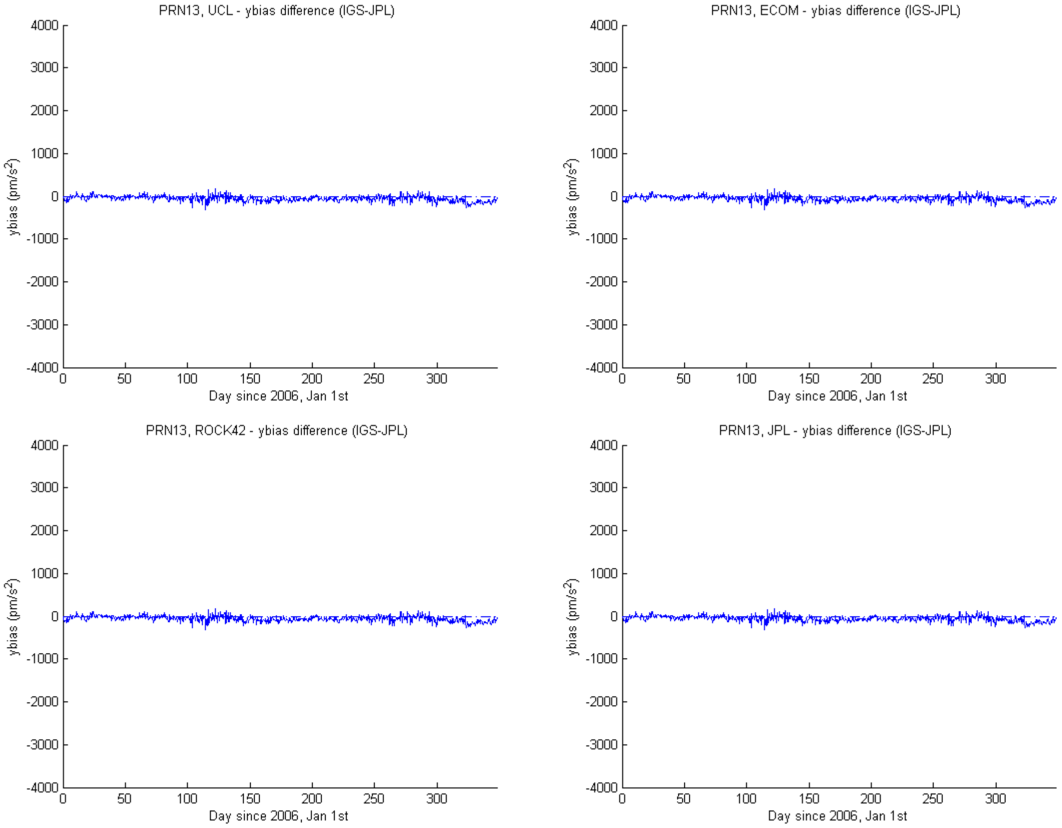

Figure 5.12. y-bias differences between IGS and JPL ephemerides

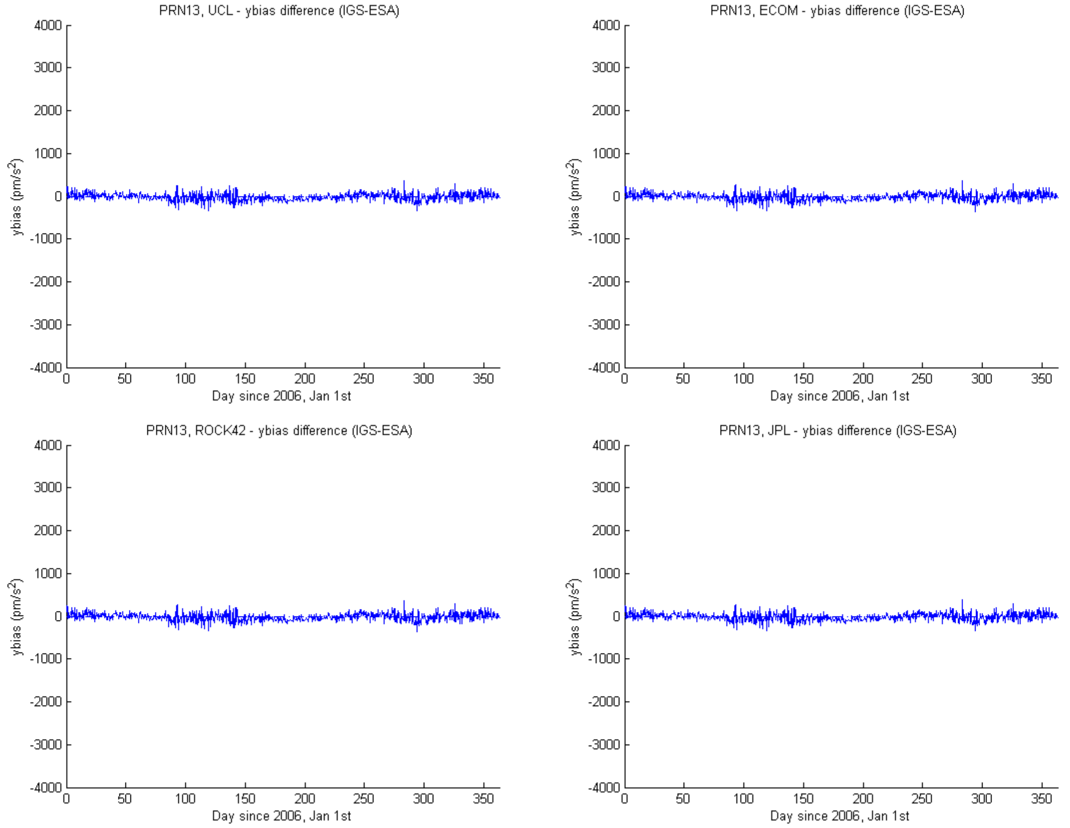

Figure 5.13. y-bias differences between IGS and ESA ephemerides

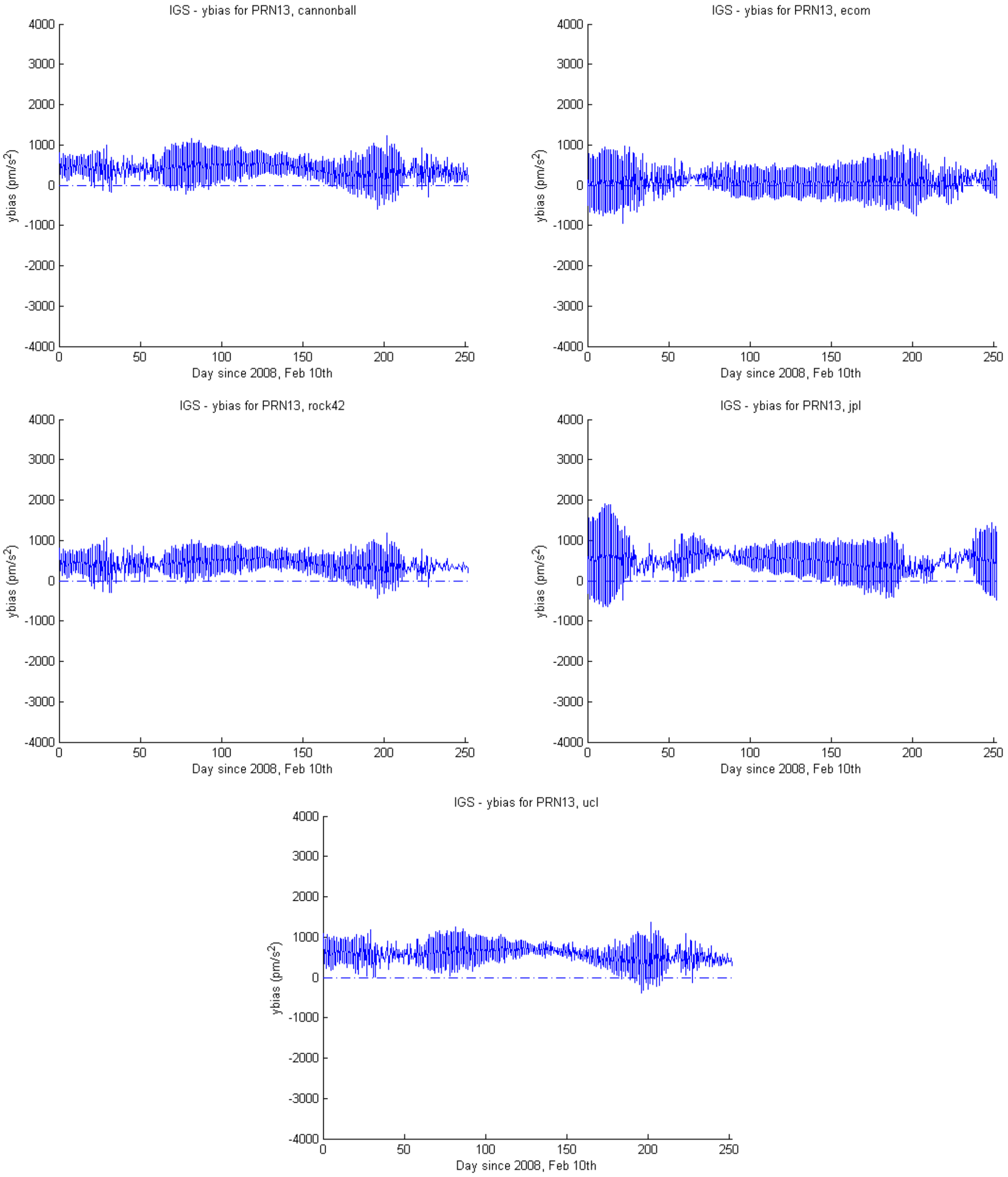

Figure 5.14. y-bias evolution - IGS ephemerides - 2008 - PRN13

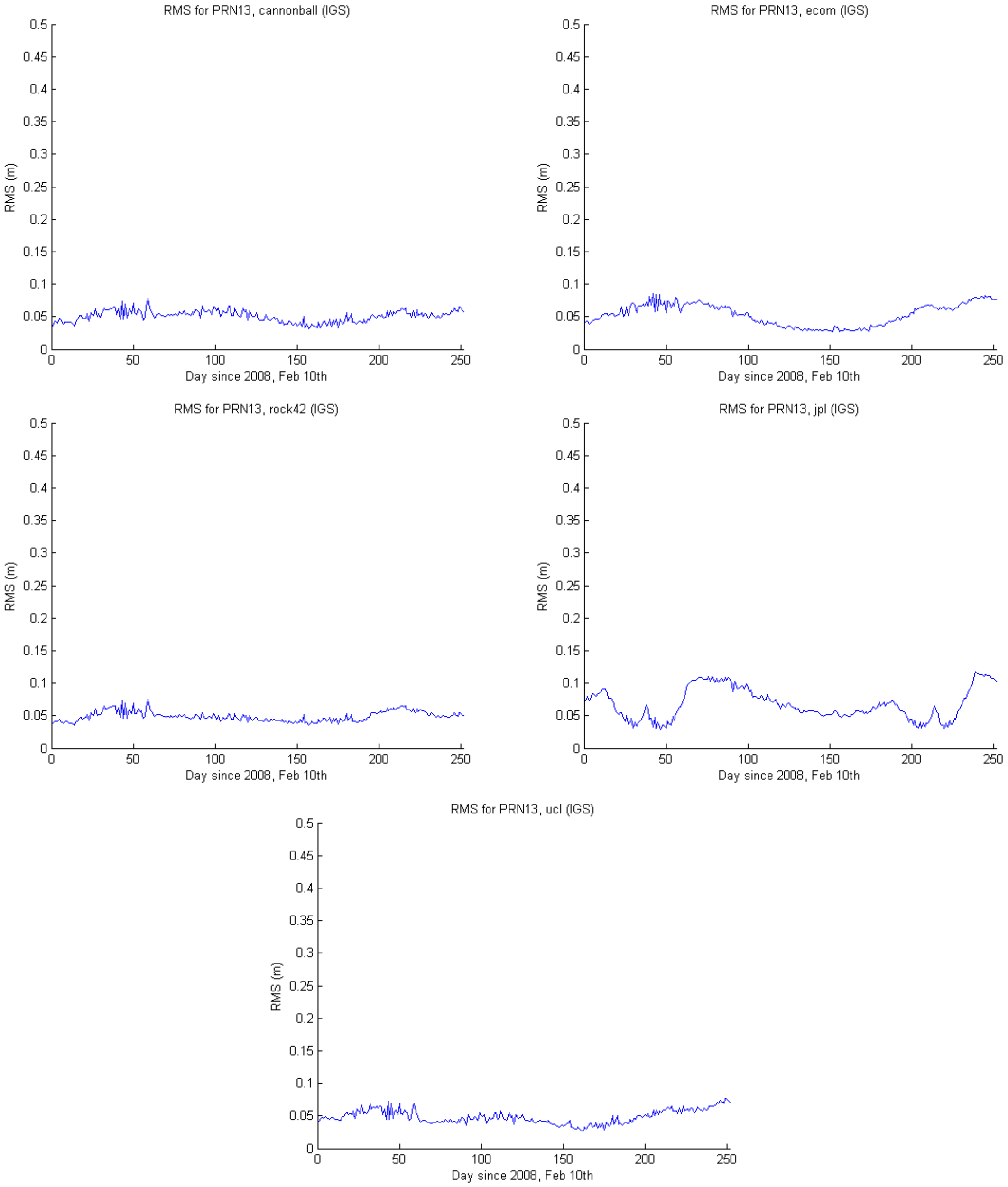

Figure 5.15. RMS evolution - IGS ephemerides - 2008 - PRN13

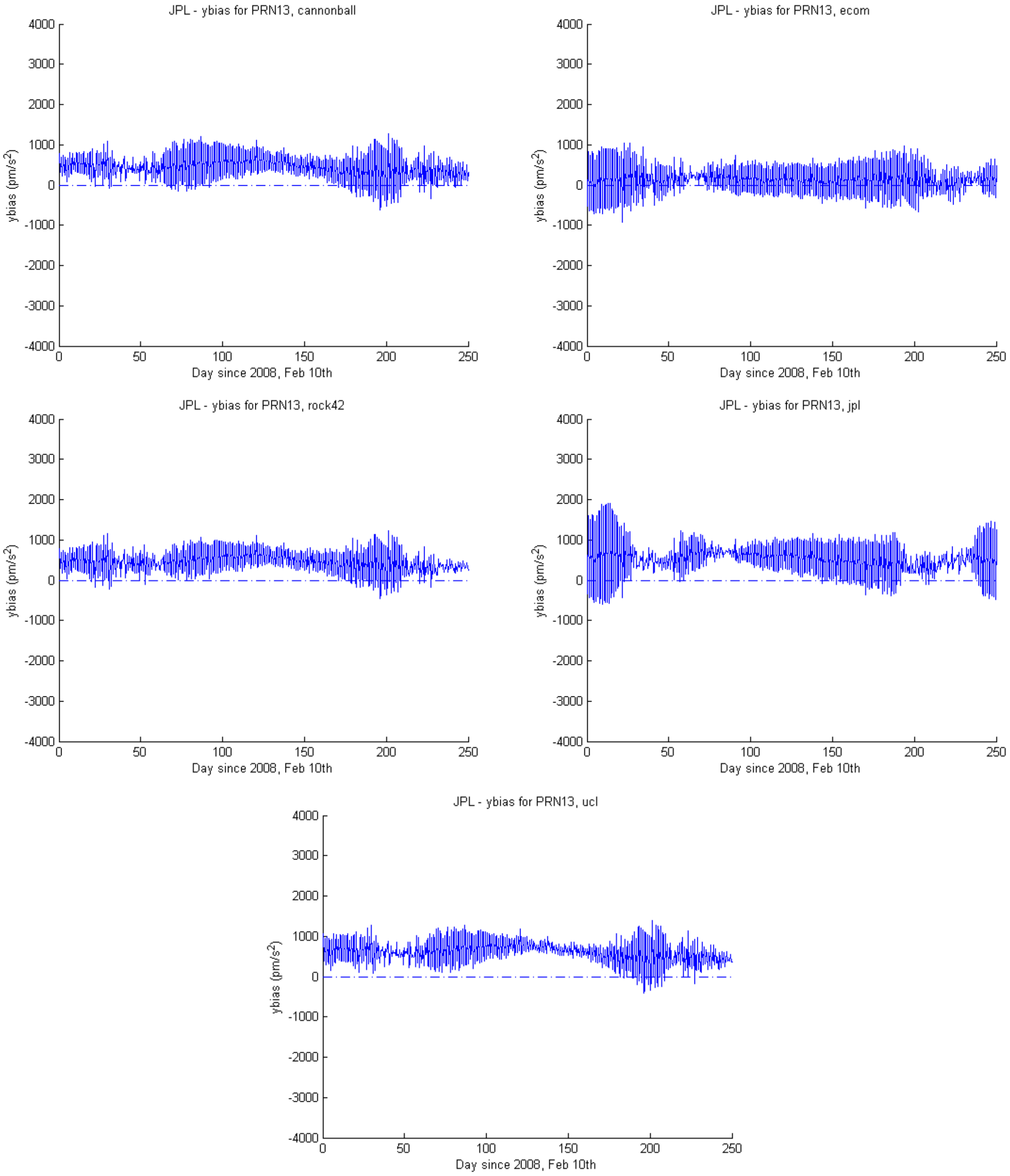

Figure 5.16. y-bias evolution - JPL ephemerides - 2008 - PRN13

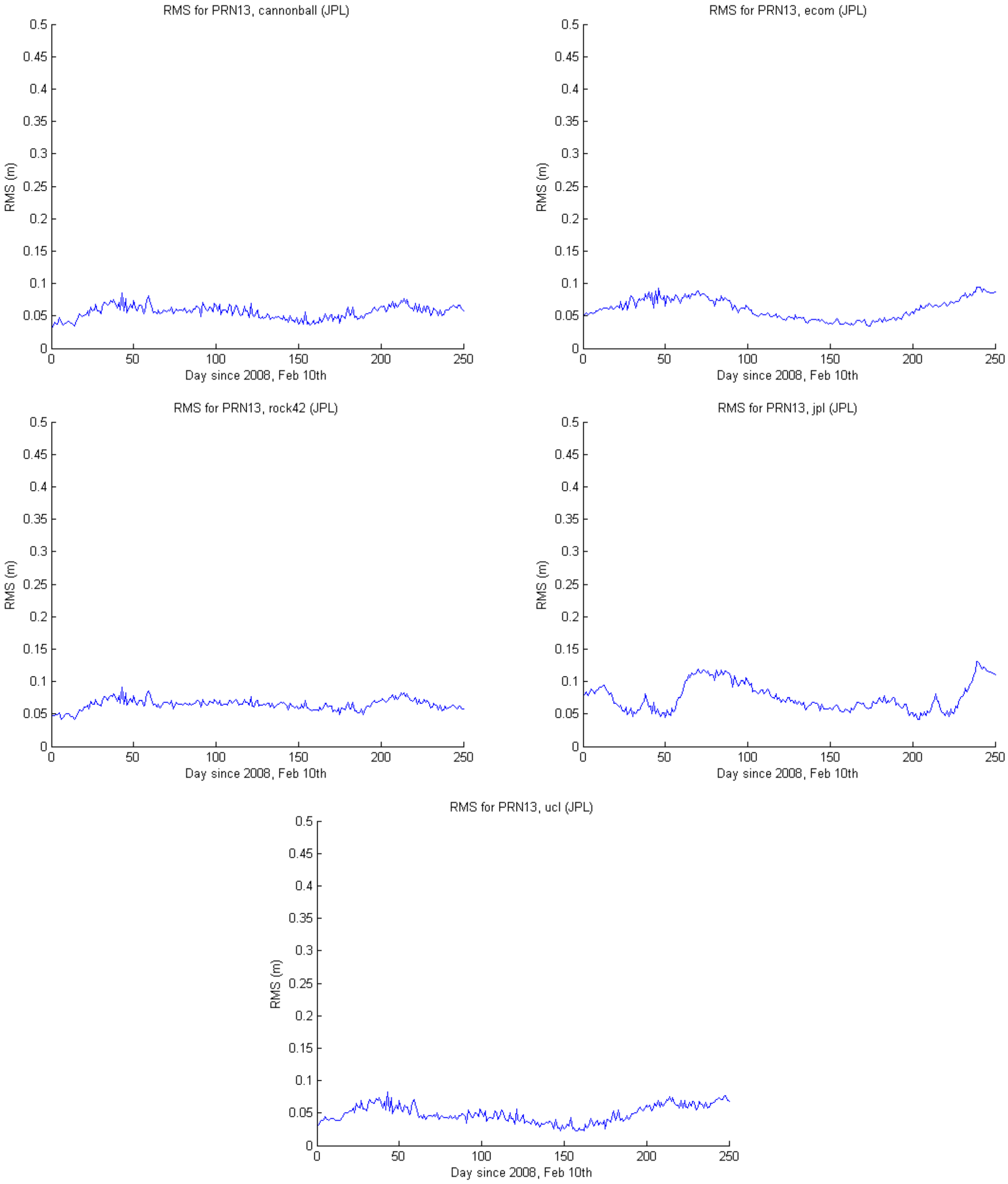

Figure 5.17. RMS evolution - JPL ephemerides - 2008 - PRN13

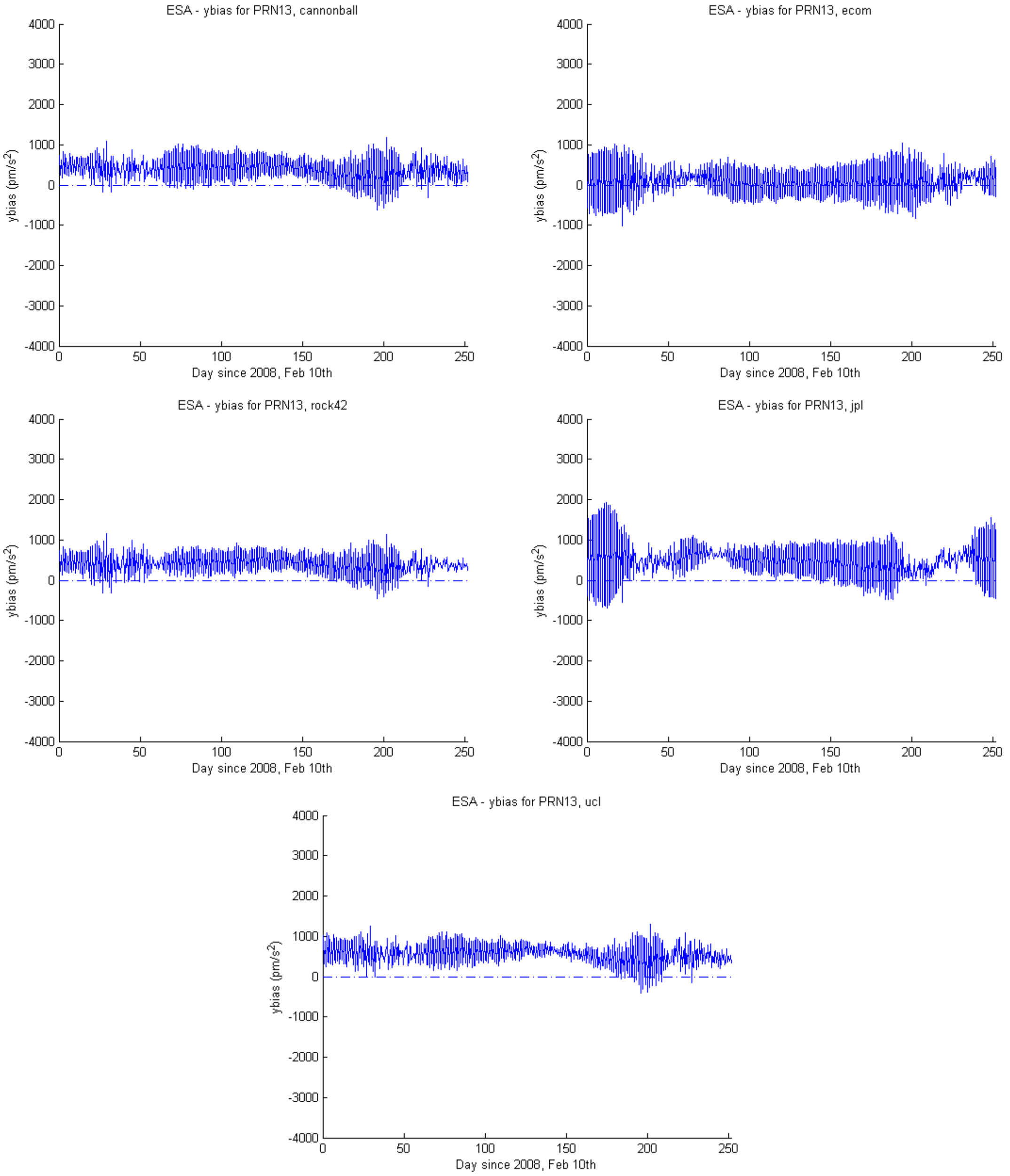

Figure 5.18. y-bias evolution - ESA ephemerides - 2008 - PRN13

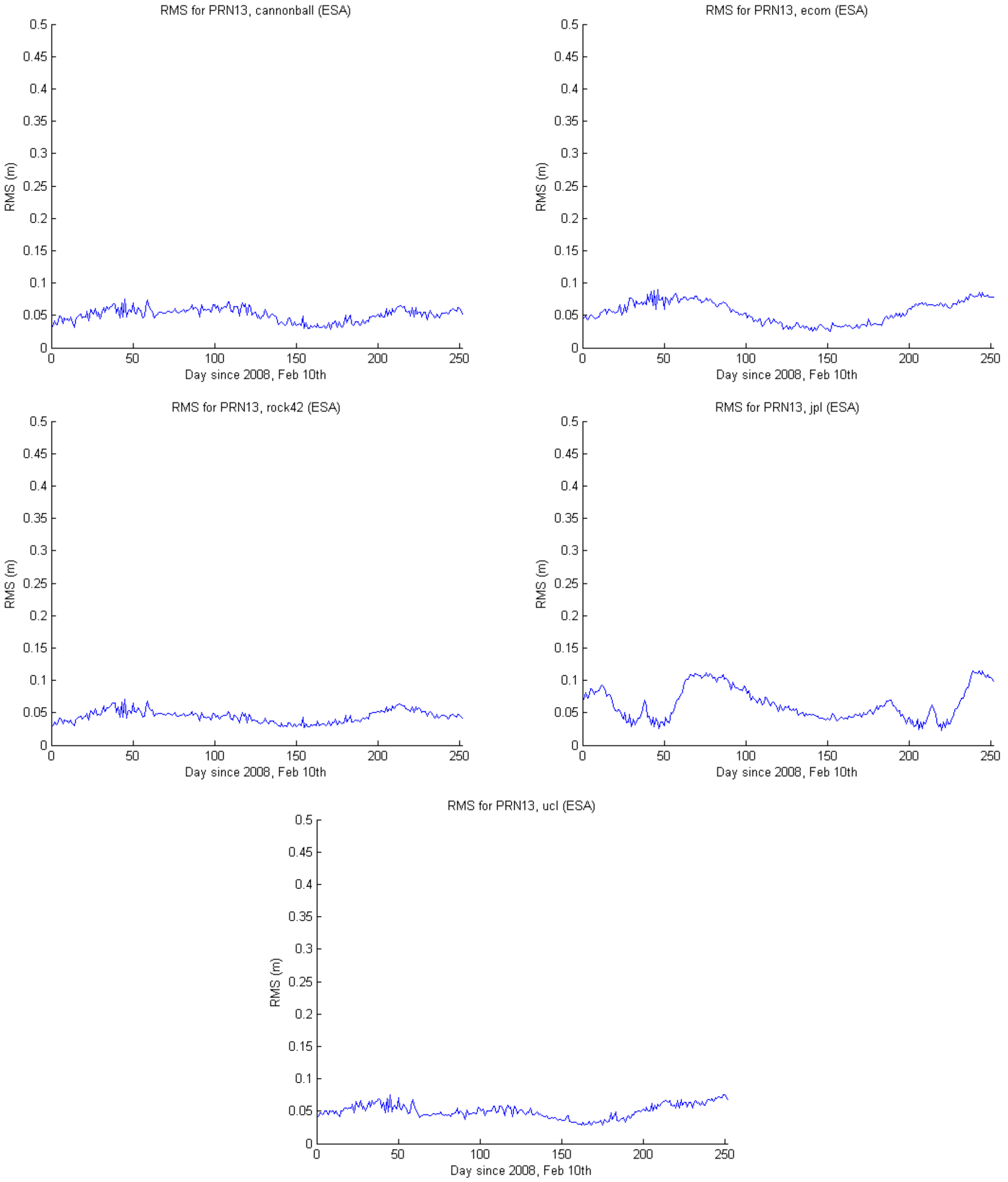

Figure 5.19. RMS evolution - ESA ephemerides - 2008 - PRN13

Chapter 6

Results

6.1 ORBIT PREDICTIONS

The main focus of this section is to investigate different ways of handling parameters during orbit predictions. The first goal is thus to obtain a precise predicted orbit for any GPS satellite. The orbit obtained is compared with the precise ephemerides computed by the IGS which are believed to have errors under 5 cm [Dow et al., 2005]. A set of simple techniques to handle the parameters is presented along with the use of Fourier series.

6.1.1 Methodology

A few problems occur when trying to predict the position of a GPS satellite. The most important one remains the way some parameters are used in the modeling of non-gravitational forces such as the SRP, the y-bias or the Ct force. Indeed, since we are trying to compute a new trajectory, we cannot use models based solely on the position of the satellite to calculate these forces. In addition, precise initial conditions in position and velocity are necessary to be able to propagate the orbit.

Performing an orbit fit will provide good initial conditions. Figure 6.1 illustrates an example of how this is done. We first perform a 1-day orbit fit from GPS day 92, 2006 (April 2nd 2006). Using the initial conditions given by the fit, we propagate the orbit for 2 days from the epoch time. Note that the actual 1-day prediction takes place from day 93 to day 94.

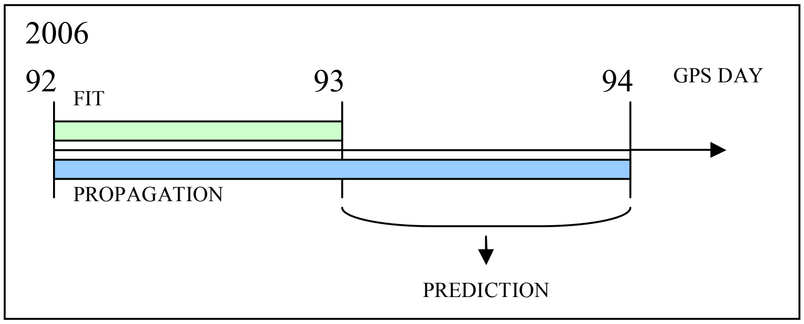

Figure 6.1. Orbit fit followed by an orbit propagation

During the orbit fit, we estimate a state vector consisting of the position and the velocity of the satellite along with two parameters: the SRP scale factor and the y-bias parameter. These two parameters are estimated ten times per day. The IGS ephemerides are used as our observations.

6.1.2 Direct methods

Different ways of handling the parameters during the prediction are possible as shown in Table 6.1. We can adopt the mean of the different values obtained for each parameter and assume that it will remain constant during the prediction. The second method used here assumes that the parameters will follow the same trend in the prediction and in the fit. The third method takes the last estimated value and assumes it remains constant during the prediction.

Method 1	Take the mean value of the estimated parameters over the different subarcs and assume it remains constant over the prediction
Method 2	Assume the parameters will follow the same trend in the prediction as in the fit
Method 3	Take the last value of the estimated parameters over the different subarcs and assume it remains constant over the prediction

Table 6.1. Methods used for the parameters in predictions

For the cases shown in Table 6.2, we estimated the y-bias force along with an SRP scale factor used in each SRP model. The orbit fit starts on GPS day 92, 2006 and the 1-day orbit prediction starts on GPS day 93, 2006. The predicted orbits were computed for the 29 GPS satellites available for this period of time using four different SRP models: ECOM, Cannonball, JPL and ROCK42. Note that the UCL model was not used here since it can only be used for Block IIR satellites.

Methods	1 → mean value 2 → same trend 3 → last value
Estimated parameters	y-bias, SRP scale factor
Time interval for the fit	1 day → 2006 92 (April 2nd)
Time interval for the prediction	1 day → 2006 93
Satellites	29 satellites

Table 6.2. Set up used in the cases studied

The orbit comparison gave for each case an RMS along each component in the RTN frame. A 3D RMS is computed as followed:

$$3D_{RMS} = \sqrt{R_{RMS}^{2} + T_{RMS}^{2} + N_{RMS}^{2}} \tag{6.8}$$

Table 6.3 through Table 6.5 present the 3D RMS's found for the 29 satellites using Method 1, 2 and 3. The 3D RMS's were then averaged over the entire constellation and reported in Table 6.6.

PRN	ECOM 3D RMS (m)	JPL 3D RMS (m)	ROCK42 3D RMS (m)	Cannonball 3D RMS (m)
1	6.52	8.75	7.79	11.56
2	45.42	44.09	42.49	46.05
3	6.59	8.35	8.20	6.57
4	45.98	44.09	43.34	46.60
5	30.75	30.91	32.11	30.49
6	11.61	10.30	10.62	11.86
7	23.59	26.54	23.92	23.57
8	6.63	9.06	8.55	6.15
9	15.39	16.87	15.85	15.79
10	9.29	11.71	12.39	8.88
11	12.25	11.60	12.37	12.46
13	14.98	12.52	14.70	13.29
14	15.86	14.75	14.79	16.27
15	13.37	17.54	15.76	13.64
16	40.47	37.93	38.36	40.98
17	38.33	40.05	39.03	38.24
18	60.45	62.39	61.17	60.85
19	34.30	36.19	36.27	34.79
20	15.79	16.70	16.80	15.94
21	13.93	9.76	12.35	13.69
22	37.02	40.26	38.72	37.45
23	48.76	48.16	49.21	48.48
24	17.01	13.20	14.41	16.79
25	24.77	25.88	26.41	24.60
26	36.78	33.84	33.40	35.96
27	87.19	90.80	89.48	87.19
28	9.72	5.14	7.71	8.93
29	42.94	39.82	39.88	42.29
30	8.98	9.66	9.10	9.33
Mean	**26.71**	**26.79**	**26.73**	**26.85**

Table 6.3. Method 1

PRN	ECOM 3D RMS (m)	JPL 3D RMS (m)	ROCK42 3D RMS (m)	Cannonball 3D RMS (m)
1	0.29	0.22	0.88	0.82
2	0.96	0.75	0.30	1.33
3	1.20	1.19	1.85	1.45
4	0.92	0.51	1.05	1.54
5	0.09	0.20	0.38	0.44
6	0.32	0.58	0.56	0.33
7	1.35	3.05	3.64	1.58
8	0.71	0.86	1.60	0.65
9	0.90	0.21	0.19	0.54
10	1.40	0.11	0.28	1.79
11	1.30	0.64	0.56	0.46
13	1.02	2.39	1.83	1.68
14	1.31	2.64	3.27	1.22
15	0.25	2.01	2.83	0.12
16	0.33	2.26	2.74	0.36
17	1.71	3.29	3.99	1.78
18	1.74	0.37	0.22	1.31
19	1.32	1.04	1.16	0.92
20	0.32	0.38	0.43	0.25
21	0.55	2.05	2.14	0.44
22	0.78	2.85	3.70	1.30
23	1.56	0.87	1.51	0.92
24	1.37	0.74	1.17	1.14
25	0.95	0.24	0.11	1.31
26	0.71	0.34	0.41	0.40
27	0.49	1.29	1.81	0.31
28	1.29	2.37	2.05	0.51
29	0.82	0.30	0.56	0.48
30	0.18	0.82	0.45	0.11
Mean	**0.90**	**1.19**	**1.44**	**0.88**

Table 6.4. Method 2

PRN	ECOM 3D RMS (m)	JPL 3D RMS (m)	ROCK42 3D RMS (m)	Cannonball 3D RMS (m)
1	6.91	17.06	4.67	10.90
2	56.99	33.43	30.79	63.99
3	7.80	7.63	4.81	10.42
4	62.30	37.14	34.64	70.86
5	37.02	39.53	35.57	26.58
6	8.71	14.01	16.59	15.11
7	21.30	22.11	23.34	21.83
8	6.55	28.28	28.79	9.07
9	7.74	15.25	24.06	17.10
10	8.98	17.54	17.65	15.34
11	7.66	9.48	6.73	7.97
13	13.22	8.57	8.96	6.63
14	7.46	9.20	13.27	12.87
15	9.15	50.58	29.08	13.09
16	32.09	13.53	26.54	37.81
17	33.99	35.65	33.90	31.48
18	69.17	87.47	89.85	78.32
19	33.37	43.46	38.20	33.13
20	18.34	18.69	15.68	11.52
21	8.05	37.68	25.60	8.26
22	61.23	77.29	66.01	62.82
23	58.09	44.75	42.43	44.20
24	36.15	4.81	5.08	35.00
25	11.12	32.46	23.54	11.38
26	41.90	33.37	38.07	43.53
27	85.28	114.49	114.30	78.40
28	9.14	14.57	17.24	13.14
29	50.02	36.58	41.54	50.78
30	4.20	10.57	18.60	12.98
Mean	**28.07**	**31.56**	**30.19**	**29.47**

Table 6.5. Method 3

3D RMS (m)	ECOM	Cannonball	JPL	ROCK42
Method 1	26.71	26.85	26.79	26.73
Method 2	0.90	0.88	1.19	1.44
Method 3	28.07	29.47	31.56	30.19

Table 6.6. 3D RMS mean over 29 satellites in the RTN frame for a 1 day predicted orbit

In Table 6.6, it is evident that the best results give an accuracy of about 1 meter. In addition, as we can see in Figure 6.2, Method 2, which assumes that the parameters follow the same trend in the prediction, gives better results than Method 1 or Method 3. Finally, Table 6.6 shows that the Cannonball model seems to give similar results to the ECOM model. This is likely caused by the scale factor absorbing unmodeled errors.

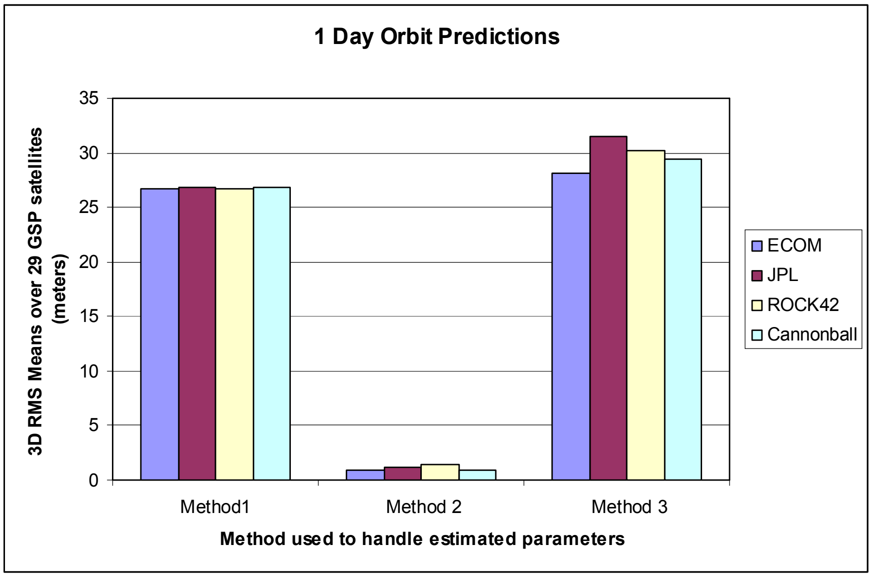

Figure 6.2. Comparison of the different methods

6.1.3 Approximating the parameters with a Fourier series

Another way of handling the parameters during a prediction is to approximate their evolution with Fourier series. By removing the noise and keeping only the main frequencies, we can introduce a more meaningful time series to be used in the orbit prediction.

We first need to obtain the power spectrum of the parameters. Recall that we first need to calculate the Nyquist frequency defined as follows:

$$F_{Nyquist} = \frac{N}{2 \cdot T} \tag{6.9}$$

where

$F_{Nyquist}$ is the Nyquist frequency

N is the number of points computed

T is the final time

Equation (6.9) shows that the larger N is, the higher the Nyquist frequency is and the better the spectrum resolution is. Using MSODP, the number of points computed is related to the length of the subarc used as follows:

$$N = \frac{T}{T_{SUB}} \tag{6.10}$$

where T_{SUB} is the subarc length. Using Equations (6.9) and (6.10), we have Equation (6.11). Therefore, the smaller T_{SUB} is, the higher the Nyquist frequency becomes. Hence,

$$F_{Nyquist} = \frac{N}{2 \cdot N \cdot T_{SUB}} = \frac{1}{2 \cdot T_{SUB}} \tag{6.11}$$

As an example, we computed the time series of the Cannonball scale factor for PRN 01 through a fit to the IGS data. The interval of time was chosen to be 37 days from January 1, 2007, to avoid high values due to eclipse seasons. The time series is plotted in Figure 6.3 followed by its spectrum in Figure 6.4. Here $T_{SUB} = 0.05$ day and thus $F_{Nyquist} = 10$ cycles/day.

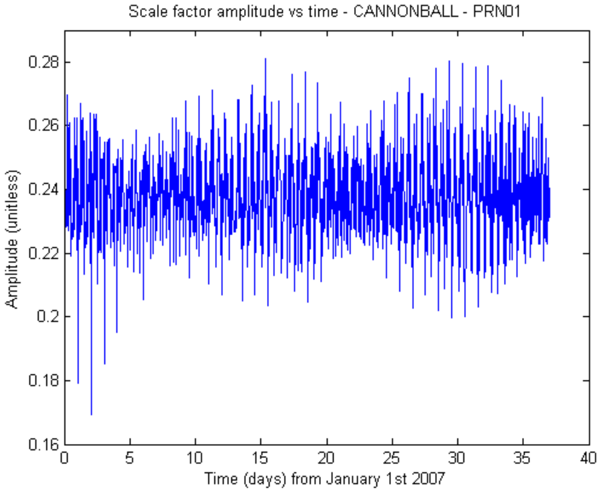

Figure 6.3. PRN 01, Cannonball scale factor

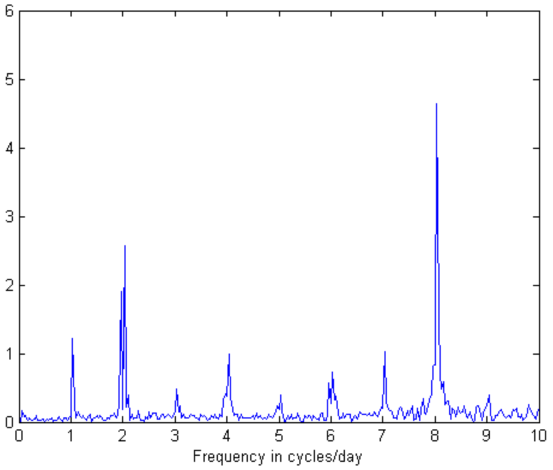

Figure 6.4. Cannonball scale factor, frequency spectrum

The next step is to keep only frequencies with high amplitude. For instance, in the previous example, we can keep all frequencies with an amplitude of 0.5 or higher as seen in Figure 6.5. To calculate the filtered time series, we need to use the inverse Fourier transform. In the following example, we used both the discrete inverse Fourier transform algorithm and the analytical Fourier transform.

The filtered time series using both the discrete and the analytical inverse Fourier transform were then used in a prediction case and compared with the original time series. The following experiment was conducted over a one day prediction on January 30, 2007, using PRN 01 and the Cannonball SRP model. Note that the y-bias parameter was approximated the same way. Initial position and velocity were obtained after a fit to the IGS data as explained in Section 6.1.1.

Time series used	**3D RMS (m)**
Estimated	0.317
Filtered: discrete inverse Fourier transform	0.323
Filtered: analytical inverse Fourier transform	1.704

Table 6.7. 3D RMS using different time series

Table 6.7 presents the 3D RMS's obtained after comparison of the predicted orbit with the IGS orbit. Surprisingly, the 3D RMS's obtained using the filtered time series is higher than the one obtained with the estimated time series. One explanation could be that the solar radiation pressure model absorbs other effects. In addition, the interpolation using the analytical inverse Fourier series seems to remove even more unmodeled forces.

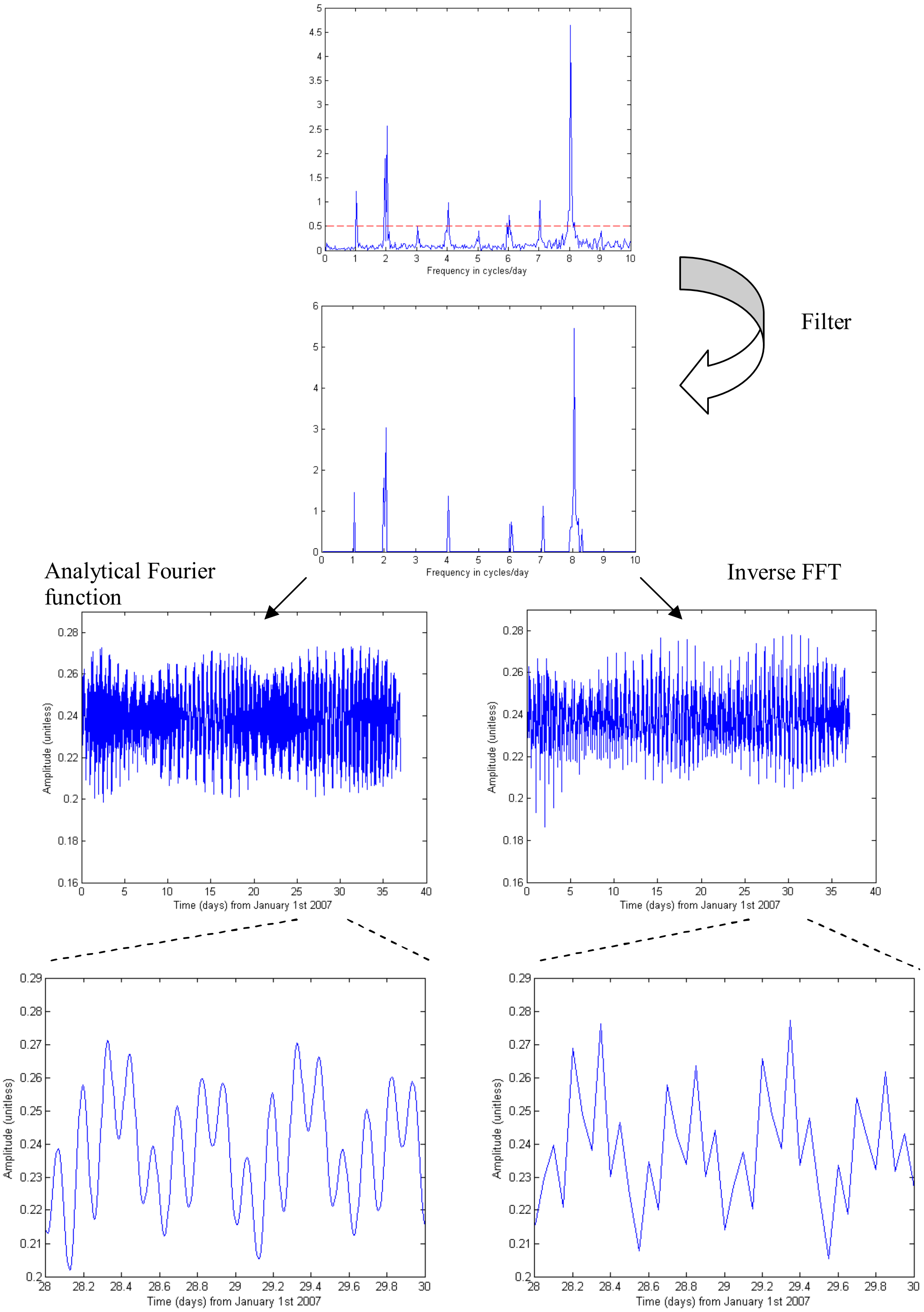

Figure 6.5. Analytical Fourier series and inverse Fourier transform

6.1.4 Conclusion

One of the main problems associated with GPS orbit predictions (or any satellite) is the methodology used to handle the different parameters used in the dynamical models and especially the determination of representing unknown variations in those parameters. Several experiments were conducted using different direct ways to approximate these parameters as well as methods involving Fourier series. The results showed that on first approximation, we can use the average of the estimated time series in the prediction. We could also use discrete Fourier transform although the approximation that gave the closest results to the IGS data consists in using directly the time series estimated during the orbit fit into the orbit prediction.

6.2 SRP MODELS

In the following section, we compared the five SRP models described in Section 4.5: the Cannonball model, the ECOM model, the early JPL model, the ROCK42 model and the UCL model. One way to examine the behavior of different SRP models is to use them in the dynamical model and determine their performance in representing the precise ephemerides from IGS both in fitting GPS ephemerides as well as in predictions.

6.2.1 Orbit Fits

6.2.1.1 PRN 16

For the following sets of experiments, we chose an example Block IIR satellite, PRN 16, (SVN 56), since the UCL SRP model implemented in this study cannot be used for Block II/IIA. In the different fits, we estimated the initial position and velocity along with the SRP scale factor and the y-bias parameter. The IGS final products described in

Section 1.3 were taken as our observations. This approached is justified earlier in Chapter 5. The arc and subarc lengths (see Section 3.1) vary depending on the experiment.

Using a significant arc length would increase the error between the models and the observations and thus would also emphasize the differences between the different dynamical models. To begin with, we chose an arc length of 364 days starting from day 0 of GPS week 1356 (January 1st 2006). We performed five different orbit fits using the five different models. Initial position and velocity are being estimated. The SRP scale factor and the y-bias parameter were both estimated once per day. The resulting RMS's of position differences shown in Table 6.8 are uncharacteristically high and probably suggest that a maneuver occurred during the time span.

PRN 16	**RMS (m)**
Cannonball	972 088
ECOM	972 082
JPL	972 078
ROCK42	972 090
UCL	972 736

Table 6.8. PRN 16, 364-day arc, 1-day subarc

The existence of a maneuver is confirmed by examining the evolution of the estimated SRP scale factor. Figure 6.6 shows the ECOM scale factor. A strong peak is visible in Figure 6.6 just before day 300. Note that all the different models show a similar scale factor evolution. By examining the archived Notice Advisory to NAVSTAR Users (NANU), we see that repositioning maneuvers occurred in 2006 on day 292 and day 298.

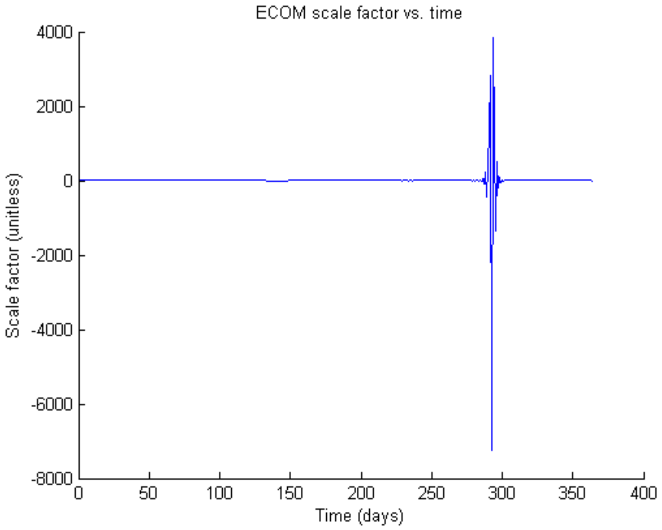

Figure 6.6. PRN 16, 364 days, 1-day subarc, initial epoch: 1356, 0

Other features are visible during the 364-day time span. At the top of Figure 6.7 we can see an expansion of Figure 6.6. The maneuver still shows with strong variations on the right side of the plot. We also see variations between day 200 and day 250. The eclipse factor, plotted at the bottom of Figure 6.7, show that they correspond to an eclipse season. Interestingly, only very small variations are seen during the first eclipse season. This is perhaps due to the way the batch estimator behaves over such a long arc length. An unexpected variation occurs around day 140 and is probably due to the same reason. To investigate more the variation seen around day 140, we performed a similar orbit starting at day 110 with an arc length of 50 days. Initial position and velocity were estimated. The ECOM scale factor and the y-bias parameter were estimated once per day. In this experiment, the variation around day 140 seen in Figure 6.7 does not show, which suggests that it might be due to the arc length being too big. In our next experiment, to make sure we do not face abnormally high RMS, we used a 100-day arc length.

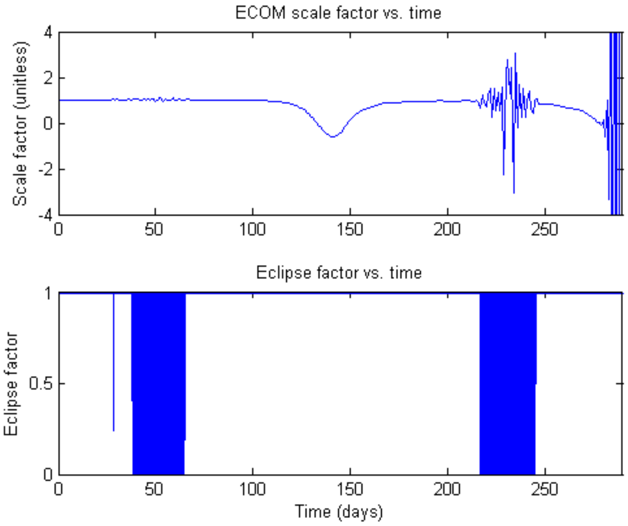

Figure 6.7. ECOM scale factor and eclipse factor

If we examine now the RMS's of the different orbit fits (Table 6.9), the Cannonball model along with the ROCK42 and the UCL have the smallest value. However, looking at the evolution of the scale factor of each model can give an indication of how well SRP is modeled. Indeed, for the ECOM, JPL, ROCK42 and UCL model, a scale factor value of 1 indicates that the model would perfectly take into account the perturbations due to SRP (see Chapter 4). Note that in the Cannonball case, the scale factor is a representation of the reflectivity coefficient whose true value is unknown but whose approximate a priori value is taken to be 0.2 [Craig, 2001].

PRN 16	**RMS (m)**
Cannonball	7.3
ECOM	12.9
JPL	11.7
ROCK42	7.1
UCL	7.4

Table 6.9. PRN 16, 100-day arc, 1-day subarc

Figure 6.8 represents the evolution of the scale factor for the five different models. We can see that in the ECOM and UCL model case, the scale factor tends to stay closer to their a priori value than in the JPL or ROCK42 model case. Note that the first eclipse season seen in Figure 6.8 can be observed here around day 50 in each case. The high scale factor values seen in some cases could be a sign that some models are absorbing more dynamical errors than expected and thus fit the IGS data better resulting in a low RMS.

The evolutions of the scale factors presented in Figure 6.8 were obtained using a 300 seconds step size in the numerical integration. Figure 6.9 exhibits the evolutions of the different scale factors obtained with a 50 seconds step size. The differences between the evolution of the scale factor using a step size of 50 seconds and the one using a step size of 300 seconds are shown in Figure 6.10. These differences are of the order of 10^{-2} during the eclipse season, which is small compared to the average values of the scale factors of approximately 1 or 0.5. For better accuracy, a smaller step size of 50 seconds would be more appropriate to examine the evolution during eclipse seasons. However, the general characteristics of the scale factors evolutions are unchanged by changing the step size. A step size of 300 seconds was kept in the rest of the study for computing purposes.

To examine how the scale factor is used by the different models, we performed the same experiment but using a 100-day subarc for both SRP and y-bias. It means that these factors get estimated only once and that all the error should go into these two coefficients.

Table 6.10 shows that both the ECOM and the UCL model have an estimated scale factor that remains close to 1. On the other hand, other models, like the ROCK42, have a greater difference between the estimated scale factor value and the ideal value of 1, which confirms what was assumed in experiment 2: some models absorb more of the error in their scale factor. Thus, even an inadequate dynamical model could perform well by absorbing the error in the scale factor. It is then not so simple to distinguish which model is more accurate. In order to get a better insight, a simple test can be performed. The idea is to prevent the models from using the scale factor to absorb unmodeled errors. By forcing its value to be 1, which means that we assume that SRP is perfectly modeled, all the error should then be exhibited in the RMS of the fit. Note that for the Cannonball model, we fixed the scale factor to its approximate a priori value of 0.2.

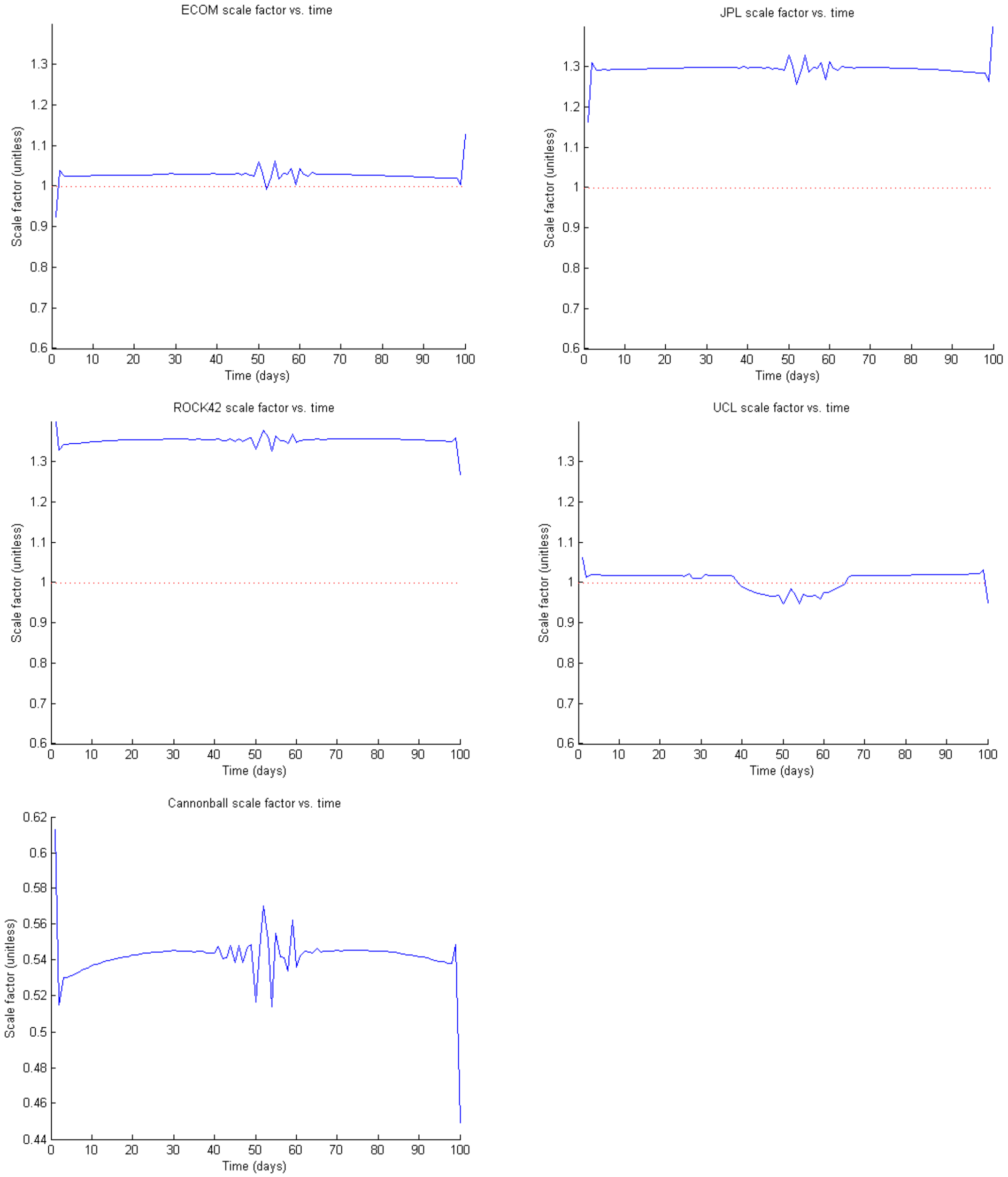
ECOM scale factor vs. time

JPL scale factor vs. time

ROCK42 scale factor vs. time

UCL scale factor vs. time

Cannonball scale factor vs. time

Figure 6.8. Scale factor evolution, PRN 16, 100-day arc, 1-day subarc

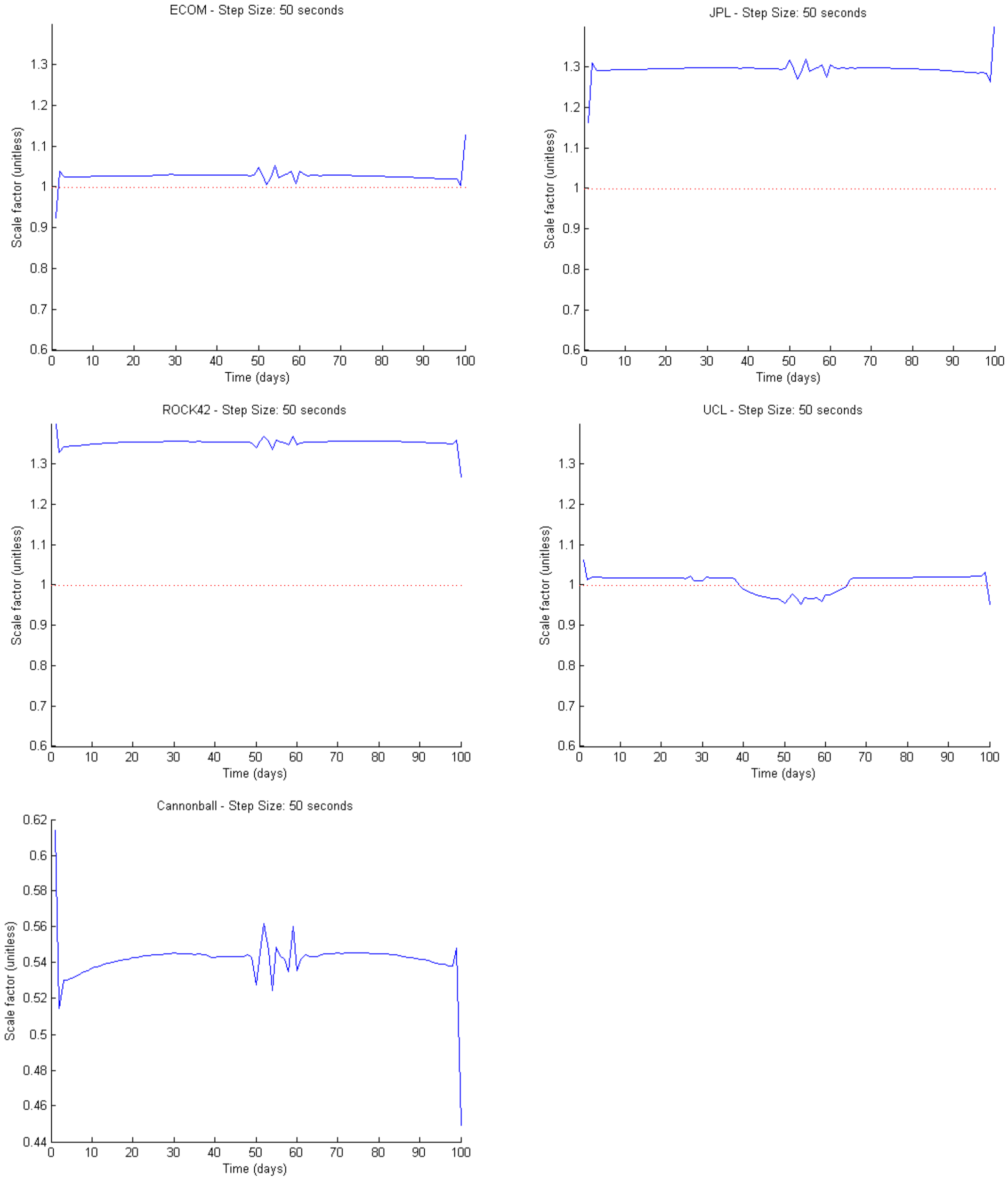

Figure 6.9. Scale factor evolution, step size: 50 seconds

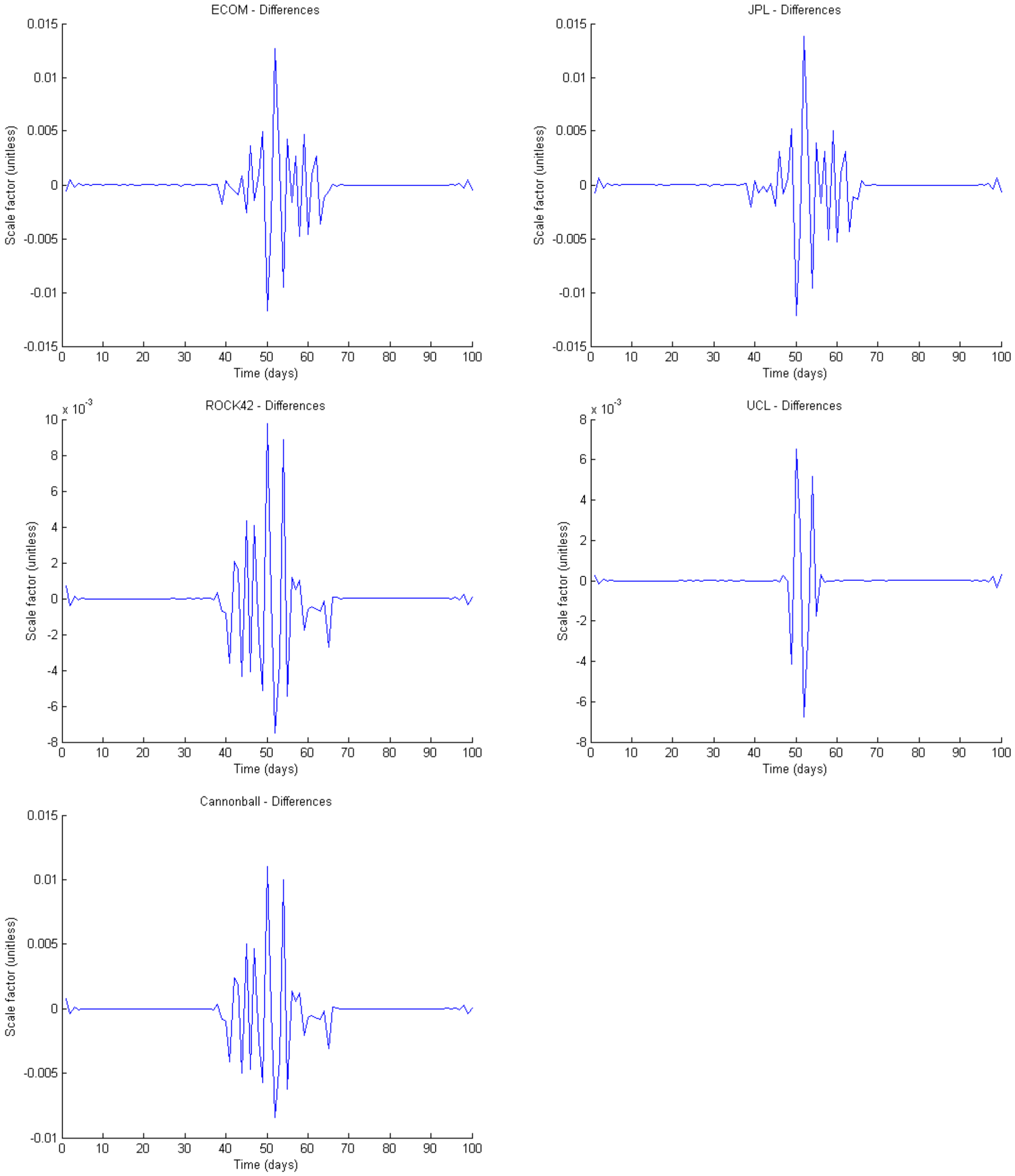

ECOM - Differences

JPL - Differences

ROCK42 - Differences

UCL - Differences

Cannonball - Differences

Figure 6.10. Scale factor differences

PRN 16	**Scale factor**	**y-bias (pm/s$^{\wedge 2}$)**	**RMS (m)**
Cannonball	0.54	-208	38.7
ECOM	1.03	380	239.8
JPL	1.28	-230	301.1
ROCK42	1.35	-212	29.5
UCL	0.99	-2	307.6

Table 6.10. PRN 16, 100-day arc, 100-day subarc

This experiment is the same as the previous one, except that the scale factor has been fixed to its nominal value. The results in Table 6.11 confirm what was suspected: most of the error is going into the RMS value. The UCL model and the ECOM model give the lowest RMS's. The Cannonball model gives a much higher value followed by the JPL model and the ROCK42 model. It is not surprising since the Cannonball model, the ROCK42 model and the early JPL model are all older models than the ECOM or the UCL model. As far as the y-bias is concerned, the values stay close to what they were in the previous experiment which suggests that the y-bias parameter does not absorb unmodeled errors like the SRP scale factor. The y-bias parameter is close to 0 in the UCL case which might suggest that the UCL model already account for the y-bias force. However, for other satellites, the y-bias does not stay close to 0 in the UCL case (see Table 6.13). In Table 6.10, the ECOM model shows a value of opposite sign for the y-bias parameter which is not always the case for the other satellites in Table 6.13.Since in these experiments only one value of the y-bias parameter was estimated over the entire interval of time, it is difficult to draw any conclusions with respect to the y-bias parameter. A more thorough study of the y-bias parameter is provided in Section 6.3.

PRN 16	Scale factor	y-bias (pm/s^2)	RMS (m)
Cannonball	0.2	-186	859.7
ECOM	1.0	366	262.6
JPL	1.0	-204	896.0
ROCK42	1.0	-186	1006.6
UCL	1.0	-2	307.8

Table 6.11. PRN 16, 100 days, 100-day subarc, fixed scale factor

An eclipse season occurs during the 100-day period used in the previous cases. To check that it does not influence the results found in the previous experiment, the interval of time was reduced to 37 days so it would terminate just before the eclipse season. Table 6.12 shows that the results in this case are similar to the previous experiment. Once again, the UCL and ECOM model gives the lowest RMS's.

PRN 16	Scale factor	y-bias (pm/s^2)	RMS (m)
Cannonball	0.2	-217	291.3
ECOM	1.0	384	33.7
JPL	1.0	-223	298.6
Rock42	1.0	-222	342.9
UCL	1.0	-27	34.2

Table 6.12. PRN 16, 37-day arc, 37-day subarc, fixed scale factor

6.2.1.2 Other Block IIR satellites

To confirm the observations of Section 6.2.1.1, similar experiments were conducted using all the other Block IIR satellites available for this interval of time. The arc length is 100 days, the subarc length is 100 and the scale factor is fixed. The results are shown in Table 6.13

.

PRN 02	y-bias	RMS
Cannonball	-130	498.6
ECOM	528	65.7
JPL	-138	515.7
ROCK42	-144	588.7
UCL	83	56.9

PRN 11	y-bias	RMS
Cannonball	-59	487.5
ECOM	-332	83.9
JPL	-56	504.2
ROCK42	-54	573.9
UCL	144	78.8

PRN 13	y-bias	RMS
Cannonball	393	702.8
ECOM	424	80.3
JPL	398	721.2
ROCK42	398	835.3
UCL	539	65.2

PRN 14	y-bias	RMS
Cannonball	397	712.7
ECOM	1253	113.2
JPL	391	731.2
ROCK42	392	845.9
UCL	567	53.8

PRN 18	y-bias	RMS
Cannonball	315	858.4
ECOM	1139	135.3
JPL	239	904.6
ROCK42	327	1007.3
UCL	374	148.6

PRN 19	y-bias	RMS
Cannonball	2396	102 599
ECOM	2468	102 718
JPL	2395	102 609
ROCK42	2395	102 606
UCL	2417	102 694

PRN 20	y-bias	RMS
Cannonball	-12 546	83 469
ECOM	-12 486	83 450
JPL	-12 554	83 560
ROCK42	-12 547	83 477
UCL	-12 535	83 482

PRN 21	y-bias	RMS
Cannonball	83	456.9
ECOM	364	24.3
JPL	73	473.1
ROCK42	68	545.4
UCL	286	46.8

PRN 23	y-bias	RMS
Cannonball	97	768.5
ECOM	784	786.3
JPL	98	787.9
ROCK42	95	903.6
UCL	250	68.7

PRN 28	y-bias	RMS
Cannonball	149	810.2
ECOM	-222	136.1
JPL	118	860.6
ROCK42	136	958.4
UCL	324	265.0

Table 6.13. Block IIR satellites, 100-day arc, 100-day subarc, fixed scale factor

PRN 19 and PRN 20 show unexpected high RMS values. By examining the 2006 NANU, we can see there was one maneuver for PRN19 on day 24 and two maneuvers for PRN20 on day 61 and 62. New cases were made to avoid these maneuvers. For PRN 19, we chose a 23-day arc as well as a 23-day subarc so the estimation would stop before the maneuver. Similarly, we chose a 60-day arc and a 60-day subarc for PRN 20. Results for these two cases are shown in Table 6.14.

PRN 19	**y-bias**	**RMS**
Cannonball	369	355.4
ECOM	1075	23.2
JPL	365	365.6
ROCK42	364	419.8
UCL	560	26.8

PRN 20	**y-bias**	**RMS**
Cannonball	782	282.1
ECOM	1387	9.0
JPL	777	289.3
ROCK42	776	333.6
UCL	926	23.2

Table 6.14. PRN 19 and PRN 20

6.2.1.3 Behavior during an eclipse season

As we can see in Figure 6.7, an eclipse season occurs between day 45 and day 60 for PRN 16. The interval of time of the fit was chosen to begin at day 45 and to end at day 60 so it would match the duration of the eclipse season. Two experiments were carried out. During the first one, one SRP scale factor and one y-bias parameter were estimated. For the second experiment, only one y-bias parameter was estimated to prevent the SRP scale factor to absorb unmodeled error.

In Table 6.15, the RMS's vary from 1.5 m to 10.1 m. The ROCK42 model gives the lowest value. The UCL model gives a RMS comparable to the ECOM model. As seen before, the scale factor seems to absorb a significant part of the error in some cases. Table 6.16, when most of the error goes into the RMS value, we see that the ECOM and UCL model give the lowest RMS's during the eclipse season.

PRN 16	Scale factor	y-bias	RMS (m)
Cannonball	0.54	-66	1.7
ECOM	1.03	334	6.7
JPL	1.30	-35	10.1
ROCK42	1.35	-66	1.5
UCL	0.96	-18	6.1

Table 6.15. PRN 16, eclipse season

PRN 16	y-bias	RMS (m)
Cannonball	171.7	134.7
ECOM	353.6	18.6
JPL	202.6	138.4
ROCK42	213.6	157.8
UCL	-55.0	22.9

Table 6.16. PRN 16, eclipse season, fixed scale factor

6.2.2 Predictions

6.2.2.1 PRN 16

Another way of testing SRP models is to examine orbit predictions which will emphasize the dynamical model errors. We only use IGS data to determine the initial conditions as it is explained in more details within Section 6.1.

In the following experiments, we will use the ‘same trend’ method where we assume that the parameters will follow the trend of the estimated values in the predictions (see Section 6.1.2). Furthermore, to prevent the models from absorbing too much error in the SRP parameter, we chose to force it to have its ideal value of 1 for all the models except for the Cannonball model where we used its approximate a priori value of 0.2. The satellite used remains PRN16. The fit used to obtain the initial conditions was performed during 1 day from day 2 of 2006 as we can see in Figure 6.11. The actual predictions were performed from day 3 of 2006 for 1, 2, 3 and 30 days. The predicted orbits were then compared to the IGS orbits and the 3D RMS's in the Radial-Transverse-Normal (RTN) frame are shown in Table 6.17. The RTN frame is defined as follows: the radial axis R lies along the line that links the center of mass of the Earth to the center of mass of the satellite. The transverse axis T is perpendicular to the R axis and lies along the satellite path. The normal axis N completes the right-handed system. The RTN frame is represented on Figure 6.12.

For the 1-day predictions, we can see that both the ECOM and UCL model have 3D RMS's of a few meters whereas the other models show RMS's of up to a few tens of meters. The 2- and 3-day predictions cases confirm the 1-day case. The 30-day prediction case also confirms the 1-day case but also seem to emphasize the difference between the models. The UCL model also shows slightly lower RMS's than the ECOM model.

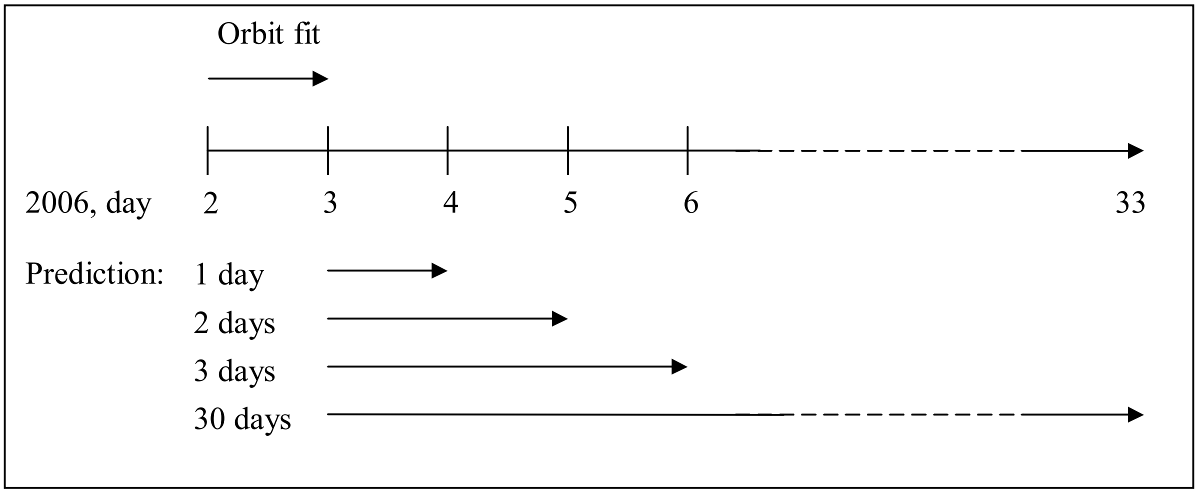

Figure 6.11. PRN 16, orbit predictions

SRP model	3D RMS (m) over 1 day	3D RMS (m) over 2 days	3D RMS (m) over 3 days	3D RMS (m) over 30 days
UCL	2.4	6.5	12.6	248.3
ECOM	2.5	6.5	12.7	256.9
Cannonball	27.6	74.5	146.7	2860.1
JPL	28.3	76.4	150.4	2939.6
ROCK42	32.6	88.2	173.5	3383.8

Table 6.17. PRN 16 (plane B), 3D RMS (m) over 1, 2, 3 and 30 day predictions

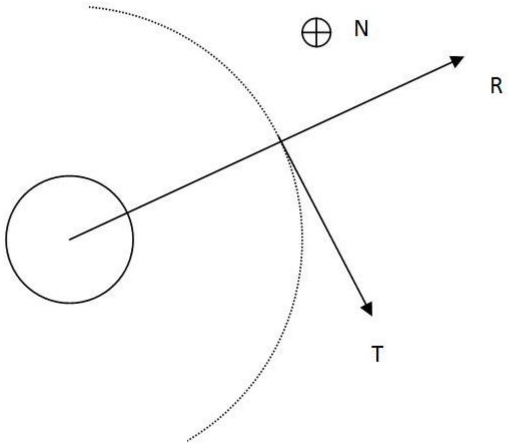

Figure 6.12. The Radial-Transverse-Normal (RTN) frame

6.2.2.2 Other Block IIR satellites

To confirm the above results, we considered one Block IIR satellite per plane where Block IIRs were present. Results can be seen in Table 6.18 through Table 6.21. These different cases show that the ECOM model and the UCL model give the lowest 3D RMS's. The ROCK42 model on the other hand shows the highest 3D RMS in most cases.

SRP model	**3D RMS (m) over 1 day**	**3D RMS (m) over 2 days**	**3D RMS (m) over 3 days**	**3D RMS (m) over 30 days**
ECOM	0.3	0.8	1.4	46.2
UCL	1.0	2.0	3.7	132.6
Cannonball	11.7	25.4	49.4	1925.9
JPL	12.1	30.3	59.0	2015.4
ROCK42	13.6	26.6	51.6	2299.3

Table 6.18. PRN 19 (plane C), 3D RMS (m) over 1, 2, 3 and 30 day predictions

SRP model	**3D RMS (m) over 1 day**	**3D RMS (m) over 2 days**	**3D RMS (m) over 3 days**	**3D RMS (m) over 30 days**
ECOM	3.7	9.9	19.6	1 677.4
UCL	4.6	12.4	24.5	2 072.3
Cannonball	39.3	105.8	209.9	18 176.1
JPL	40.1	107.8	213.8	18 551.8
ROCK42	46.2	124.5	246.8	21 352.0

Table 6.19. PRN 11 (plane D), 3D RMS (m) over 1, 2, 3 and 30 day predictions

SRP model	**3D RMS (m) over 1 day**	**3D RMS (m) over 2 days**	**3D RMS (m) over 3 days**	**3D RMS (m) over 30 days**
UCL	3.3	8.2	14.9	762.4
ECOM	5.3	14.0	26.2	1 529.3
Cannonball	46.7	121.0	224.3	12 212.4
JPL	48.1	125.4	232.8	12 671.9
ROCK42	54.9	142.4	263.9	14 392.1

Table 6.20. PRN 18 (plane E), 3D RMS (m) over 1, 2, 3 and 30 day predictions

SRP model	3D RMS (m) over 1 day	3D RMS (m) over 2 days	3D RMS (m) over 3 days	3D RMS (m) over 30 days
ECOM	1.7	3.0	4.3	50.2
UCL	1.9	3.1	4.7	404.1
Cannonball	29.2	45.7	60.8	1 763.6
JPL	30.1	47.4	63.3	1 440.8
ROCK42	34.7	54.3	72.3	2 061.6

Table 6.21. PRN 14 (plane F), 3D RMS (m) over 1, 2, 3 and 30 day predictions

During the orbit fits performed on Block IIR satellites in Section 6.2.1, the UCL model and the ECOM model provided the lowest RMS's of position differences. The other models led to higher RMS's. In Section 6.2.2, when comparing the IGS ephemerides to predicted orbits over 1, 2, 3 and 30 days, the UCL model and the ECOM model case exhibited the lowest RMS'S. These results are consistent with the comparison of the orbit fits.

6.2.3 SLR Residuals

Until this point, we mostly used IGS data to study the dynamics of GPS orbits. Satellite Laser Ranging (SLR) provides a set of independent data that can be used to confirm some of the observations already made using IGS data.

In this section, we used SLR data to compare the different SRP models. SLR range residuals (described in Section 6.2.3.1 below) were computed for orbits generated using different SRP models. Although SLR provides us with very accurate measurements, it is limited as far as the GPS constellation is concerned. Indeed, only two satellites have been equipped with Laser Retroreflector Array (LRA), namely SVN 35 and SVN 36. SLR data are thus available only for these two satellites. Note that they are both Block IIA satellites which prevents us from using the UCL model, which applies only to Block IIR satellites. However, by allowing us to compare the performances of the other SRP models, SLR data can validate our previous approach based on IGS data.

6.2.3.1 Residuals

A range residual is a difference between an observed range and a computed range. The computed range is defined as follows [Rim and Schutz, 2002]:

$$R_{SLR} = \left\| \vec{R}_{SAT} - \vec{R}_{GS} \right\| + \Delta_{atmosphere} + \Delta_{relativity} + \left\| \vec{X}_{LRA/CM} \right\|_{p} \tag{6.1}$$

where:

R_{SLR}	is the computed range
$\vec{R}_{SAT}$	is the position vector of the satellite in the International Terrestrial Frame 2005 (ITRF 2005)
$\vec{R}_{GS}$	is the position vector of the ground station in the ITRF 2005
$\Delta_{atmosphere}$	is the correction for the tropospheric delay
$\Delta_{relativity}$	is the correction for the general relativity effects
$\left\| \vec{X}_{LRA/CM} \right\|_{p}$	is the projected value of the position of the LRA with respect to the center of mass of the satellite in the direction $\vec{R}_{SAT}$ - $\vec{R}_{GS}$

Figure 6.13 shows the geometry. To get the position vector of the satellite we first calculate precise initial conditions using IGS data as observations in MSODP. We then generate an orbit by propagating the dynamical equations from those initial conditions. In the following experiments, different orbits were generated using different SRP models.

The observed range is obtained using SLR normal point data provided by CSR. MSODP is then used to obtain a series of range residuals over time.

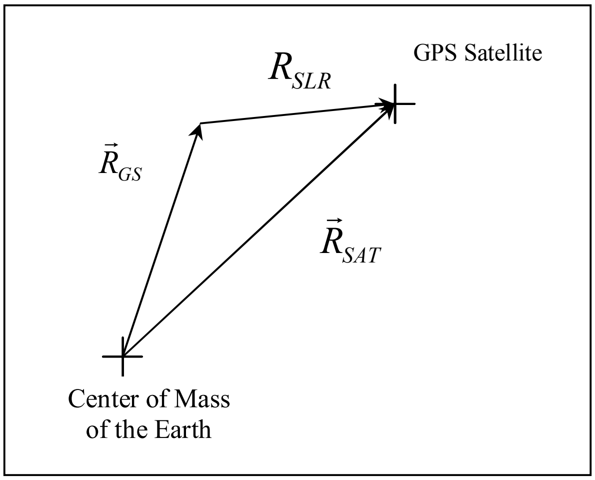

Figure 6.13. SLR geometry

6.2.3.2 Setup

To calculate the residuals, we first need to know the precise position of the Laser Retroreflector Array (LRA) with respect to the center of mass. As illustrated in Figure 6.14, we can calculate this vector by subtracting the position of the center of mass of the satellite to the LRA offset as follows:

$$\vec{X}_{LRA/CM} = \vec{X}_{LRAoffset} - \vec{X}_{CM} \tag{6.2}$$

The position of the center of mass of the satellite varies as the fuel is consumed. The average value in millimeters is:

$$\vec{X}_{CM} = \begin{bmatrix} 0 \\ 0 \\ 1011.4 \end{bmatrix} \tag{6.3}$$

The schematics in Figure 6.14 provided by the International Laser Ranging Service (ILRS) [Pearlman et al., 2002] allow us to determine the LRA offset with respect to the origin. The values of the components are given in millimeters:

$$\vec{X}_{LRAoffset} = \begin{bmatrix} 862.6 \\ -524.5 \\ 1669.8 \end{bmatrix} \tag{6.4}$$

Then, using Equation (6.2), we have:

$$\vec{X}_{LRA/CM} = \begin{bmatrix} 862.6 \\ -524.5 \\ 658.4 \end{bmatrix} \tag{6.5}$$

More accurate data, including current center of mass information, are directly provided by the ILRS [ILRS, 2008]. The following values were used in MSODP:

For PRN 05 (SVN 35):

$$\vec{X}_{LRA/CM} = \begin{bmatrix} 862.58 \\ -524.51 \\ 669.5 \end{bmatrix} \tag{6.6}$$

For PRN 06 (SVN 36):

$$\vec{X}_{LRA/CM} = \begin{bmatrix} 862.58 \\ -524.51 \\ 671.7 \end{bmatrix} \tag{6.7}$$

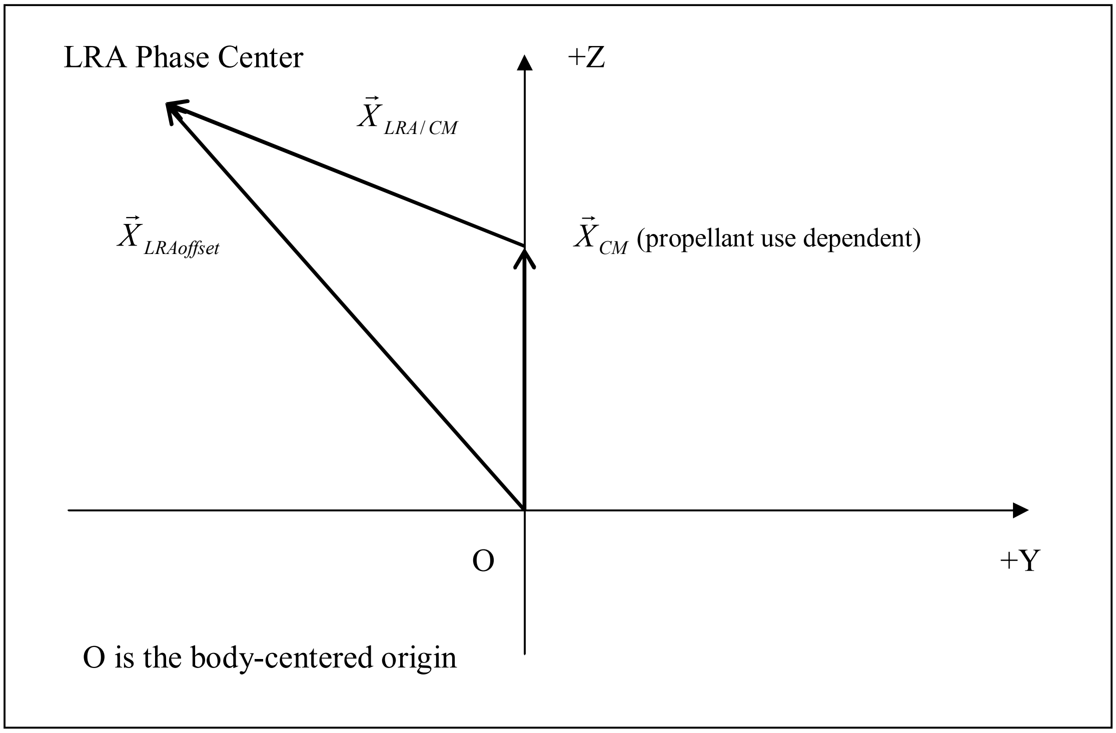

Figure 6.14. LRA Phase Center

6.2.3.3 Experiments

In this experiment, SLR range residuals were computed using one week of SLR data. Using relatively short periods of time should lead to low RMS's of the residuals. The first week used was GPS week 1461 (2008, January 6th). We then processed 18 more consecutive weeks of SLR data and combined the residuals. After combining the weekly residuals, we obtain the statistics of Table 6.22.

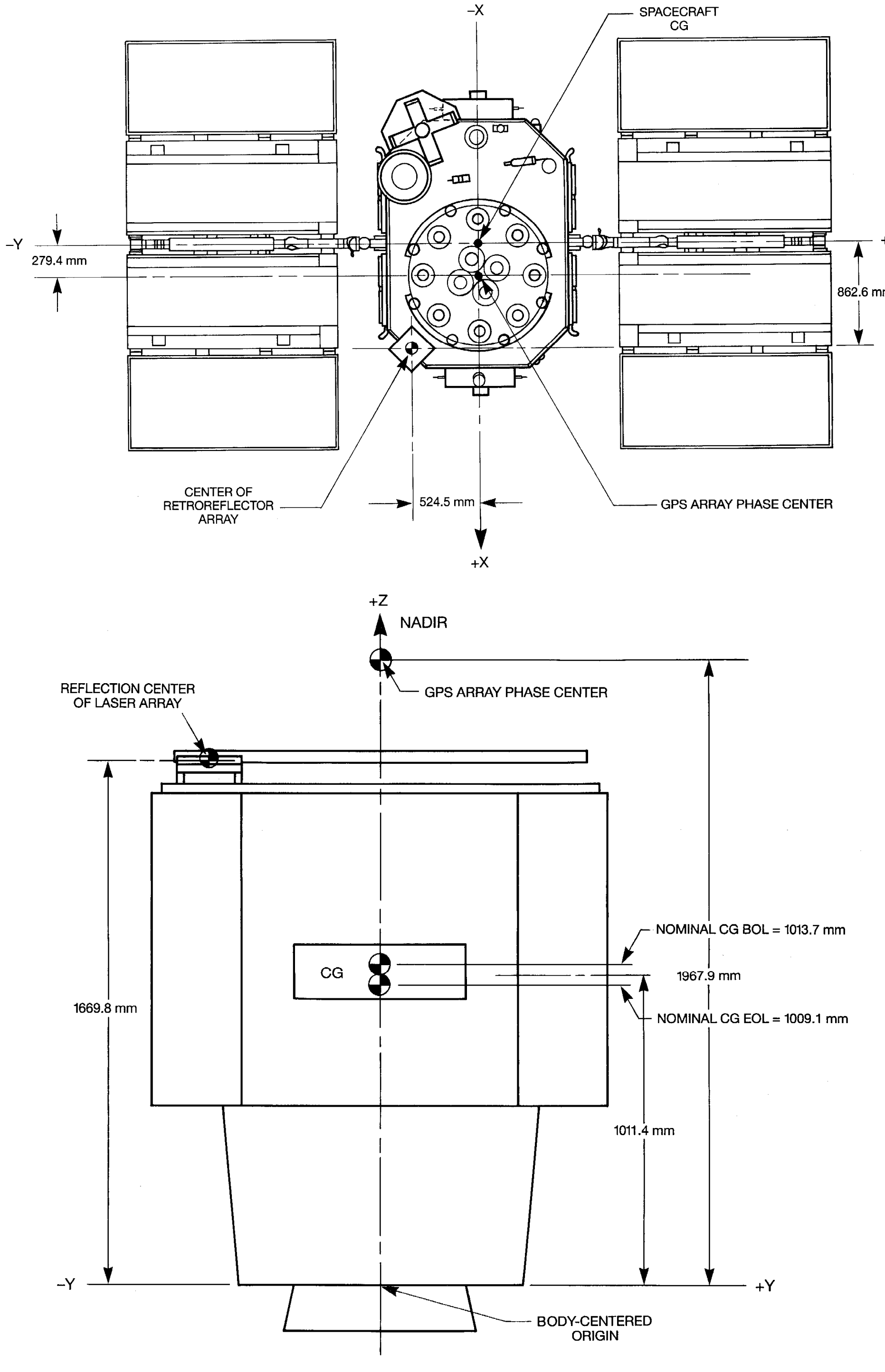

Figure 6.15. XY view (above) and YZ view (below) for satellite SVN 35, SVN 36

SRP model	Number of observations	RMS (cm)	Mean (cm)
Cannonball	872	3.35	0.1
ECOM	872	3.34	-0.3
JPL	872	3.36	-1.3
ROCK42	872	3.36	-1.9
IGS	872	3.34	-0.2

Table 6.22. SLR residuals, PRN 05, short arcs (18 weeks)

The RMS's for all the different cases are really close to each other and it is thus difficult to distinguish which SRP model is more consistent with the SLR data. A longer period of time should be used in order to increase the differences seen in the RMS's. Thus, in the next experiment, one year of SLR data were used.

To emphasize the errors due to the dynamical model, range residuals were computed using 363 days starting from 2006, January 2nd. The resulting RMS's of residuals were found to be uncharacteristically high. The NANU archives from the USCG Navigation Center indicate that two maneuvers were performed on PRN 05 in 2006. The first maneuver occurred on day 227 and the second on day 349. Details can be found in NANU 2006072 and NANU 2006159.

To eliminate maneuvers in the residuals, we only used the first 210 days instead of the 363 day interval. The RMS's of the residuals are shown below in Table 6.23. As expected, we can now observe significant differences between the cases. Again, the IGS orbit is used as a reference. The ECOM model clearly shows the lowest RMS after the IGS.

To compare the results obtained with the SLR data to the one obtained with the IGS data, four orbit fits were performed over the same interval of time using the four different SRP models. The IGS precise ephemerides were taken as our observations.

Initial position and velocity were estimated along with the SRP scale factor and the y-bias parameter. The SRP scale factor and the y-bias parameter were estimated once per day. The resulting RMS's of position differences of the different orbit fits in Table 6.23 indicate that the ECOM model leads to the lowest RMS in fit which is consistent with the results obtained through the SLR residuals. Moreover, the RMS's in orbit fits in the other cases are consistent with the RMS's of SLR residuals obtained earlier. For example, the Cannonball model leads to the highest RMS both in fitting the IGS data and in SLR residuals.

SRP model	**Number of observations**	**SLR** RMS (cm)	**IGS Fit** RMS (m)
Cannonball	1910	330.68	22.71
ROCK42	1910	329.46	22.47
JPL	1910	101.98	6.07
ECOM	1910	49.24	2.85
IGS	1910	16.95	N/A

Table 6.23. SLR residuals, PRN 05, long arc (210 days)

A similar experiment was conducted with satellite PRN 06. In order to pick a reasonable interval of time, we plotted the scale factor time series of an orbit fit to IGS data over one year. In Figure 6.16, we can see that an obvious maneuver occurred around day 100. To eliminate it from the residuals, the interval of time was chosen to be from day 110 to day 363 (253 days). SLR residuals were computed and are shown in Table 6.24. The ECOM model case shows the lowest RMS in residuals. Using the same interval of time, four orbit fits using the four different SRP models were performed. Initial position and velocity were estimated along with the SRP scale factor and the y-bias parameter, each being estimated once per day. The RMS's of the different orbit fits are presented in Table 6.24. The ECOM model case shows the lowest RMS in fit. The

RMS's in orbit fits in the other cases are consistent with the RMS's in SLR residuals. For example, the Cannonball model case lead to the highest RMS in SLR residuals and the highest RMS in orbit fit. This is similar to the previous PRN 05 case.

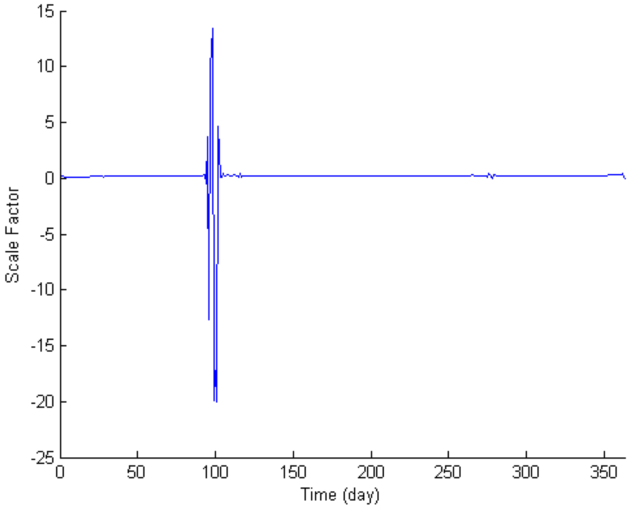

Figure 6.16. Cannonball scale factor for PRN 06 over 363 days from 2006, January 2nd

SRP model	Number of observations	SLR RMS (cm)	IGS Fit RMS (m)
Cannonball	2931	300.53	25.95
ROCK42	2931	300.05	25.83
JPL	2931	70.13	6.56
ECOM	2931	37.71	3.18
IGS	2931	22.69	N/A

Table 6.24. SLR residuals, PRN 06, long arc (253 days)

6.2.3.4 Conclusion

SLR range residuals for PRN 05 and PRN 06 showed that the ECOM model performed better than the other models. In addition, comparing the SRP models using both SLR data and IGS data on the same period of time led to similar rankings in RMS's of SLR residuals and RMS's of the orbit fits. For example, the Cannonball model showed the highest RMS both in SLR residuals and in the IGS fit. The results using SLR data are thus consistent with the results found using IGS data. Although the UCL model could not be used in the previous experiments, these results validate our previous approach using IGS data to compare the different SRP models.

Lastly, it is worth noting that SLR tracking of GPS satellites will end soon with the decommission of SVN 35 and SVN 36. The recent Block IIR-M satellites do not carry corner reflectors. However, "[...] the US Geodetic Requirements Working Group has recommended that Satellite Laser Retro-reflectors be installed on GPS III satellites [...]" [LaBrecque et al., 2008]. Besides, SLR is right now being used for other GNSS satellites such as Galileo In-Orbit Validation Element A and B (GIOVE).

6.3 Y-BIAS EXPERIMENTS

The goal of the following experiments is to observe some of the characteristics of the y-bias force. A short frequency analysis will be presented. Some of the dependencies of the y-bias force will be investigated. For instance, the estimated y-bias force depends on the SRP model used as well as on the GPS satellite Block used.

6.3.1 Frequency analysis

In this part, we examined the frequencies of the y-bias parameter. We first obtained different y-bias time series and then examined their power spectra.

The first step is to calculate the y-bias time series. To that end, we performed several orbit fits using the IGS ephemerides as our observations. We picked two distinct intervals of time in the year 2006. To avoid important changes in behaviour, we chose them to be outside of eclipse seasons. Position and velocity were estimated once a day. To make sure we could observe most of the frequencies, we used a Nyquist frequency of 10 cycle/day. As seen in Section 6.1.3, this implies that we use a subarc length of 0.05 day. In other words, the y-bias parameter will be estimated 20 times per day. In addition, an SRP parameter was estimated four times a day. We used two Block IIAs, PRN 03 and PRN 25, and four Block IIRs in two different planes: PRN 11 and PRN 21 in plane D, PRN 13 and PRN 14 in plane F. We estimated SRP parameters from all the different models used so far. Daily orbit fits were performed consecutively over ten days for two different intervals of time. Similar experiments were conducted using a longer interval of time of thirty days, which led to comparable results.

The top of Figure 6.17 shows the y-bias parameter evolution for PRN 03 over a 10 day period of time in 2006. In this experiment, we used the Cannonball SRP model. The bottom of Figure 6.17 shows the corresponding power spectrum. The peaks represent the main frequencies of the time series. We can see here that the main peak occurs at 2 cycles/day. Other peaks can be seen, but at a much lower power.

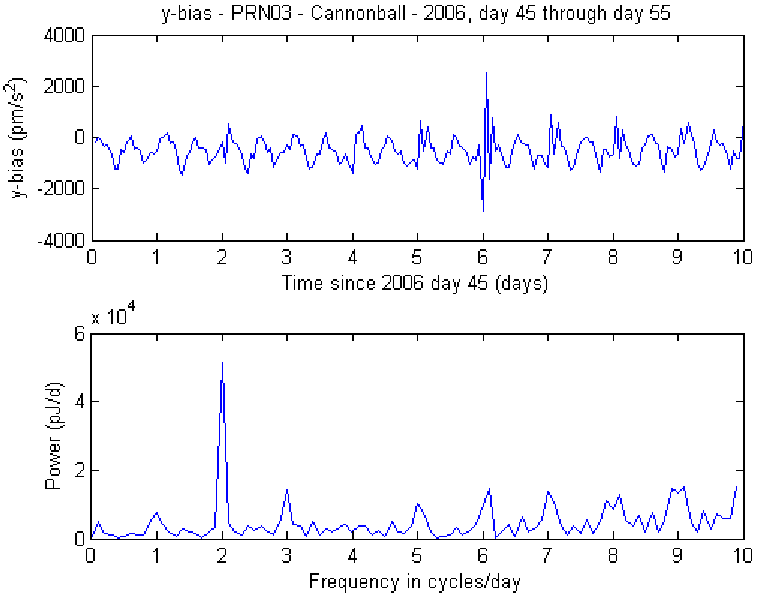

Figure 6.17. y-bias time series and power spectrum for PRN 03 using the Cannonball model

To illustrate the influence of the SRP model on the estimated y-bias parameter, and thus on its frequencies, similar cases were run using the other SRP models available. Note that PRN 03 is a Block IIA satellite, so we cannot use the UCL model. In Figure 6.18, we can see that the main frequency peak also occurs at 2 cycles/day when using the other models, and other peaks are visible. Examining a different time period for the same satellite confirms the previous case. The power spectra for the second interval of time for PRN 03 can be found in Figure 6.19. Similar experiments were conducted using a different satellite: PRN 25. The corresponding power spectra computed for two different intervals of time of ten consecutive days using the four different SRP models can be found in Figure 6.20 and Figure 6.21. Again, the 2 cycles/day frequency seems to dominate the spectrum.

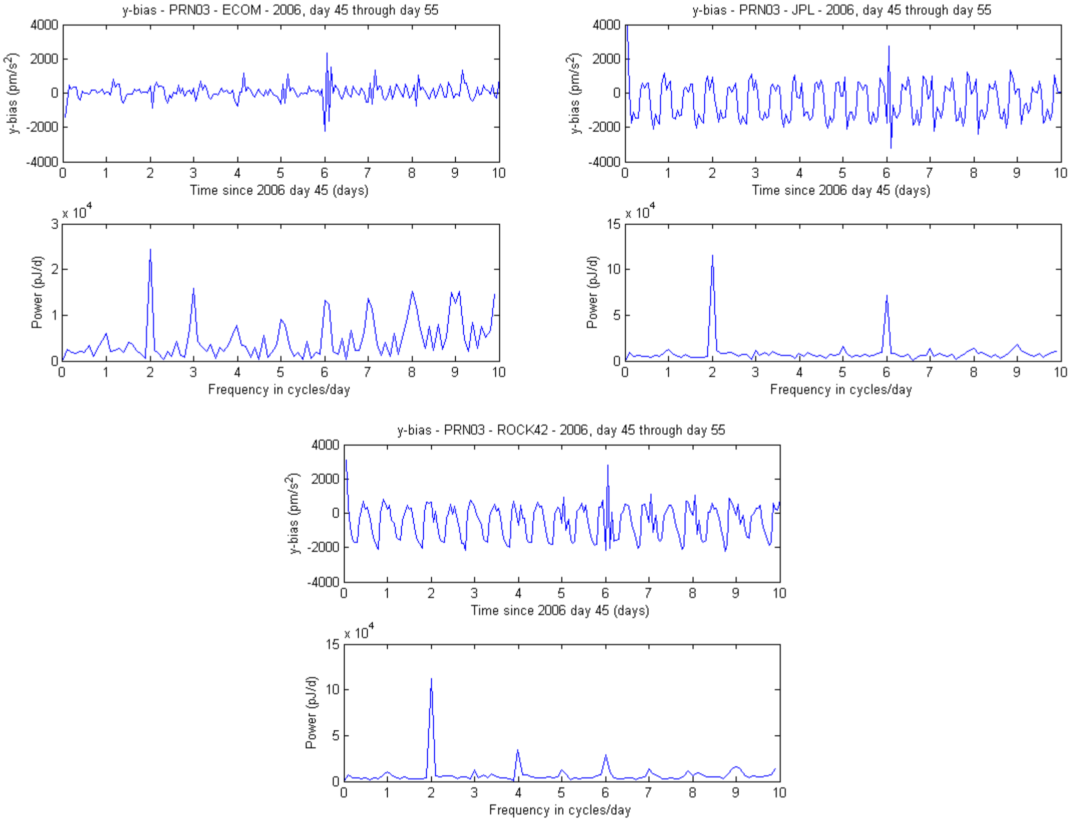

Figure 6.18. y-bias time series and power spectra - PRN 03 - first interval

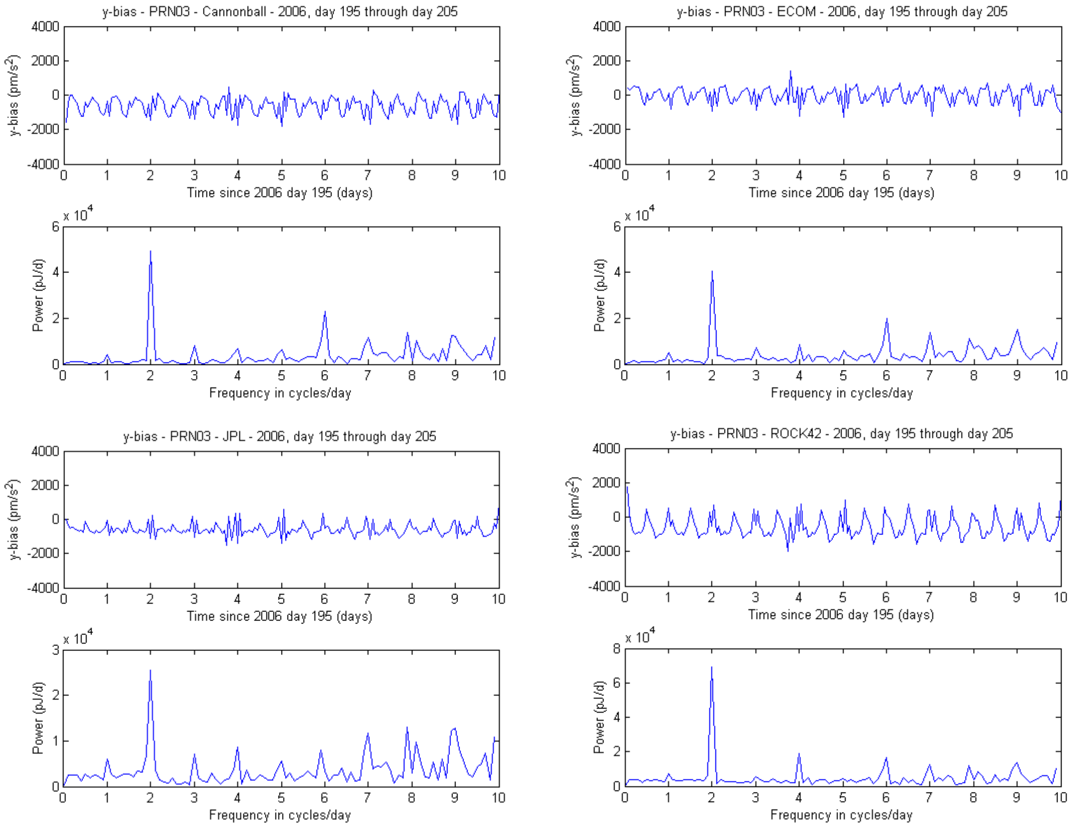

Figure 6.19. y-bias time series and power spectra - PRN 03 - second interval

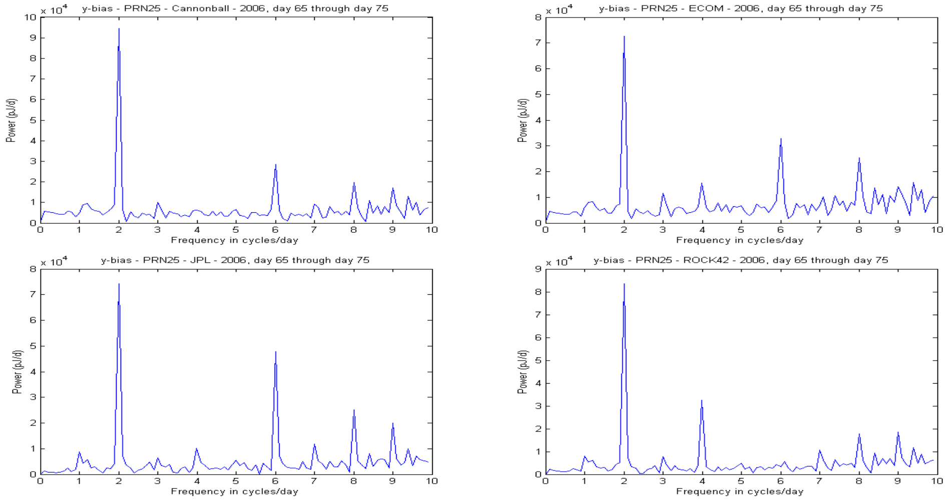

Figure 6.20. y-bias power spectra - PRN 25 - first interval

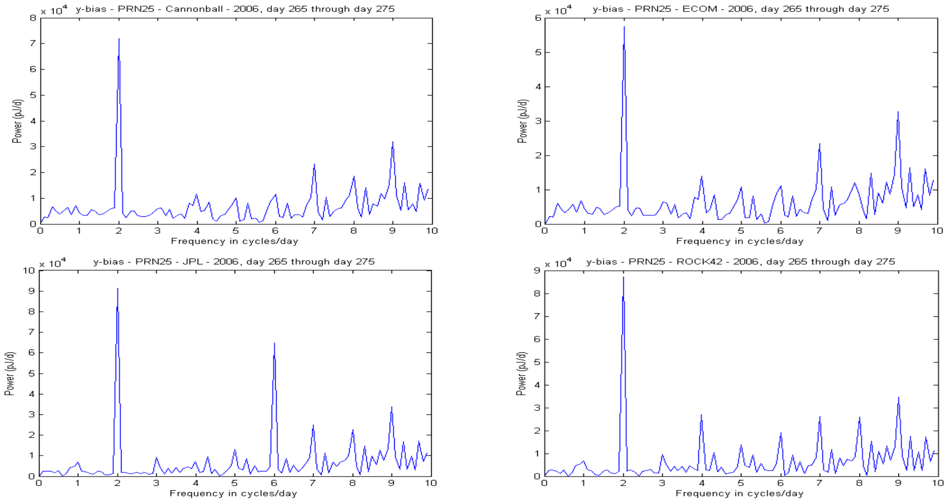

Figure 6.21. y-bias power spectra - PRN 25 - second interval

Similar power spectrum for two intervals of ten days for PRN 11 can be seen on Figure 6.22 and Figure 6.23. For most cases, a clear strong peak at 2 cycles/day is noticeable. However, the Cannonball case and the UCL case in Figure 6.23 do not show a main frequency at 2 cycles/day, but at 8 and 9 cycles/day as well as several other frequencies.

Concerning PRN 21, the cases using the JPL and ROCK42 SRP model show a main frequency at 2 cycles/day in the two intervals used. In the other cases, the power spectra are very noisy. For instance, the ECOM case in Figure 6.25 shows frequencies at 4, 6 and 9 cycles/day with smaller peaks at 2, 3, 7 and 8 cycles/day. In other words, it is hard to distinguish the main frequency. The power spectra for PRN 21 are presented in Figure 6.24 and Figure 6.25.

Another Block IIR satellite, PRN 13, is shown in Figure 6.26 and Figure 6.27. In most cases, the main frequency at 2 cycles/day is visible, although the Cannonball case shows a strong peak at 4 cycles/day, as well as the UCL case during the second time period. In Figure 6.28 and Figure 6.29, PRN 14 shows somewhat similar power spectra as PRN 13 with a strong peak at 2 cycles/day in most cases. The Cannonball case shows a strong peak at 4 cycles/day, as well as the ECOM case in the second time period. We also notice that the UCL case shows a strong peak at 8 cycles/day.

In summary, in the previous experiments, the two Block IIAs, PRN 03 and PRN 25, show a clear main frequency at 2 cycles/day. For the Block IIRs, the frequencies are more distributed depending on the case. However, the most consistent frequency generally remains at 2 cycles/day. It is worth noting that some cases show peaks at almost every frequency suggesting that the estimated y-bias time series contains significant noise, which may limit the interpretation of the results.

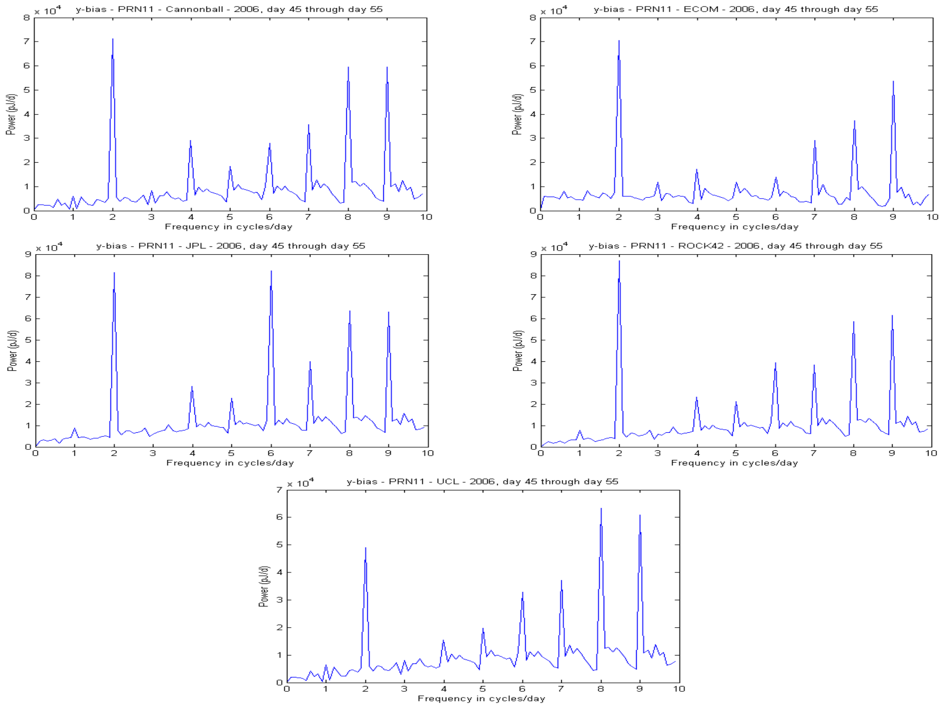

Figure 6.22. y-bias power spectra - PRN 11 - first interval

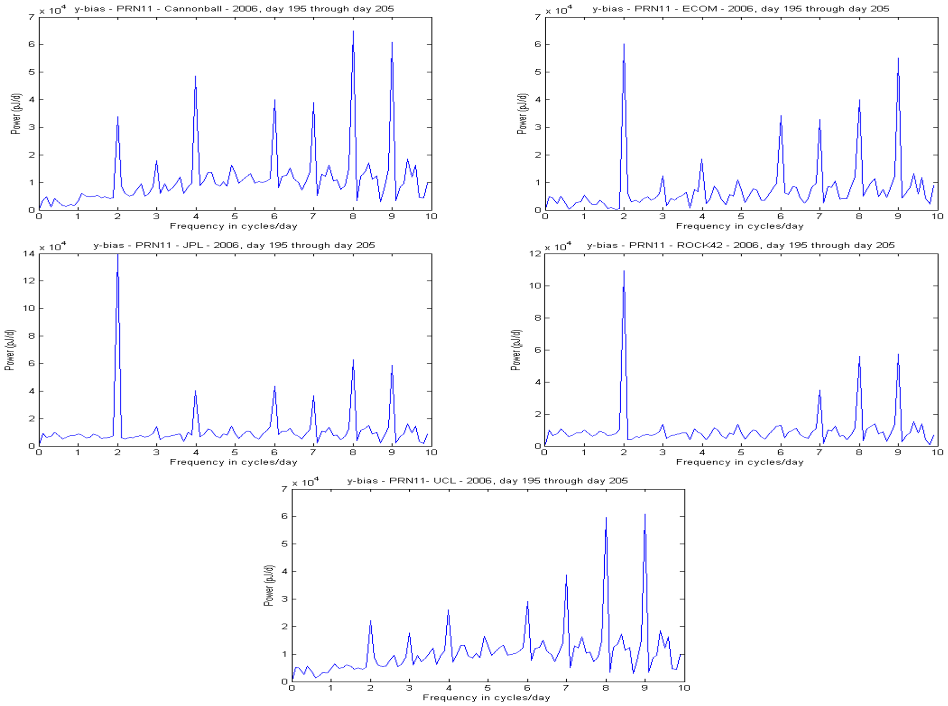

Figure 6.23. y-bias power spectra - PRN 11 - second interval

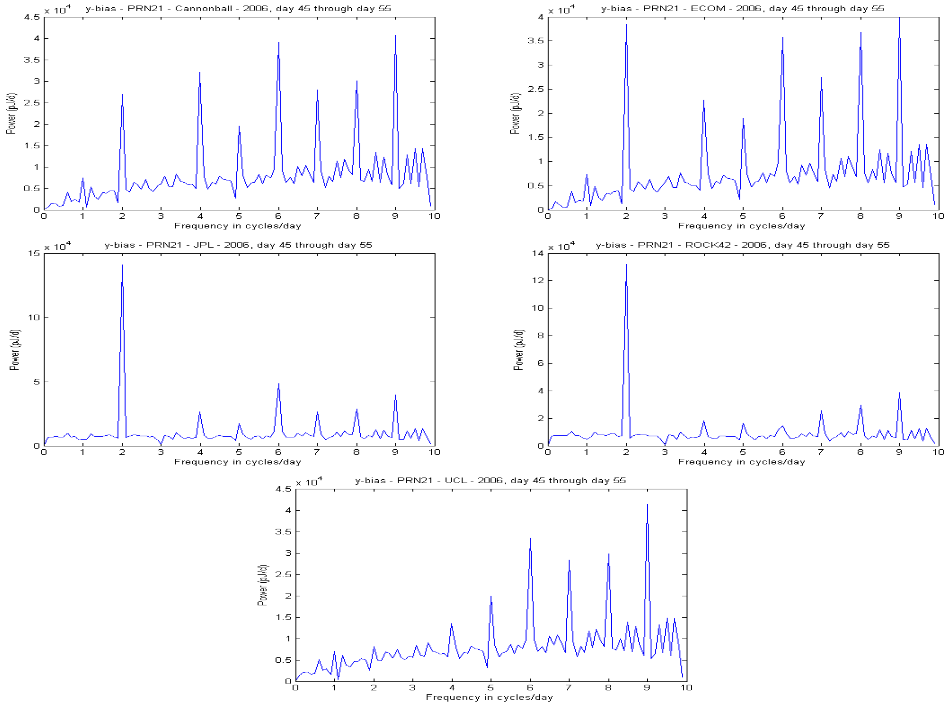

Figure 6.24. y-bias power spectra - PRN 21 - first interval

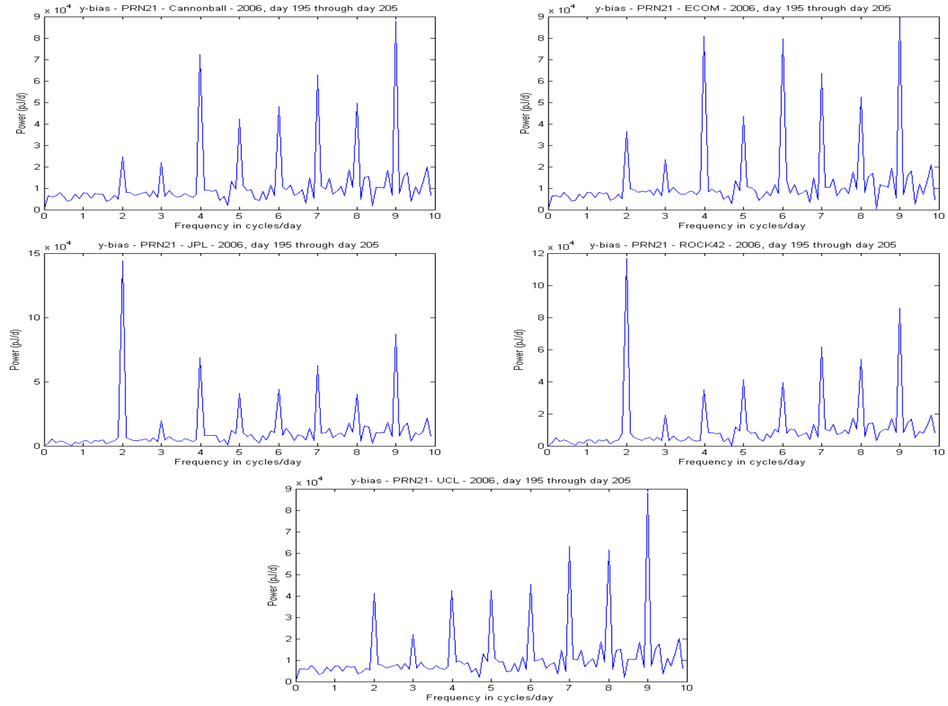

Figure 6.25. y-bias power spectra - PRN 21 - second interval

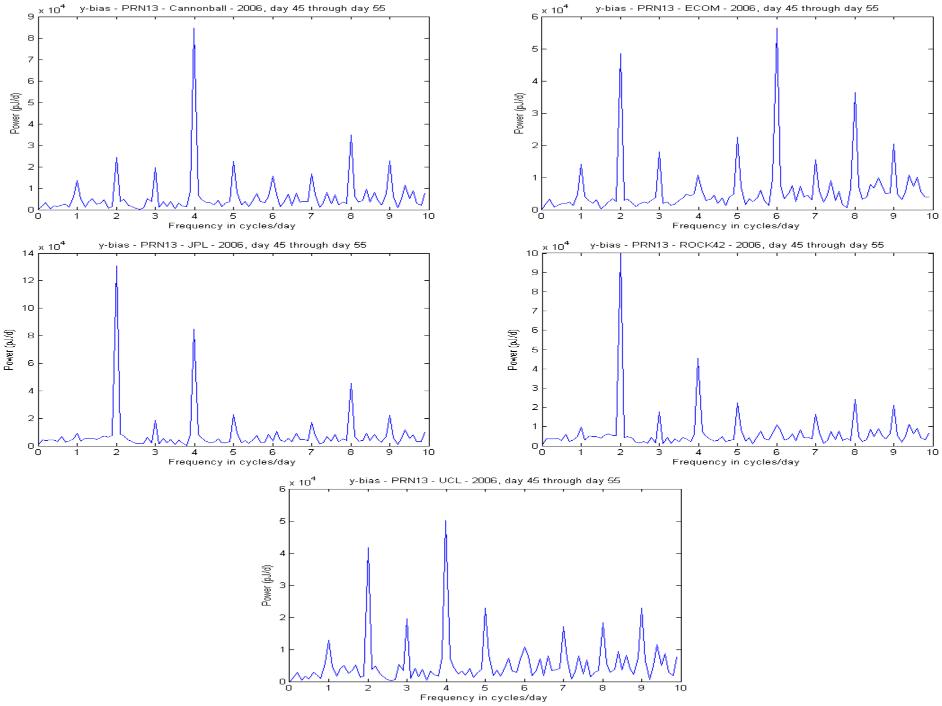

Figure 6.26. y-bias power spectra - PRN 13 - first interval

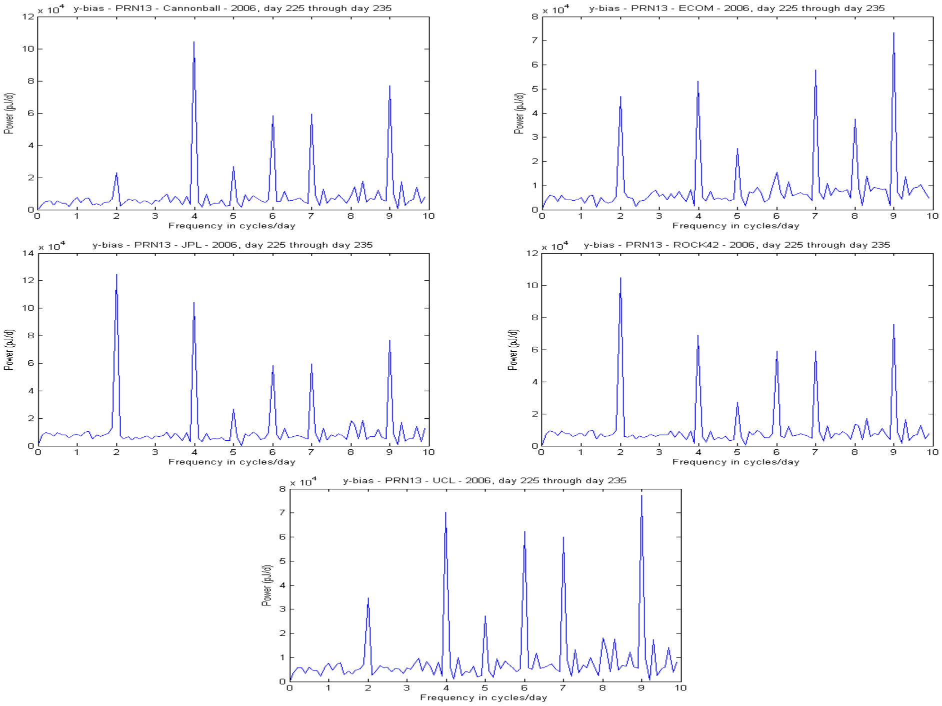

Figure 6.27. y-bias power spectra - PRN 13 - second interval

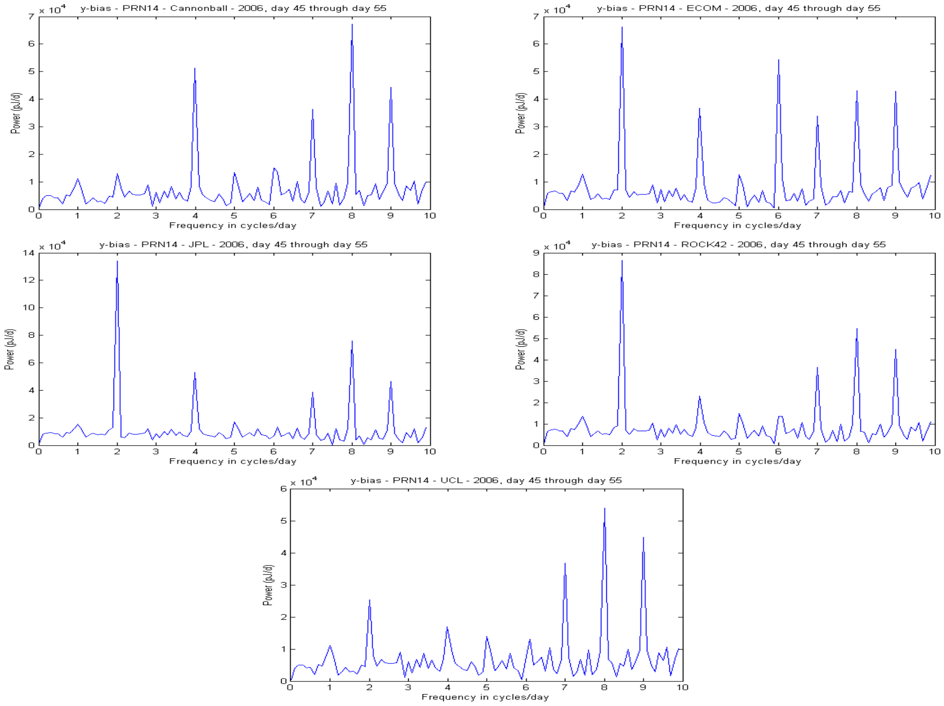

Figure 6.28. y-bias power spectra - PRN 14 - first interval

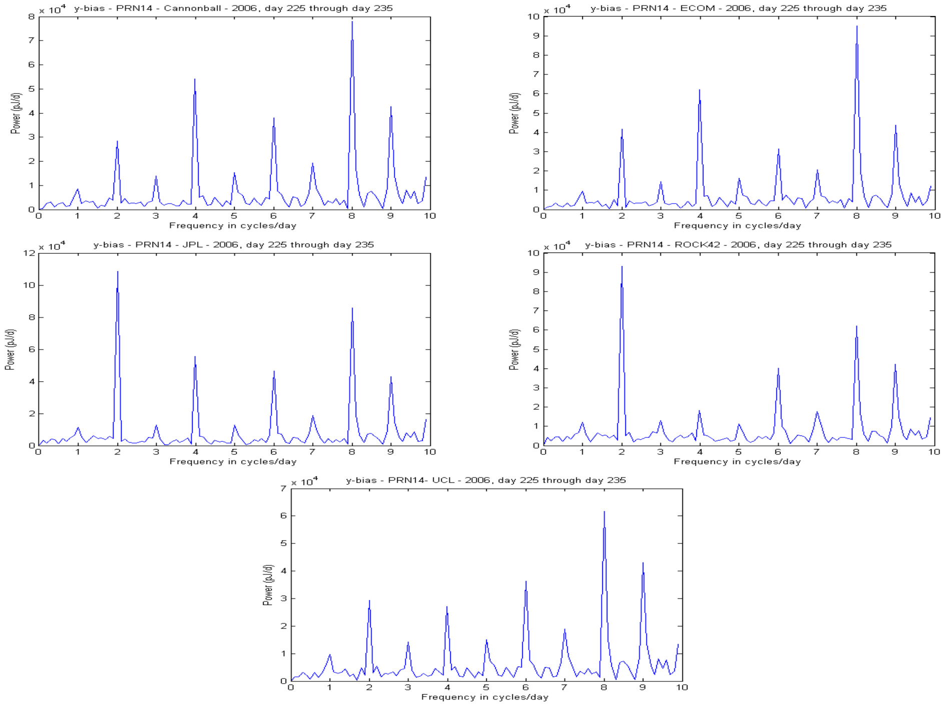

Figure 6.29. y-bias power spectra - PRN 14 - second interval

6.3.2 Y-bias evolution

In the following experiments, we take a closer look at the general characteristics of the estimated y-bias parameter time series. We computed the evolution of the y-bias parameter over the entire year 2006 for different satellites using different SRP models. In all the following cases, we performed orbit fits using the IGS ephemerides as our observations, similar to the previous cases described in this chapter. The position and velocity were estimated once per day. We found in Section 6.3.1 that the y-bias parameter seems to have a 2 cycles/day effect, thus we estimated the y-bias parameter twice per day in the next set of experiments. In addition, an SRP parameter was estimated four times a day since its main frequency was found to be 4 cycles/day [Froideval, 2004].

In the first case, we examined a Block IIR satellite, PRN 13. We estimated five different y-bias time series using the five SRP models available. Evolution of the y-bias parameter can be seen in Figure 6.30. To check the quality of the fits, the daily RMS's were calculated and displayed in Figure 6.31. Days corresponding to maneuvres, day 145 and 146, showed very high RMS's and were removed. By looking at Figure 6.30, we notice that the y-bias evolution depends on the SRP model used. However, we observed similarities among the analytical models: the UCL, the ROCK42 and the Cannonball model. This makes sense since all three analytical models are based on the same theoretical equations. The two empirical models behave differently. Similarities can also be seen in the RMS evolution in Figure 6.31. These observations are confirmed by looking at a different Block IIR satellite: PRN 14. Figure 6.32 shows the estimated y-bias time series for PRN 14. The dependency on the SRP model used can be seen in Figure 6.32 and the similarities among analytical models is evident. It is interesting to note that the evolution of the RMS when using the JPL model exhibits changes of behavior around day 120 and day 210. These changes correspond to eclipse seasons. Figure 6.33 shows the percentage of time spent in the Earth's shadow in this particular case. This change in behavior is consistent with the hybrid nature of the model as described in Section 4.5.4.

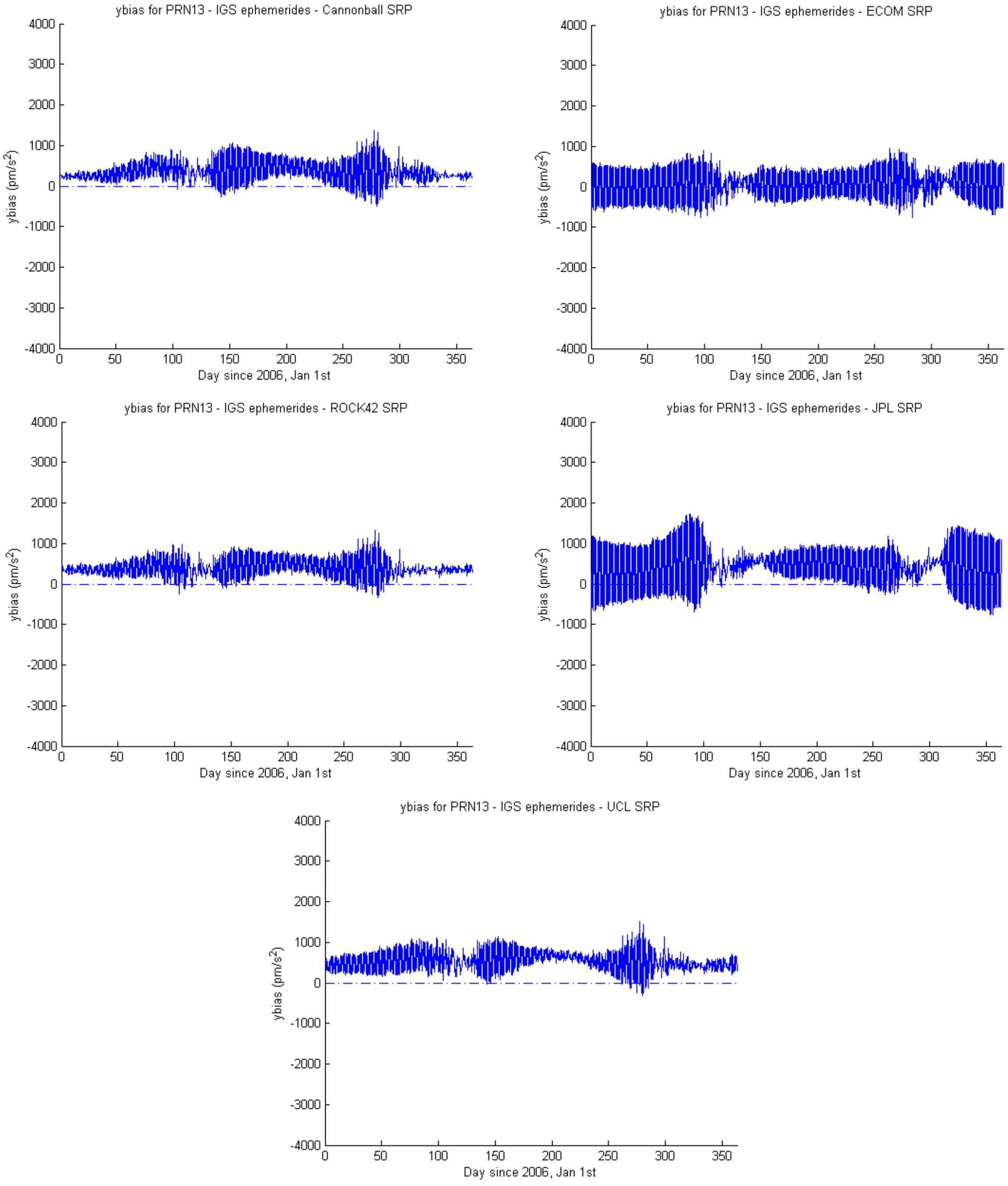

Figure 6.30. y-bias - PRN 13

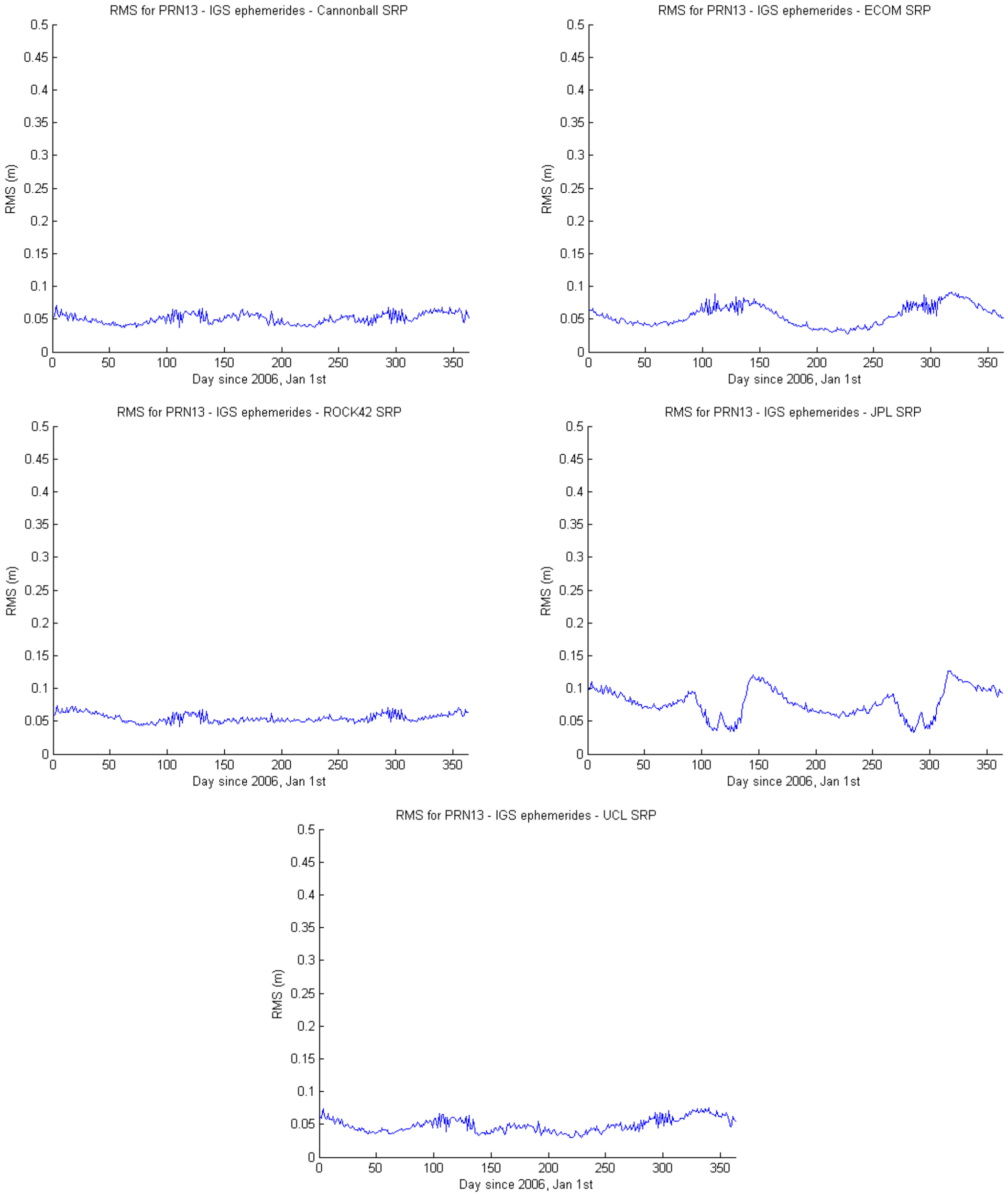

Figure 6.31. RMS - PRN 13

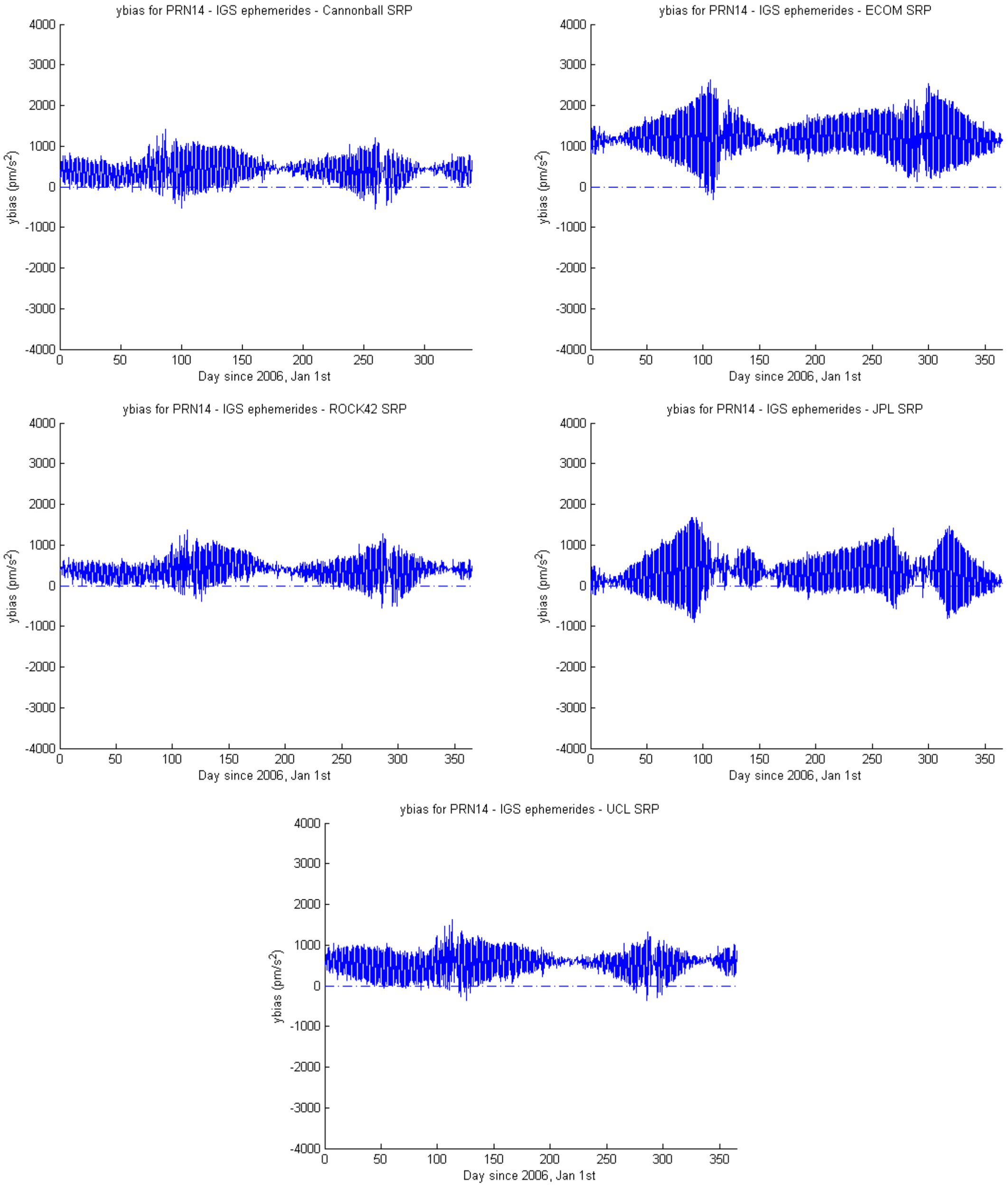

Figure 6.32. y-bias - PRN 14

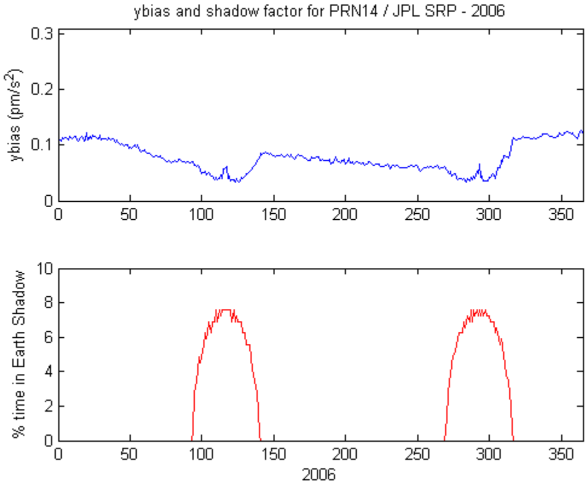

Figure 6.33. y-bias - PRN 14

The orbital plane seems to be another factor that influences the estimated y-bias time series. PRN 13 and PRN 14 are both located in plane F. We compared them to PRN 11 and PRN 21, two satellites located in a different plane, plane D. We obtained similar y-bias time series for satellites in the same plane. Figure 6.34 shows the y-bias evolution for the four different satellites using the Cannonball model. Satellites in plane F, on the left hand side of Figure 6.34, show a higher average value than the one in plane D, on the right hand side. We also note some similarities in the patterns among satellites in the same plane. Cases using the UCL, the ROCK42 and the JPL model lead to the same observations. The JPL case is shown in Figure 6.35. The ECOM case in Figure 6.36 shows different time series for PRN 13 and PRN 14, although we note similarities between PRN 11 and PRN 21. Since the ECOM model is an empirical model, it is possible that the ECOM model is absorbing other orbital effects. We can observe in most cases similarities in the evolution of the y-bias for satellites in the same plane. This suggests that the orientation of the orbital plane influence the evolution of the y-bias parameter.

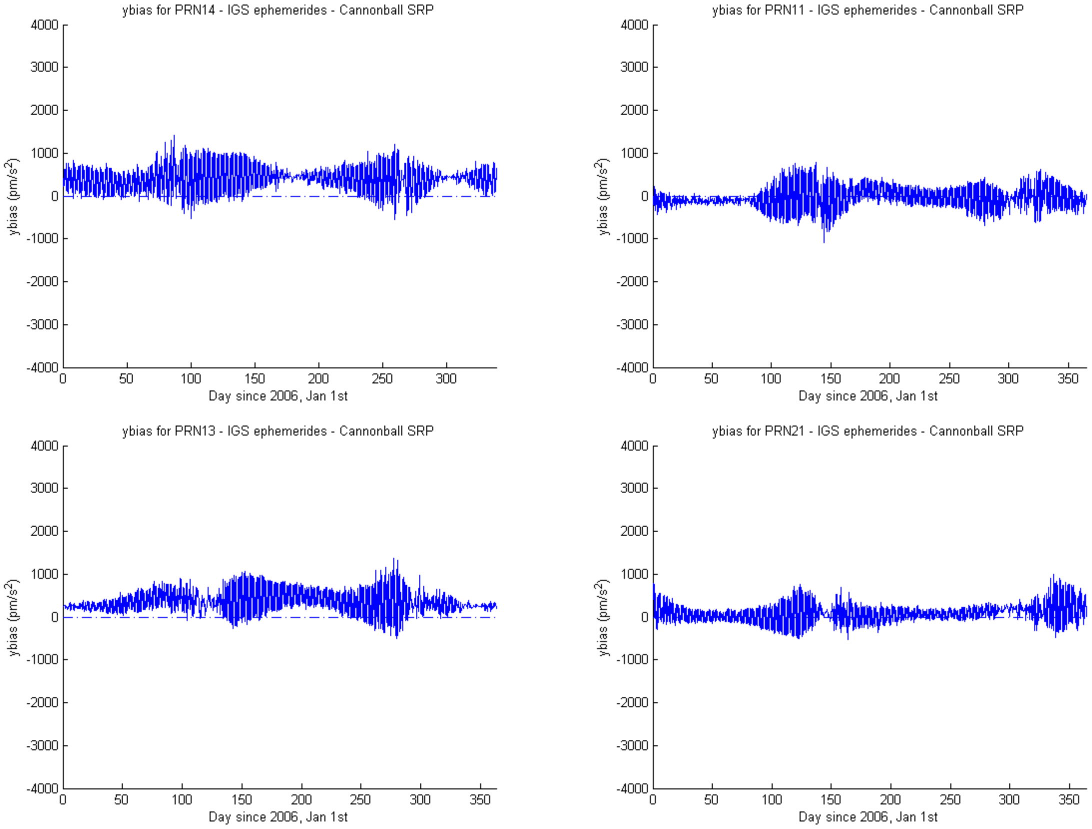
ybias for PRN14 - IGS ephemerides - Cannonball SRP

ybias for PRN11 - IGS ephemerides - Cannonball SRP

ybias for PRN13 - IGS ephemerides - Cannonball SRP

ybias for PRN21 - IGS ephemerides - Cannonball SRP

Figure 6.34. y-bias comparison - PRN 13, PRN 14, PRN 11 and PRN 21 - Cannonball

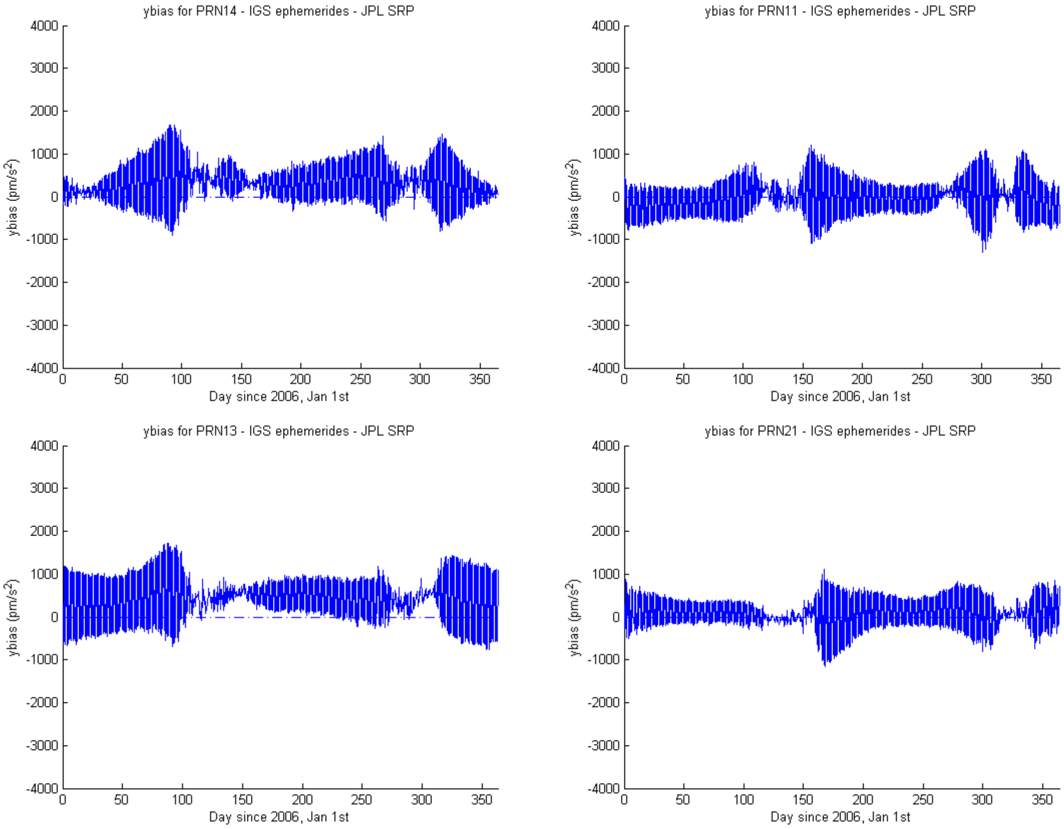

Figure 6.35. y-bias comparison - PRN 13, PRN 14, PRN 11 and PRN 21 - JPL

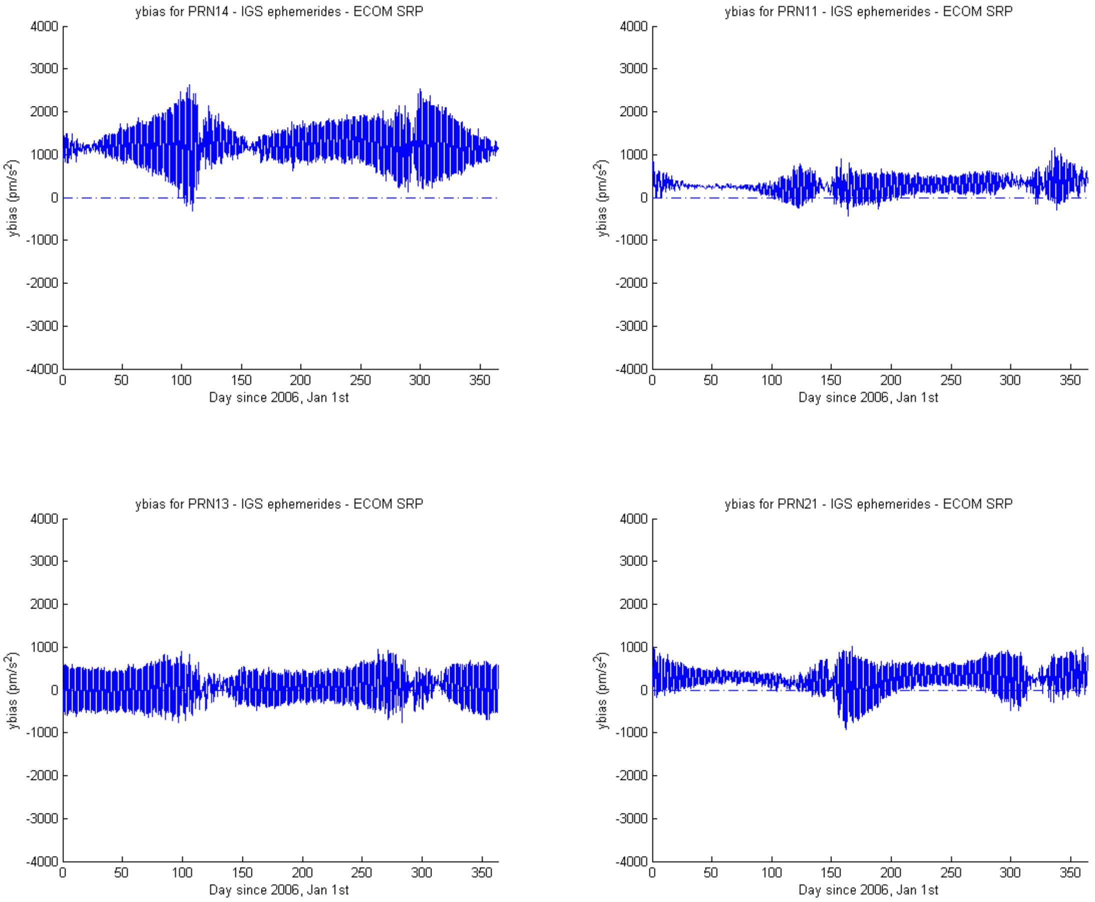

Figure 6.36. y-bias comparison - PRN 13, PRN 14, PRN 11 and PRN 21 - ECOM

We estimated the y-bias time series for two Block IIA satellites: PRN 03 and PRN 25. Figure 6.37 and Figure 6.38 show the y-bias time series for PRN 03 and PRN 25, respectively. The y-bias parameter is negative on average except for the case of PRN 03 using the ECOM model where the y-bias stays close to 0. In the previous cases, using Block IIR satellites, the average y-bias parameter value was positive or close to 0. The satellite Block seems to have an influence on the estimated y-bias time series.

Finally, one experiment suggests that the attitude of the satellite also plays a role in the y-bias evolution. Indeed, we examined a longer period of time of approximately 13 years, using PRN 25 with the Cannonball model. Daily orbit fits were performed since January 2, 1994. Initial position and velocity were estimated every day. The y-bias parameter was estimated twice per day and the Cannonball scale factor was estimated four times per day. The estimated y-bias is shown in Figure 6.39. We can see the effect of the different eclipse seasons where the amplitude becomes bigger. It is worth noting that a change in pattern indicated by a vertical dashed line is apparent. This change corresponds to the change in attitude suggested by Bar-Sever [1996b] and implemented on November 1995 for Block IIA satellites. The example shows that a change in the satellite attitude affects the estimated y-bias parameter.

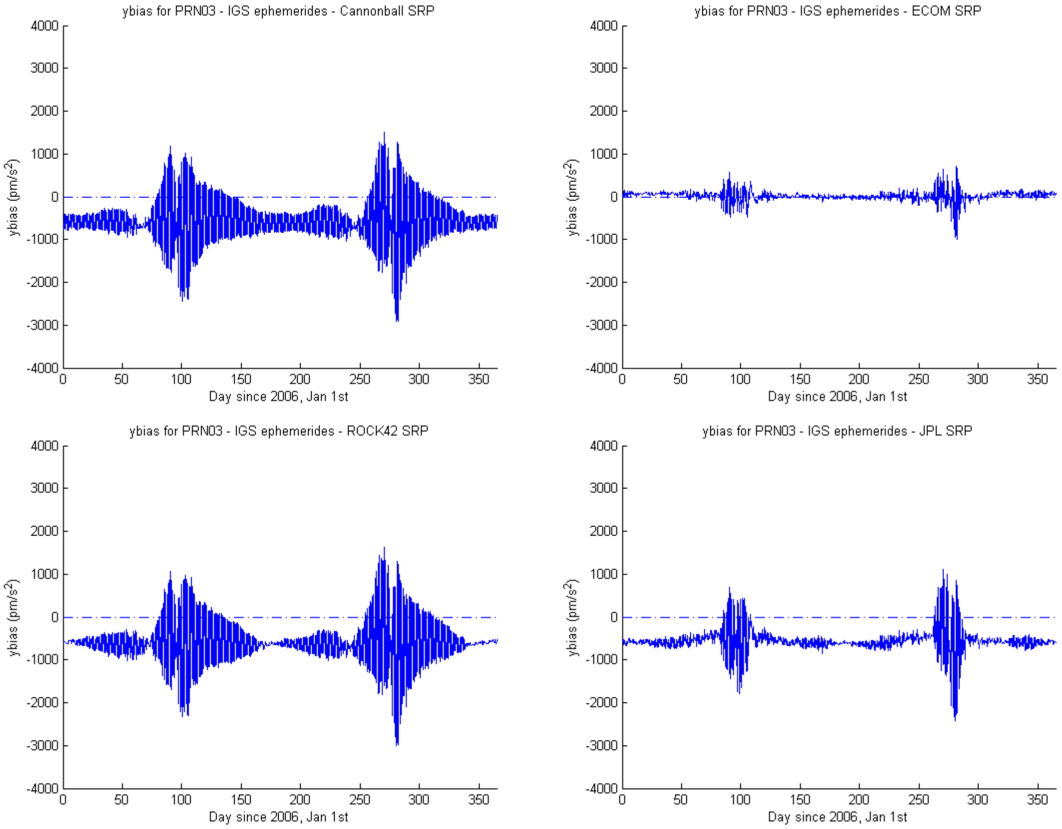

ybias for PRN03 - IGS ephemerides - Cannonball SRP

ybias for PRN03 - IGS ephemerides - ECOM SRP

ybias for PRN03 - IGS ephemerides - ROCK42 SRP

ybias for PRN03 - IGS ephemerides - JPL SRP

Figure 6.37. y-bias – PRN 03

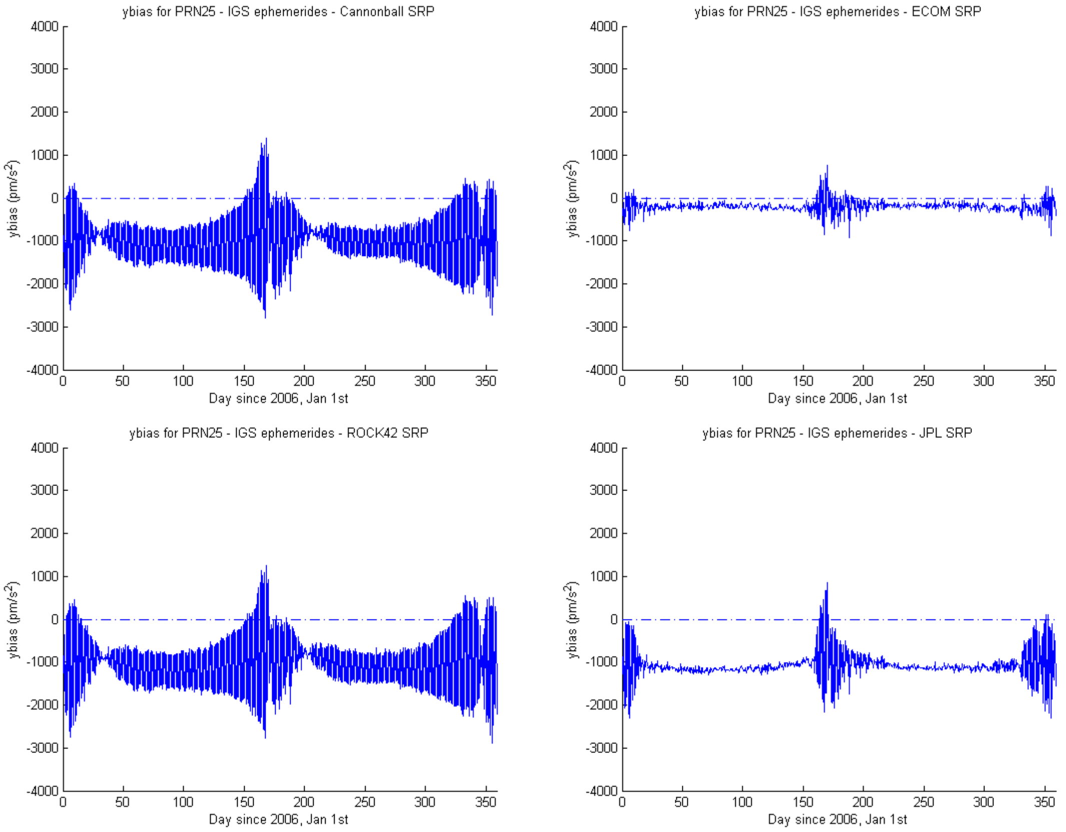

Figure 6.38. y-bias - PRN 25

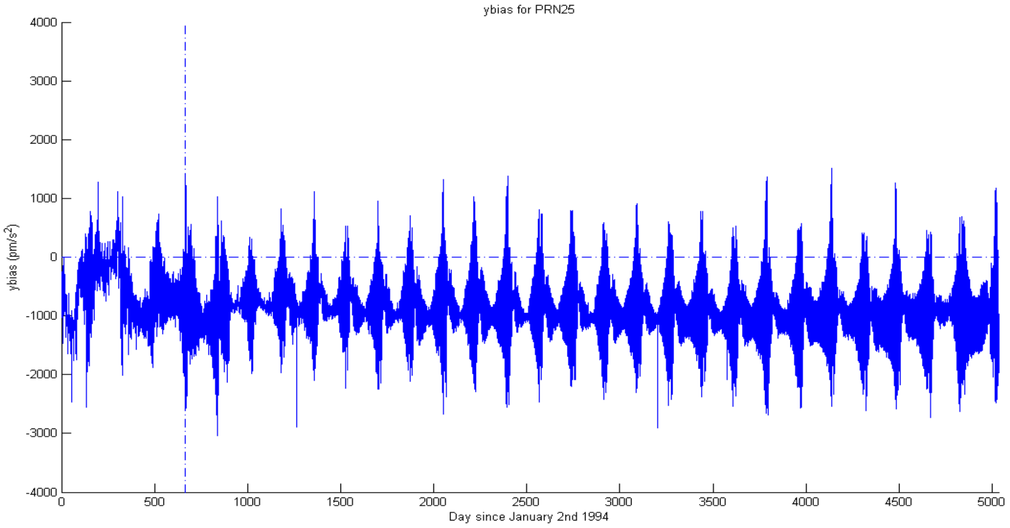

Figure 6.39. y-bias - PRN 25 - Cannonball SRP - change in attitude

Chapter 7

Conclusion

7.1 SUMMARY

Forces acting on GPS satellites can be categorized into gravitational and non-gravitational forces. Although gravitational forces are well modeled, non-gravitational forces are not fully understood and their mathematical models are incomplete. In this study, we focused on some non-gravitational forces. More precisely, at the altitude of GPS satellites, Solar Radiation Pressure represents the dominant non-gravitational force, but smaller forces are known to exist, such as the y-bias force and Earth Radiation Pressure (not considered in this study).

Solar Radiation Pressure (SRP) was described in Chapter 2. In Chapter 4, gravitational and non-gravitational forces were presented. A more detailed description was provided for five SRP models: the Cannonball model, the ECOM model, the early JPL model, the ROCK42 model and the UCL model. The recently developed UCL model [Ziebart, 2004] was implemented in MSODP for the purpose of this study.

In our approach, we considered the precise ephemerides provided by the IGS to be an accurate representation of the true orbit. The IGS, through the Analysis Centers and the Analysis Center Coordinator, combines the products generated by its different Analysis Centers. The final combination is believed to have errors under 5 cm [IGS, 2008c]. As described in Chapter 1, every Analysis Center models non-gravitational forces independently. To ensure the characteristics of the estimated orbits obtained in this study using the combined ephemerides are not dominated by any particular Analysis Center, we compared the IGS combination to the ephemerides generated by two independent centers: the JPL and the ESA center. We showed in Chapter 5 that the choice of ephemerides source does not significantly influence our results.

In Chapter 6, we studied different methodologies to handle non-gravitational parameters during an orbit prediction. An example of a direct method consists in taking the average of the estimated parameters values over one particular day and using it in the predicted orbit. On first approximation, this method leads to reasonable results. A more meaningful way is to approximate the estimated parameters time series by keeping only the most important frequencies. However, the best way is to assume that the evolutions of the parameters will be the same as the previously estimated time series. This method was used to generate the predicted orbits in the rest of the study.

The different SRP models were used in the dynamical model and we compared their performance in representing the precise ephemerides from IGS both in fitting GPS ephemerides as well as in predictions. In the first experiments, we estimated an SRP scale parameter for each model. However, in the following experiments, the SRP parameters were given a constant value to prevent them from absorbing effects not taken into account by the models. The comparison of the SRP models showed that both the UCL and the ECOM models lead to the lowest RMS of fit to the IGS daily ephemerides. Older models like the ROCK42 model presented the highest RMS of fit. The results were confirmed by examining orbit predictions in which the parameters were computed by applying the method described in the previous paragraph. SLR residuals offered an independent confirmation of the previous approach. Indeed, the residuals obtained were in agreement with the respective RMS's computed from orbit fits to the IGS ephemerides.

The last part of Chapter 6 was dedicated to the study of the y-bias force. We found that it has a main frequency of 2 cycles/day, that is to say it has a dominant once per revolution effect. In addition, we found that the y-bias time series depends on the SRP model used. Note that similar results were found among the different analytical models. The y-bias force is also dependent on the satellite Block type, which suggests that it depends on the geometry and structural properties of the satellite. Moreover, the y-bias force was found to be dependent on the plane where the satellite is located. This could mean that it depends on the orientation of the plane toward the Sun. Lastly, the y-bias was shown to be influenced by the attitude of the satellite.

7.2 DISCUSSION

By comparing the different SRP models, we show that a purely analytical model such as the UCL model leads to results that are comparable to a purely empirical model like the ECOM model. This is significant since analytical models provide a physical meaning whereas empirical models rely on observed data. In other words, empirical models can absorb errors caused by other effects. In principle, this makes analytical models better suited to separate SRP from other forces. Another advantage is that analytical models do not require empirical data and are thus useful for newly launched satellites.

Observations of the y-bias force show that it can be modeled as a once per revolution effect. The fact that it varies depending on the orbital plane implies that the orientation toward the Sun is important. This suggests that the y-bias force is related to SRP or other Sun-related effect.

7.3 FUTURE WORK

In this study, approximations were made by applying models previously derived for Block IIA satellites to Block IIR satellites. For better accuracy, updates for these models should be taken into account. For instance, the recently developed JPL model could be implemented into MSODP. In addition, coefficients for the ECOM model obtained for Block IIR satellites as well as improved coefficients for Block IIA satellites could be used in the future [Dach et al., 2007].

Improvements in analytical modeling are very promising. However, other aspects of SRP modeling could be refined such as the transition from pure sunlight to shadow. The conical model for eclipses can be improved to include secondary effects. For example, Adhya et al. [2004] show how the flattening of the Earth could be incorporated. Vokrouhlický et al. [1993] describe the refraction of the sunlight by the atmosphere of the Earth which in turn causes the visible Sun's disk to be flattened. Finally, it would be advantageous to look at SRP for future similar satellites like the GPS Block III or the future Galileo system.

Appendix A:

Solar Radiation Pressure models and estimated parameters used by the Analysis Centers

Organization	Effective date	A priori	Estimated Parameters
MIT Massachusetts Institute of Technology	2006-Nov	CODE	9 radiation pressure terms
	2004-Jan	CODE	9 radiation pressure terms
CODE Center for orbit determination in Europe	2008-Apr	CODE (2007)	5 parameters for solar radiation pressure modeling, i.e. constants in D-, Y- and X-direction and periodic terms in X-direction
	2002-Mar	ROCK	same as above
	1998-Mar	ROCK	same as above
	1996-Jun	ROCK	solar radiation scale factor and y-bias estimated as constants for one arc
EMR Natural Resources Canada	2008-Aug	JPL	solar radiation pressure scale in direct direction; stochastic and x/z solar scale
	2001-Nov	JPL (1997)	x,z, scale
	1996-Jun	ROCK	solar pressure scales in x and z
ESA Euopean Space Agency	2008-Jan	none	constants in D-, Y- and X-direction, periodic terms in X-direction (param. from CODE), small along-track accel, A0, Acos(u), Asin(u)
	2002-May*	ROCK	solar radiation pressure scale factor
	1999-May	ROCK	solar radiation pressure scale factor

GFZ GeoForschungsZentrum Potsdam	06-May-2007 (prep date: Jan 7, 2009)**	none	5 parameters for solar radiation pressure modeling, i.e. constants in D-, Y- and X-direction and periodic terms in X-direction (CODE)
	06-May-2007 (prep date: Sept 4, 2008)**	JPL (98)	solar radiation pressure scale
	1999-Aug	ROCK	solar radiation pressure scale
JPL Jet Propulsion Laboratory	2008-Nov	JPL (2004)	xz-scale, y-bias, and 3 stochastics
	2004-Apr*	II/IIA: JPL IIR: Lockheed-Martin	direct xz-scale, y-bias, and 3 stochastics
	25-Jan-2002*	Same as above	solar radiation pressure scale stochastically varying
	11-Jan-2002*	ROCK	same as above
	2000-Jun*	ROCK	same as above
	1999-Aug*	ROCK	same as above
JPL Jet Propulsion Laboratory	1998-Mar*	ROCK	same as above
	1998-Feb*	ROCK	same as above
	1997-Dec*	ROCK	same as above
	1995-Jan	ROCK	same as above
NOAA/NGS National Oceanic & Atmospheric Administration National Geodetic Survey	2006-Nov	CODE (2007)	scale parameters
	2004-Feb	CODE	scale parameters relative to CODE
	2001-Jun	ROCK	solar radiation pressure scales and once-per-revolution perturbation terms along the satellites - sun, body centered Y, and orthogonal third directions estimated as constant offsets for each one-day arc
	1998-Jul	ROCK	same as above
	1996-Jun	ROCK	solar radiation pressure scales in x and y estimated as constant offsets for each one-day arc
SOPAC Scripps Orbit and Permanent Array Center	2005-Apr	CODE	9 radiation-pressure terms

Solar Radiation Pressure models and estimated parameters
used by the Analysis Centers [IGS, 2008b]

Appendix B:
CODE Analysis Strategy Summary

```
=============================================================================

                         INTERNATIONAL GNSS SERVICE

                       CODE Analysis Strategy Summary

=============================================================================
Analysis Center   | Center for Orbit Determination in Europe (CODE)
                  | Astronomical Institute
                  | University of Bern
                  | Sidlerstrasse 5
                  | CH-3012 Bern
                  | Switzerland
                  | E-mail:       code (at) aiub.unibe.ch (CODE AC Team)
                  | Phone:        +41-31-631-8591
                  | Fax:          +41-31-631-3869
                  | Data archive: ftp://ftp.unibe.ch/aiub/CODE/
                  |               http://www.aiub.unibe.ch/download/CODE/
                  | Web:          http://www.aiub.unibe.ch    (CODE at AIUB)
                  |               http://www.bernese.unibe.ch (Bernese SW)
-----------------------------------------------------------------------------
Contact People    | Dr. Stefan Schaer
                  |   E-mail: stefan.schaer (at) aiub.unibe.ch
                  |   Phone:  +41-31-631-8592 (8591)
                  | Dr. Rolf Dach
                  |   E-mail: rolf.dach (at) aiub.unibe.ch
                  |   Phone:  +41-31-631-8593 (8591)
                  | Michael Meindl
                  |   E-mail: michael.meindl (at) aiub.unibe.ch
                  |   Phone:  +41-31-631-3802 (8591)
                  | Dr. Heike Bock
                  |   E-mail: heike.bock (at) aiub.unibe.ch
                  |   Phone:  +41-31-631-8602 (8591)
                  | Dr. Adrian Jaeggi
                  |   E-mail: adrian.jaeggi (at) aiub.unibe.ch
                  |   Phone:  +41-31-631-8592 (8591)
                  | Luca Ostini
                  |   E-mail: luca.ostini (at) aiub.unibe.ch
                  |   Phone:  +41-31-631-3802 (8591)
-----------------------------------------------------------------------------
Software Used     | Bernese GPS Software Version 5.1, developed at AIUB
-----------------------------------------------------------------------------
List of CODE's    | ftp://ftp.unibe.ch/aiub/BSWUSER50/TXT/AIUB_AFTP.README
analysis products |
http://www.aiub.unibe.ch/download/BSWUSER50/TXT/AIUB_AFTP.README
                  |
Final Products    | CODwwwwn.EPH    GNSS/GPS ephemeris/clock data in 7 daily
```

```
generated for     |                 files at 15-min intervals in SP3 format,
GPS week 'wwww'   |                 including accuracy codes computed from
day of week 'n'   |                 a long-arc analysis
(n=0,1,...,6)     | CODwwww7.ERP    GNSS ERP (pole, UT1-UTC) solution for 1
day of year 'ddd' |                 week in IGS IERS ERP format
year 'yy'         | CODwwww7.SUM    Analysis summary for 1 week
                  | CODwwww7.SNX    GNSS weekly station coordinates, SATAs,
                  |                 GCs, and daily sets of ERPs in SINEX
                  |                 format
                  | CODwwwwn.CLK    GPS satellite and receiver clock
                  |                 corrections at 30-sec intervals in clock
                  |                 RINEX format
                  | CODwwwwn.CLK_05S GPS satellite and receiver clock
                  |                 corrections at 5-sec intervals in clock
                  |                 RINEX format
                  | CODwwwwn.TRO    GNSS 2-hour troposphere delay estimates
                  |                 in troposphere SINEX format
                  | CODGddd0.yyI    GNSS 2-hour global ionosphere maps in
                  |                 IONEX format, including satellite and
                  |                 receiver P1-P2 code bias values
                  | CGIMddd0.yyN    GNSS daily Klobuchar-style ionospheric
                  |                 (alpha and beta) coefficients in RINEX
                  |                 format
                  | P1P2yymm.DCB    GNSS monthly P1-P2 code bias solutions
                  |                 in Bernese DCB format
                  | P1C1yymm.DCB/F  GPS monthly P1-C1 code bias solutions in
                  |                 Bernese DCB format and in a format
                  |                 specific to the CC2NONCC utility
                  |
                  | Remarks:
                  |
                  |   EPH: Orbit positions correspond to the estimates for
                  |        the middle day of a 3-day long-arc analysis.
                  |   ERP: ERP representation is continuous in time (over
                  |        1 week).
                  |   CLK: Clock corrections are consistent with carrier
                  |        phase as well as P1/P2 pseudorange measurements.
                  |        CODE P1-C1 pseudorange bias values of a moving
                  |        30-day solution are considered to correct C1/X2
                  |        and C1/P2 receiver data.
                  |   EPH/ERP/TRO: These products are based on weekly
                  |        coordinate results.
                  |
Rapid Products    | CODwwwwn.EPH_R  GNSS/GPS ephemeris/clock data in at
generated daily   |                 15-min intervals in SP3 format, including
                  |                 accuracy codes computed from a long-arc
                  |                 analysis
                  | CODwwwwn.ERP_R  GNSS ERP (pole, UT1-UTC) solution in IGS
                  |                 IERS ERP format
                  | CODwwwwn.CLK_R  GPS satellite and receiver clock
                  |                 corrections at 30-sec intervals in clock
                  |                 RINEX format
                  | CODwwwwn.TRO_R  GNSS 2-hour troposphere delay estimates
                  |                 in troposphere SINEX format
                  | CORGddd0.yyI    GNSS 2-hour global ionosphere maps in
                  |                 IONEX format, including satellite and
                  |                 receiver P1-P2 code bias values
                  | CGIMddd0.yyN_R  GNSS daily Klobuchar-style ionospheric
                  |                 (alpha and beta) coefficients in RINEX
```

```
                  |                 format
                  | CODwwwwd.SNX_R  GNSS daily station coordinates and set
                  |                 of 6-hourly ERPs in SINEX format (for
                  |                 IERS inter-technique combination)
                  |
                  | Remarks:
                  |
                  |   EPH: Orbit positions correspond to the estimates for
                  |        the last day of a 3-day long-arc analysis.
                  |   CLK: Clock corrections are consistent with carrier
                  |        phase as well as P1/P2 pseudorange measurements.
                  |        CODE P1-C1 pseudorange bias values of a moving
                  |        30-day solution are considered to correct C1/X2
                  |        and C1/P2 receiver data.
                  |
Ultra Rapid       | COD.EPH_U       GNSS ephemeris/broadcast clock data in at
Products updated  |                 15-min ntervals in SP3 format, including
every 6 hours     |                 accuracy codes computed from a long-arc
                  |                 analysis
                  | COD.ERP_U       GNSS ERP (pole, UT1-UTC) solution in IGS
                  |                 IERS ERP format
                  | COD.SUM_U       List of considered GNSS stations
                  | COD.TRO_U       GNSS 2-hour troposphere delay estimates
                  |                 in troposphere SINEX format
                  | COD.ION_U       GNSS 2-hour global ionosphere maps in
                  |                 Bernese ION format
                  |
                  | Remarks:
                  |
                  |   EPH: Orbit positions correspond to the estimates for
                  |        the last 24 hours of a 3-day long-arc analysis
                  |        plus predictions for the following 24 hours
                  |   EPH/ERP/TRO: Files contain generally results of last
                  |        update
                  |   ION: Last rapid ionosphere product complemented by all
                  |        available ionosphere predictions
                  |
Predictions       | CODwwwwn.EPH_Pi GNSS/GPS ephemeris/clock data at 15-min
updated every 6   |                 intervals in SP3 format, including
hours             |                 accuracy codes computed from a long-arc
                  |                 analysis
                  | CODwwwwn.ERP_Pi GNSS ERP (pole, UT1-UTC) solution in IGS
                  |                 IERS ERP format
                  | COPGddd0.yyI    GNSS 2-hour global ionosphere maps in
                  |                 IONEX format, including satellite P1-P2
                  |                 code bias values
                  | CGIMddd0.yyN_Pi GNSS daily Klobuchar-style ionospheric
                  |                 (alpha and beta) coefficients in RINEX
                  |                 format
                  | CODwwwwd.EPH_5D GNSS/GPS ephemeris/clock data at 15-min
                  |                 intervals in SP3 format
                  | CODwwwwd.ERP_5D GNSS ERP (pole, UT1-UTC) solution in IGS
                  |                 IERS ERP format
                  |
                  | Remarks:
                  |
                  |   "P2" indicates 2-day predictions (24-48 hours); "P"
                  |   indicates 1-day predictions (0-24 hours).
                  |   "5D" indicates files containing predicted information
```

```
                   |   for 5 days (0-120 hours).
                   |
Specialties in     | - CODE has been generating its products from a rigorous
CODE's analysis    |   combination of GPS and GLONASS observations. In this
                   |   way, best possible consistency of the orbit products is
                   |   guaranteed.
                   | - Uninterrupted POD for all transmitting GNSS satellites,
                   |   specifically for:
                   |   . brand new satellites
                   |   . satellites without any broadcast orbit information
                   |   . satellites marked unhealthy/unusable
                   |   . poorly observed (GLONASS) satellites
                   |   . (GPS) satellites being repositioned
                   | - Elevation mask angle of 3 degrees used.
                   | - Sophisticated ambiguity resolution scheme, already
                   |   including GLONASS ambiguity resolution for shortest
                   |   baselines.
                   | - Continuous parameterization, particularly for EOP,
                   |   troposphere ZPD and horizontal gradient parameters,
                   |   ionosphere parameters, allowing for connection of the
                   |   parameters at day boundaries.
                   | - IGS fiducial sites are automatically verified for
                   |   consistent datum definition. This is also true with
                   |   respect to all antenna-sharing fiducial sites.
                   | - Inclusion of fast moving South Pole station AMU2.
                   | - Inclusion of all available NGA stations.
                   | - Generation of high-rate (5-sec) clock products.
                   | - Generation of high-rate (1-hour) EOP results
                   |   (internally).
                   | - Setup of GNSS satellite antenna PCV parameters specific
                   |   to each individual GPS and GLONASS satellite;
                   |   corresponding patterns are not only available for the
                   |   ionosphere-free linear combination but also for the
                   |   geometry-free (L1-L2) linear combination.
                   | - A multi-GNSS-capable internal PCV file format is used;
                   |   receiver antenna PCV models specific to GLONASS
                   |   (or other) frequencies could be applied.
                   | - Monitoring of various differential code biases (DCBs),
                   |   specifically:
                   |   . GPS/GLONASS P1-P2 satellite and receiver DCBs
                   |   . GPS P1-C1 satellite DCBs
                   |   . biases crucial for GLONASS ambiguity resolution
                   | - Extensive monitoring of IGS data flow concerning:
                   |   . availability
                   |   . latency
                   |   . completeness
                   |   . consistency
                   | - Provision of GNSS geocenter coordinates in SINEX.
                   | - Production of GNSS rapid SINEX files containing station
                   |   coordinates and ERPs with a time resolution of 6 hours
                   |   is foreseen as a contribution for the IERS inter-
                   |   technique combination.
                   | - Regular GNSS orbit validation using SLR data; CODE
                   |   acts as an AAC of the ILRS.
                   | - The latest version of our steadily further developed
                   |   GNSS analysis SW is employed for operational analysis.
                   |
Computer platform  | Week 1477: UBELIX: Linux, x86_64
                   | Week 1065: UBECX: SunOS
```

```
                  |
Last changes      | Week 1477: See IGSREPORT.16225 and IGSMAIL.5771
                  | Week 1452: See IGSREPORT.15669/IGSREPORT.14622
                  | Week 1440: See IGSREPORT.15405
                  | Week 1439: See IGSREPORT.15403
                  | Week 1409: See IGSREPORT.14695
                  | Week 1406: See IGSREPORT.14622 and
IGSMAIL.5507/IGSMAIL.5518
                  | Week 1400: See IGSREPORT.14486 and IGSMAIL.5518
                  | Week 1367: See IGSREPORT.13669
                  | Week 1349: See IGSREPORT.13201
                  | Week 1328: See IGSREPORT.12706
                  | Week 1326: See IGSREPORT.12657
                  | Week 1321: See IGSREPORT.12569 and IGSMAIL.5151
                  | Week 1299: See IGSREPORT.12031
                  | Week 1282: See IGSREPORT.11617
                  | Week 1279: See IGSREPORT.11543
                  | Week 1255: See IGSMAIL.4913
                  | Week 1254: See IGSREPORT.10997 and IGLOSMAIL.963
                  | Week 1252: See IGSMAIL.4782
                  | Week 1242: See IGSREPORT.10752
                  | Week 1222: See IGSREPORT.10361 and
IGSMAIL.4474/IGLOSMAIL.770
                  | Week 1216: See IGSMAIL.4371/IGLOSMAIL.736
                  | Week 1191: See IGSREPORT.9756 and IGSMAIL.4162
                  | Week 1158: See IGSREPORT.9147 and IGSMAIL.3823
                  | Week 1143: See IGSREPORT.8868
                  | Week 1142: See IGSREPORT.8848
                  | Week 1135: See IGSREPORT.8710
                  | Week 1130: See IGSREPORT.8616
                  | Week 1128: See IGSREPORT.8577
                  | Week 1077: See IGSREPORT.7544
                  | Week 1065: See IGSREPORT.7279
                  | Week 1057: See IGSREPORT.7107 and IGSMAIL.2827
                  | Week 1021: See IGSREPORT.6351
                  | Week 0978: See IGSREPORT.5415 and IGSMAIL.2043
                  | Week 0947: See IGSREPORT.4698 and IGSMAIL.1829
                  | Week 0926: See IGSREPORT.4247 and IGSMAIL.1705
                  | Week 0873: See IGSREPORT.3056
-----------------------------------------------------------------------------
Preparation Date  | 18-Aug-1996
-----------------------------------------------------------------------------
Modification Dates| 13-Mar-1998
                  | 12-Mar-2002/SS: Major revision and update
                  | 13-Mar-2002/SS: JGM3 model up to degree 12
                  | 24-Oct-2002/SS: Typo concerning satellite antenna offset
                  |                 value corrected
                  | 28-May-2008/SS/RD: Major revision and update
-----------------------------------------------------------------------------
Effective Date for| 27-Apr-2008
Data Analysis     |
=============================================================================
```

```
-----------------------------------------------------------------------------
|                           MEASUREMENT MODELS                              |
|---------------------------------------------------------------------------|
| Preprocessing     | Phase preprocessing in a baseline by baseline mode    |
|                   | using triple-differences. In most cases, cycle slips  |
|                   | are fixed looking simultaneously at different linear  |
|                   | combinations of L1 and L2. If a cycle slip cannot be  |
|                   | fixed reliably, bad data points are removed or new    |
|                   | ambiguities are set up. In addition, a data screening |
|                   | step on the basis of weighted postfit residuals is    |
|                   | performed. Outliers are removed.                      |
|---------------------------------------------------------------------------|
| Basic Observable  | GPS/GLONASS carrier phase; code only used for receiver |
|                   | clock synchronization                                  |
|                   |-------------------------------------------------------|
|                   | Elevation angle cutoff :  3 degrees                   |
|                   | Sampling rate          :  3 minutes                   |
|                   | Weighting              :  6 mm for double-differenced |
|                   |                           ionosphere-free phase       |
|                   |                           observations at zenith;     |
|                   |                           elevation-dependent weighting |
|                   |                           function 1/cos(z)**2        |
|---------------------------------------------------------------------------|
| Modeled           | Double differences, ionosphere-free linear combination |
| observable        |                                                       |
|---------------------------------------------------------------------------|
| RHC phase         | Phase polarization effects applied (Wu et al., 1993)  |
| rotation corr.    |                                                       |
|---------------------------------------------------------------------------|
| Ground antenna    | IGS05 PCV model is applied. Receiver antenna PCV      |
| phase center      | models specific to GLONASS is applied (as soon as     |
| calibrations      | available).                                           |
|---------------------------------------------------------------------------|
| Troposphere       | A priori model  : Saastamoinen-based hydrostatic      |
|                   |                   (using GPT) mapped with the dry-GMF |
|                   |-------------------------------------------------------|
|                   | Met data input  : No real met measurements used (GPT) |
|                   |-------------------------------------------------------|
|                   | Estimation      : Zenith delay corrections are        |
|                   |                   estimated relying on the wet-GMF in |
|                   |                   intervals of 2 hours. N-S and E-W   |
|                   |                   horizontal delay parameters are     |
|                   |                   solved for every 24 hours. Details  |
|                   |                   about the gradient model can be     |
|                   |                   found in (Rothacher et al., 1997).  |
|                   |                   Refined gradient model used (see    |
|                   |                   IGSMAIL.5518).                      |
|                   |-------------------------------------------------------|
|                   | Constraints     : Both zenith and gradient parameters |
|                   |                   are treated as completely           |
|                   |                   unconstrained.                      |
|                   |-------------------------------------------------------|
|                   | Mapping function: GMF                                 |
|---------------------------------------------------------------------------|
| Ionosphere        | Not modeled (first-order effect eliminated by forming |
|                   | the ionosphere-free linear combination of L1 and L2). |
|                   | GNSS-derived global ionosphere map information is used |
|                   | to support ambiguity resolution when using the QIF    |
|                   | strategy.                                             |
```

```
|                   |                                                       |
|                   | Zero-difference data analysis for global ionosphere    |
|                   | mapping and for P1-P2 code bias retrieval:             |
|                   |                                                       |
|                   | The vertical total electron content (VTEC) is modeled  |
|                   | in a solar-geomagnetic reference frame using a         |
|                   | spherical harmonics expansion up to degree and         |
|                   | order 15. The time resolution considered for the VTEC  |
|                   | maps is 2 hours. Instrumental biases, so-called        |
|                   | differential code biases (DCB), for all GNSS           |
|                   | satellites and ground stations are estimated as        |
|                   | constant values for each day, simultaneously with the  |
|                   | 12 times 256, or 3072 parameters used to represent the |
|                   | global VTEC distribution. The DCB datum is defined by  |
|                   | a zero-mean condition imposed on the satellite bias    |
|                   | estimates. To convert line-of-sight TEC into vertical  |
|                   | TEC, a modified single-layer model mapping function    |
|                   | approximating the JPL extended slab model mapping      |
|                   | function is adopted. The mapping function is evaluated |
|                   | at geodetic satellite elevation angles. For the        |
|                   | computation of the ionospheric pierce points, a        |
|                   | spherical layer with a radius of 6821 km is assumed,   |
|                   | implying geocentric, not geodetic IONEX latitudes.     |
|                   | The geometry-free linear combination of one-way        |
|                   | carrier phase leveled to code is used as observable.   |
|                   |                                                       |
|                   | Elevation cutoff: 10 degrees                           |
|----------------------------------------------------------------------------|
| Plate motions     | IGS05 station velocities                               |
|----------------------------------------------------------------------------|
| Tidal             | Solid earth tidal displacement: complete model from    |
| displacements     |                                 IERS Conventions 2003  |
|                   | Permanent tidal term          : applied in tide model, |
|                   |                                 NOT included in site   |
|                   |                                 coordinates            |
|                   |                                                       |
|                   | Step 1: in-phase: degree 2 and 3                       |
|                   |           Nominal h02 and l02 : 0.6078, 0.0847 (anela.)|
|                   |           Nominal h22 and l22 :-0.0006, 0.0002         |
|                   |           Nominal h3  and l3  : 0.292 , 0.015          |
|                   |                                                       |
|                   |         out-of-phase: degree 2 only semi- and diurnal  |
|                   |           diurnal: nominal hI, lI :-0.0025,-0.0007     |
|                   |           semi-di: nominal hI, lI :-0.0022,-0.0007     |
|                   |                                                       |
|                   |         latitude dependence                            |
|                   |           diurnal: nominal l1 : 0.0012                 |
|                   |           semi-di: nominal l1 : 0.0024                 |
|                   |                                                       |
|                   | Step 2: in-phase: degree 2, diurnal                    |
|                   |         in-phase and out-of-phase: long-period tides   |
|                   |--------------------------------------------------------|
|                   | Pole tide                     : applied (IERS, 2003)   |
|                   |         nominal mean m1, m2   : 0.033, 0.331 arcsec.   |
|                   |--------------------------------------------------------|
|                   | Ocean tidal loading: FES2004                           |
|----------------------------------------------------------------------------|
| Atmospheric load.| Not applied                                            |
|----------------------------------------------------------------------------|
```

```
| Earth orientation| Tidal UT1 (> 5 days): modeled                           |
| models (EOP)     | Subdaily ERPs       : IERS2003                          |
|                  | Nutation            : IAU2000                           |
|                  | Precession          : USNO Circular No. 163             |
|----------------------------------------------------------------------------|
| Satellite center | IGS05 PCV model applied.                                |
| of mass          |                                                         |
| correction       |                                                         |
|----------------------------------------------------------------------------|
| Satellite phase  | IGS05 PCV model applied.                                |
| center calibrat. |                                                         |
------------------------------------------------------------------------------
| Relativity       | Periodic, -2(R*V/c): applied                            |
| corrections      | Gravity bending    : not applied                        |
|                  | Dynamical          : applied (IERS, 2003)               |
|                  | Shapiro            : applied                            |
------------------------------------------------------------------------------
| Time argument    | TDT                                                     |
------------------------------------------------------------------------------
| GNSS attitude    | Not applied                                             |
| model            |                                                         |
------------------------------------------------------------------------------

------------------------------------------------------------------------------
|                             ORBIT MODELS                                   |
|----------------------------------------------------------------------------|
| Geopotential     | JGM3 model up to degree and order 12 (+C21+S21)         |
|                  |---------------------------------------------------------|
|                  | GM = 398600.4415 km**3/sec**2                           |
|                  |---------------------------------------------------------|
|                  | AE =   6378.1363 km                                     |
|----------------------------------------------------------------------------|
| Third-body       | Sun and Moon as point masses                            |
|                  |---------------------------------------------------------|
|                  | Ephemeris: JPL DE405                                    |
|                  |---------------------------------------------------------|
|                  | GMsun  = 132712500000 km**3/sec**2                      |
|                  |---------------------------------------------------------|
|                  | GMmoon =    4902.7890 km**3/sec**2                      |
|----------------------------------------------------------------------------|
| Solar radiation  | Direct radiation: CODE RPR model coefficients           |
| pressure         |                   (updated 2007)                        |
|                  |---------------------------------------------------------|
|                  | Estimated RPR parameters (see Beutler 1994):            |
|                  |  Constants in D-, Y- and X-direction                    |
|                  |  Periodic terms in X-direction                          |
|                  |---------------------------------------------------------|
|                  | Earth shadow model includes: cylindric shadow           |
|                  |---------------------------------------------------------|
|                  | Moon shadow model includes: umbra and penumbra          |
|                  |---------------------------------------------------------|
|                  | Reflection radiation: not included                      |
|                  |---------------------------------------------------------|
|                  | New GPS satellite attitude model: not applied           |
|----------------------------------------------------------------------------|
| Tidal forces     | Solid earth tides: TIDE2000 (IERS 2000)                 |
|                  |---------------------------------------------------------|
|                  | Ocean tides: OT CSR30 model                             |
|----------------------------------------------------------------------------|
```

```
| Relativity       | Applied (IERS 2003)                                    |
|-------------------------------------------------------------------------|
| Numerical        | Integration algorithms developed at AIUB by Gerhard   |
| Integration      | Beutler (see references below). Representation of the |
|                  | the orbit by a polynomial of degree 10 for 1 hour.     |
|                  |--------------------------------------------------------|
|                  | Integration step: 1 hour                               |
|                  |--------------------------------------------------------|
|                  | Starter procedure: no special starter procedure needed |
|                  |--------------------------------------------------------|
|                  | Arc length: 72 hours                                   |
---------------------------------------------------------------------------

---------------------------------------------------------------------------
|               ESTIMATED PARAMETERS (APRIORI VALUES & SIGMAS)            |
|-------------------------------------------------------------------------|
| Adjustment       | Weighted least-squares algorithms                      |
|-------------------------------------------------------------------------|
| Station          | Starting with GPS week 1400, the IGS realization of   |
| coordinates      | ITRF2005 (IGS05) is used.                              |
|                  |                                                        |
|                  | Notes:                                                 |
|                  |                                                        |
|                  |   Number of GNSS stations typically included:          |
|                  |   . 200 for final analysis                             |
|                  |   . 120 for rapid analysis                             |
|                  |   .  90 for ultra-rapid analysis                       |
|                  |   Datum definition:                                    |
|                  |   . 3 no-net translation conditions                    |
|                  |   . 3 no-net rotation    conditions                    |
|                  |   . geocenter coordinates constrained nominally to     |
|                  |     zero values                                        |
|                  |   IGS05 fiducial sites are selected as reference, if:  |
|                  |   . horizontal deviation < 10 mm                       |
|                  |   . vertical   deviation < 30 mm                       |
|                  |   List of selected/rejected fiducial sites is given in |
|                  |   CODE's weekly analysis summary files.                |
|-------------------------------------------------------------------------|
| Satellite clock  | Zero-difference data analysis for GPS clock estimation |
| bias             | and for P1-C1 code bias retrieval:                     |
|                  |                                                        |
|                  | Satellite and receiver clock corrections are computed  |
|                  | on the basis of the double-difference orbit, ERP,      |
|                  | coordinate, and troposphere solutions. The generation  |
|                  | of high-rate clock results is performed in the         |
|                  | following three steps:                                 |
|                  | 1 Least-squares adjustment with a sampling of 5 min    |
|                  |   using phase and code observations.                   |
|                  | 2 Interpolation from  5 min to 30 sec using phase.     |
|                  | 3 Interpolation from 30 sec to  5 sec using phase      |
|                  |   (using IGS 1-Hz observation data).                   |
|                  |                                                        |
|                  | These clock corrections are consistent with carrier    |
|                  | phase as well as P1/P2 pseudorange measurements. CODE  |
|                  | P1-C1 pseudorange bias values of a moving 30-day       |
|                  | solution are considered to correct C1/X2 and C1/P2     |
|                  | receiver data.                                         |
|                  |                                                        |
|                  | Note: Daily sets of P1-C1 code bias values for the     |
```

	satellite constellation are derived as part of the global clock estimation process by distinguishing between three receiver classes. Elevation cutoff: 5 degrees
Receiver clock bias	See above (Satellite clock biases)
Orbital parameters	6 Keplerian elements plus 5 solar radiation parameters at start of arc; no a priori sigmas used. Estimated RPR parameters (see Beutler 1994): - Constants in D-, Y- and X-direction - Periodic terms in X-direction A priori orbits are the CODE rapid orbit solution. Pseudo-stochastic orbit parameters (small velocity changes), every 12 hours, constrained to: . 1.E-6 m/sec in radial . 1.E-5 m/sec in along-track . 1.E-8 m/sec in out-of-plane
Troposphere	Zenith delay parameters and pairs of horizontal delay gradient parameters are estimated for each station in intervals of 2 hours and 24 hours. No a priori constraints are applied. Piece-wise, linear parameterization, allowing for connection of the parameters at day boundaries.
Ionospheric correction	Not estimated in ionosphere-free analyses
Ambiguity	Ambiguities are resolved in a baseline-by-baseline mode performing the following steps: . Melbourne-Wuebbena approach (< 6000 km) . Quasi-Ionosphere-Free (QIF) approach (< 2000 km) . Phase-based widelane/narrowlane method (< 200 km) . Direct L1/L2 method, also for GLONASS (< 20 km) GNSS-derived global ionosphere map information is used to support the code-less methods.
Earth Orient. Parameters (EOP)	X- and Y-pole coordinates, and UT1-UTC are represented each with piece-wise linear polynomials which are continuous in time. UT1-UTC is fixed to the a priori value at the beginning of the first day. No further a priori sigmas are used. All reported CODE EOP solutions do include a subdaily EOP model (see above). The estimates therefore correspond to daily averages on top of the introduced a priori model. Drifts in nutation (Dpsi, Deps) are solved for in a special 3-day solution. The corresponding nutation parameters generally set up are constrained to the IAU 2000 model for the CODE official solution. High-rate (1-hour) X-, Y- and UT1-UTC estimates are also generated in a special 3-day solution.

GNSS attitude model	Not estimated
Other parameters	Center of mass coordinates: Center of mass, or geocenter coordinate parameters are commonly set up as part of each solution. The related parameters are usually heavily constrained to zero values. Additional computations on the normal equation level are made regularly in order to retrieve 1-day, 3-day, as well as weekly GNSS geocenter coordinates in the current ITRF. GNSS satellite phase center offsets and patterns: Corresponding parameters are commonly set up as part of each final solution for each individual GNSS satellite. The related parameters are usually heavily constrained to the corresponding nominal values (as defined by the IGS05 PCV model). Such GNSS PCV parameters are available for the ionosphere-free as well as the geometry-free linear combination.

REFERENCE FRAMES	
Inertial	Geocentric; mean equator and equinox of 2000 Jan 1 at 12:00 (J2000.0)
Terrestrial	IGS05 station coordinates and velocities
Interconnection	Precession: IAU 2000 Precession Theory
	Nutation: IAU 2000 Nutation Theory
	Relationship between UT1 and GMST: USNO Circular No. 163 (IAU Resolution)
	Tidal variations in UT1: periods > 5.8 days modeled but not removed (UT1-UTC sol.)

Glossary of acronyms

ACC	Analysis Center Coordinator
ACRIM	Active Cavity Radiometer Irradiance Monitor
ACRIMSAT	Active Cavity Radiometer Irradiance Monitor Satellite
AFB	Air Force Base
AS	Anti Spoofing
BKG	Bundesamt fur Kartographie und Geodaesie
C/A	Coarse Acquisition or Clear/Access
CBIS	Central Bureau Information System
CDDIS	Crustal Dynamics Data Information System
CODE	Center for Orbit Determination in Europe
CORS	Continuously Operating Reference Stations
CS	Cesium
CSR	Center for Space Research
DOD	Department of Defense
ECEF	Earth-Centered, Earth-Fixed
ECOM	Extended CODE Orbit Model
ERP	Earth Radiation Pressure
ESOC	European Space Operations Center
ESA	European Space Agency
ESS	Earth-Satellite-Sun

EUREF	European Reference Frame Network
GA	Geoscience Australia
GFZ	GeoForschungsZentrum
GIOVE	Galileo In-Orbit Validation Element
GLONASS	GLObal NAVigation Satellite System
GNSS	Global Navigation Satellite System
GOP	Geodetic Observatory Pecny
GPS	Global Positioning System
GRACE	Gravity Recovery and Climate Experiment
HRAO	Hartebeesthoek Radio Astronomy Observatory
IERS	International Earth Rotation Service
IGN	Institut Geographique National
IGS	International GNSS Service
ILRS	International Laser Ranging Service
ITRF	International Terrestrial Frame
ILS	Instrument Landing System
JGM-3	The Joint Gravity Model 3
JPL	Jet Propulsion Laboratory
KASI	Korean Astronomy and Space Science Institute
MCS	Master Control Station
MIT	Massachusetts Institute of Technology
MSODP	Multi-Satellite Orbit Determination Program
NANU	Notice Advisory to Navstar Users

NAVSAT	Navy Navigation Satellite System
NAVSTAR	NAVigation Satellite Timing And Ranging
NGA	National Geospatial Intelligence Agency
NGS	National Geodetic Survey
NOAA	National Oceanic and Atmospheric Administration
NRCan	Natural Resources Canada
OCS	Operational Control System
P-code	Precise code
POD	Precise Orbit Determination
PRN	Pseudo Random Noise
RB	Rubidium
RMS	Root Mean Square
RTN	Radial Transverse Normal
SA	Selective Availability
SIO	Scripps Institution of Oceanography
SLR	Satellite Laser Ranging
SMM	Solar Maximum Mission
SORCE	SOlar Radiation and Climate Experiment
SP3	Standard Product #3
SRP	Solar Radiation Pressure
SVN	Space Vehicle Number
TAI	International Atomic Time
TSI	Total Solar Irradiance

UARS	Upper Atmosphere Research Satellite
UCL	University College London
USAF	United States Air Force
USCG	United States Coast Guard
USNO	US Naval Observatory
UT1	Universal Time 1
UTC	Coordinated Universal Time
UTOPIA	University of Texas Orbit Processor

References

Adhya, S., A. Sibthorpe, M. Ziebart, and P. Cross (2004), Oblate earth eclipse state algorithm for low-earth-orbiting satellites, *Journal of spacecraft and rockets*, Vol. 41, No. 1, pp. 157-159.

Adhya, S., M. Ziebart, A. Sibthorpe, P. Arrowsmith, and P. Cross (2005), Thermal Force Modeling for Precise Prediction and Determination of Spacecraft Orbits, *Navigation*, Vol. 52, No. 3, pp. 131-144.

Anderle, R. (1973), Geodetic analysis through numerical integration, *Proceedings of the International Symposium on the Use of Artificial Satellites for Geodesy and Geodynamics*, Athens, Greece.

Bar-Sever, Y. (1996a), A New Model for GPS Yaw Attitude, *Journal of Geodesy*, Vol. 70, No. 11, pp. 714-723.

Bar-Sever, Y., J. Anselmi, W. Bertiger, and E. Davis (1996b), Fixing the GPS Bad Attitude: Modeling GPS Satellite Yaw During Eclipse Seasons, *Navigation*, Vol. 43, No. 1.

Bar-Sever, Y. (1997), New and Improved Solar Radiation Models for GPS Satellites Based on Flight Data, Final Report of Air Force Materiel, Command Space and Missile Systems Center/CZSF.

Bar-Sever, Y., and D. Kuang (2006), Improved Solar-Radiation Pressure Models for GPS Satellites, *NASA Tech Briefs*, NP0-41395.

Bartoli, A. (1884), Il calorico raggiante e il secondo principio di termodynamica, Il Nuovo Cimento, Vol. 15, No. 1, pp. 193-202.

Beutler, G., J. Kouba, and T. Springer (1995), Combining the orbits of the IGS Analysis Centers, *Bulletin Géodésique*, Vol. 69, pp. 200-222.

Beutler, G. (2005), *Methods of Celestial Mechanics*, Vol. II, Springer.

Bruyns, M. (1993), Longitude in the Context of Navigation, *The quest for longitude: the proceedings of the Longitude Symposium*, Cambridge, Massachusetts, Nov. 4-6.

Casson, L. (1914), *The ancient mariners: seafarers and sea fighters of the Mediterranean in ancient times*, Princeton, N.J.: Princeton University Press.

Craig, D. (2001), An Analysis of GPS Satellite Force Model, Center for Space Research, CSR-TM-01-02.

Dach, R., C. Urschl, M. Ploner, S. Schaer, and U. Hugentobler (2007), Latest GNSS orbit modelling improvement at CODE, European Geosciences Union; General Assembly, Vienna, Austria, April 16-20.

Dow, J., R. Neilan, and G. Gendt (2005), The International GPS Service (IGS): Celebrating the 10th Anniversary and Looking to the Next Decade, *Advances in Space Research*, Vol. 36, No. 3, pp. 320-326.

Eanes, R., B. Schutz, and B. Tapley (1983), Earth and Ocean Tide Effects on Lageos and Starlette, *Proceedings of the Ninth International Symposium on Earth Tides*.

Evans, A., R. Hill, G. Blewitt, E. Swift, T. Yunck, R. Hatch, S. Lichten, S. Malys, J. Bossler, and J. Cunningham (2002), The Global Positioning System Geodesy Odyssey, *Navigation*, Vol. 49, No. 1, pp. 7-34.

Fliegel, H., T. Gallini, and E. Swift (1992), Global Positioning System radiation force model for geodetic applications, *Journal of Geophysical Research*, Vol.97, No. B1, pp. 559-568.

Fliegel, H., and T. Gallini (1996), Solar Force Modeling of Block IIR Global Positioning System Satellites, *Journal of Spacecraft and Rockets*, Vol. 33, No. 6, pp. 863-866.

Fröhlich, C. (2006), Solar Irradiance Variability since 1978, *Space Science Reviews*, Vol. 125, No. 1, pp. 53-65, Springer.

Froideval, L. (2004), Power spectra of non-gravitational forces acting on GPS satellites, MS Thesis, Center for Space Research, The University of Texas at Austin, Austin, Texas.

Gao, G. (2009), Modernization Milestone, Observing the First GPS Satellite with an L5 Payload, *InsideGNSS*, May/June 2009.

Ge, M., E. Calais, and J. Haase (2000), Reducing satellite orbit error effects in near real-time GPS zenith tropospheric delay estimation for meteorology, *Geophysical Research Letters*, Vol. 27, No. 13, pp. 1915-1918.

Gutro, R., and J. Weier (2002), Solar Radiation and Climate Experiment, *Science Writer's Guide*, Science Systems and Applications, Inc., NASA Goddard Space Flight Center.

Harding, L. (1952), *A brief history of the art of navigation; an outline and background of the methods employed by navigators for finding their way around the seas*, New York, William-Frederick Press.

Hofmann-Wellenhof, B., H. Lichtenegger, and J. Collins (2001), *GPS: theory and practice*, Springer-Verlag Wien New York.

IGS (2008a), The IGS Tracking Network, retrieved 2008 from the World Wide Web: http://igscb.jpl.nasa.gov/network/iglos.html

IGS (2008b), IGS Organization, retrieved 2008 from the World Wide Web: http://igscb.jpl.nasa.gov/organization/centers.html

IGS (2008c), IGS Products, retrieved 2008 from the World Wide Web: http://igscb.jpl.nasa.gov/components/prods.html

IGS AAC (2009), Figures and Statistics from the IGS Final Orbit Combination, retrieved from the World Wide Web:
http://acc.igs.org/index_igsacc.html

ILRS (2008), Center of mass information, retrieved 2008 from the World Wide Web: http://ilrs.gsfc.nasa.gov/

Johnson, J., P. Kammeyer, and J. Ray (2001), The effects of geophysical fluids on motions of the Global Positioning System satellites, *Geophysical Research Letters*, Vol. 28, No. 17, pp. 3329-3332.

Kaplan, E., and Hegarty C. (2006), *Understanding GPS: Principles and Applications*, 2nd ed., Norwood: Artech House.

Kaula, W. (1966), *Theory of Satellite Geodesy*, Blaisdell Publishing, Waltham.

Knocke, P. (1989), Earth radiation pressure effects on satellites, Ph.D. dissertation, Center for Space Research, University of Texas at Austin, Austin, Texas.

Kouba, J. (2009), A simplified yaw-attitude model for eclipsing GPS satellites, *GPS Solutions*, Vol. 13, No. 1, pp. 1-12.

LaBrecque, J., J. Miller, and M. Pearlman (2008), A Recommendation on SLR Ranging to Future Global Navigation Satellite Systems, *Eos Trans. AGU*, Vol. 89, No. 53, Fall Meet. Suppl., Abstract G41C-0631.

Marquis, W., and C. Krier (2000), Examination of the GPS Block IIR Solar Pressure Model, *Proceedings of ION-GPS*, Salt Lake City, Utah.

Maxwell, J. (1871), *Theory of heat*, London: Longmans, Green, and co.

Maxwell, J. (1873), *A Treatise on Electricity and Magnetism*, Vol. II, Oxford: Clarendon Press.

Montenbruck, O., and E. Gill (2000), *Satellite Orbits, Models, Methods and Applications*, Springer Berlin Heidelberg New York.

Moscati, S. (1988), *The Phoenicians*, Milan: Bompiani.

Pearlman, M., J. Degnan, and J.M., Bosworth (2002), The International Laser Ranging Service, *Advances in Space Research*, Vol. 30, No. 2, pp. 135-143.

Pervan, B., and L. Gratton (2005), Orbit ephemeris monitors for local area differential GPS, *Aerospace and Electronic Systems, IEEE Transactions on*, Vol. 41, No. 2, pp. 449-460.

Porter, W. (1976), Solar force-torque model for the GPS space vehicle system, Rockwell TOR 76 MA641, enclosure 2, Opt. Model Rep. CDRL 064A14, F04701-78-C-0153, Rockwell Int., Seal Beach, California.

Ries, J., C. Huang, and M. Watkins (1988), Effect of General Relativity on a near-Earth satellite in the geocentric and barycentric reference frames, *Physical Review Letters*, Vol. 61, pp. 903-906.

Rim, H. (1992), TOPEX orbit determination using GPS tracking system, Ph.D. dissertation, Center for Space Research, The University of Texas at Austin, Austin, Texas.

Rim, H., and B. Schutz (2002), Precision orbit determination (POD), Version 2.2, Geoscience Laser Altimeter System (GLAS) algorithm theoretical basis document.

Rizos, C. (1999), Notes on Basic GPS Positioning and Geodetic Concepts, University of New South Wales. Retrieved 2003 from website: http://www.gmat.unsw.edu.au/snap/gps/gps_notes.htm

Springer, T., G., Beutler, and M., Rothacher (1998), A New Solar Radiation Pressure Model for the GPS Satellites, *GPS Solutions*, pages 50-62.

Springer, T., and U. Hugentobler (2001), IGS Ultra rapid products for (near-) real-time applications, *Physics and Chemistry of the Earth, Part A*, Vol. 26, No. 6-8, pp. 623-628.

Schutz, B., and B. Tapley (1980), Utopia: University of Texas Orbit Processor, Dept. of Aerospace Engineering and Engineering Mechanics, The University of Texas at Austin, TR 80-1, 1980.

Steigenberger, P., G. Gendt, R. Ferland, and I. Romero (2008), Current Status of the IGS Reprocessing, IGS Analysis Center Workshop, Miami Beach, Jun. 2-6.

Tapley, B., and J. Ries (1987), Orbit Determination Requirements for TOPEX, Proceedings AAS/AIAA, Astrodynamics Specialist Conference, Kalispell, Montana, August 10-13.

Tapley, B., M. Watkins, J. Ries, G. Davis, R. Eanes, S. Poole, H. Rim, B. Schutz, C. Shum, S. Nerem, F. Lerch, J. Marshall, S. Klosko, N. Pavlis, and R. Williamson (1996), The Joint Gravity Model 3 (JGM-3), *Journal of Geophysical Research*, Vol. 101, No. B12, pp. 28029-28049, Dec. 10.

Tapley, B., B. Schutz, and G. Born (2004), *Statistical Orbit Determination*, Elsevier Academic Press, Boston, Massachusetts.

United States Coast Guard (2008), GPS constellation status, retrieved 2008 from the World Wide Web:
http://www.navcen.uscg.gov/navinfo/Gps/ActiveNanu.aspx

Vigue, Y., and B. Schutz (1991), Thermal imbalance force modelling for a GPS satellite using the finite element method, paper presented at the AAS/AIAA Spaceflight Mechanics Meeting, Washington, D.C.

Vigue, Y. (1994), Thermal Force Modeling for Global Positioning System Satellites Using the Finite Element Method, *Journal of Spacecraft and Rockets*, Vol. 31, No. 5, pp. 855-859.

Vokrouhlický, D., P. Farinella, and F. Mignard (1993), Solar radiation pressure perturbations for Earth satellites. I. A complete theory including penumbra transitions, *Astronomy and Astrophysics*, Vol. 280, pp. 295-312.

Vokrouhlický, D., P. Farinella, and F. Mignard (1994), Solar radiation pressure perturbations for Earth satellites. II. An approximate method to model penumbra transitions and their long-term orbital effects on LAGEOS, *Astronomy and Astrophysics*, Vol. 285, pp. 333-343.

Wahr, J. (1981), Body Tides on an Elliptical, Rotating Elastic and Oceanless Earth, *Geophysical Journal of the Royal Astronomical Society*, Vol. 64, No. 3, pp. 677-703.

Wang, H. (2006), Precise GPS orbit determination and prediction using H_∞ neural network, *Journal of the Chinese Institute of Engineers*, Vol. 29, No. 2, pp. 211-219.

Willson, R., S. Gulkis, M. Janssen, H. Hudson, and G. Chapman (1981), Observations of Solar Irradiance Variability, *Science, New Series*, Vol. 211, No. 4483, pp. 700-702, American Association for the Advancement of Science.

Wilmhoff, B., F. Lalezari, V. Zavorotny, and E. Walsh (2007), GPS ocean altimetry from aircraft using the P(Y) code signal, Geoscience and Remote Sensing Symposium, Barcelona, Spain, Jul. 23-27.

Ziebart, M., and P. Dare (2001), Analytical solar radiation pressure modeling for GLONASS using a pixel array, *Journal of Geodesy*, Vol. 75, No. 11, pp. 587-599.

Ziebart, M, S. Adhya, A. Sibthorpe, and P. Cross (2003), GPS Block IIR Non-Conservative Force Modelling: Computation and Implications, proceedings of ION-GPS, pp. 2671-2679, Portland, Oregon.

Ziebart, M. (2004a), Generalized Analytical Solar Radiation Pressure Modeling Algorithm for Spacecraft of Complex Shape, *Journal of Spacecraft and Rockets*, Vol. 41, No. 5, pp. 840-848.

Ziebart, M. (2004b), Personal communication.

Ziebart, M., S. Adhya, A. Sibthorpe, S. Edwards, and P. Cross (2005), Combined radiation pressure and thermal modelling of complex satellites: Algorithms and on-orbits tests, *Advances in Space Research*, Vol. 36, pp. 424-430.

Vita

Laurent Froideval was born on November 2nd, 1980 in Strasbourg located in the Eastern part of France. He is the son of Marie-Christine Fischbach and Jean-Claude Froideval. After graduating from the Lycee Anne de Bretagne (Rennes, France) in June 1998, he entered the Classes Preparatoires aux Grandes Ecoles in Rennes, France in September 1998. After passing the nationwide Concours Aux Grandes Ecoles in May-July 2000, he entered the Ecole Centrale de Lille (Lille, France) in September 2000. Then, in August 2002, he entered the Graduate School of the University of Texas at Austin. He earned the Master's degree in Aerospace Engineering in May 2004.

Permanent address: 6, rue Charles Boutard
37000 Tours
France

This thesis was typed by the author.